Force-Detected Nuclear Magnetic Resonance Independent of Field Gradients

Thesis by Garett Michael Leskowitz

in partial fulfillment of the requirements
for the degree of Doctor of Philosophy

California Institute of Technology
Pasadena, California
2003
(Defended January 14, 2003)

Acknowledgements

First and foremost, I would like to acknowledge the support and guidance of my thesis advisor and mentor, Dan Weitekamp. It is my good fortune to have worked with and learned from someone who has his special blend of insight, enthusiasm, rigor, and the big picture. I appreciate his patience with my own sometimes erratic style and pace in scientific work, and I will miss our collaboration. His efforts to promote his students in the scientific community through opportunities to present at conferences are atypical and show great confidence in his own work and in us.

I would like to thank the many scientists I have worked with and those who have shown interest and given help, advice, and encouragement in my studies and research, particularly Richard Driver, Alan Davison, Craig Lehmann, Andrew Barron, Constantino Yannoni, Dan Rugar, John Baldeschwieler, and James Yesinowski.

I would also like to thank the students I have worked with in Dan's group. Jack Hwang and Pedro Pizarro gave much needed help early on, and my first and continuing conversations with Len Mueller, John Marohn, and particularly with Paul Carson were largely the reason why I decided to join the group. (I also thank Len Mueller for time off from postdoctoral research to complete this thesis!) Jim Kempf, Mike Miller, and Bruce Lambert merit special mention for help, new ideas, and friendship during our shared years at Caltech, and I am happy to see the traditions carried on by Ramez Elgammal, Valerie Norton, and Mark Butler. But particular thanks go to my principal collaborator, my adjoint in the dual spaces of science and

jazz, Lou Madsen. Without his drive, and efforts, and insight in virtually all phases of the work described in this thesis, BOOMERANG would not have advanced to anywhere near its current state. I consider it a privilege to have worked in such company.

I would like to acknowledge financial support from Caltech and from NASA's Jet Propulsion Laboratory, and I would like to thank Thomas George and Weilong Tang of JPL's Microdevices Laboratory and the several students and colleagues who worked with them on the effort to construct microfabricated versions of BOOMERANG technology.

I would like to thank Mary Mason for her love, patience, and encouragement. Together we are far greater than our sum. Finally, but certainly not least, I would like to thank my parents, George and Mary Leskowitz, and my sister, Laurie, for their encouragement and love, and for their example as thinking and caring humans, which I have tried to follow.

Abstract

This thesis describes a new method of magnetic resonance detection based on mechanical displacements caused by magnetic forces, which is general with respect to sample and pulse sequence. A spin-bearing sample placed inside a flexible magnet assembly distorts that assembly in proportion to the sample's magnetization. Radio-frequency fields that modulate the sample's spin magnetization at this detector's mechanical resonance frequency encode magnetic resonance spectra into the detector's trajectory. A key insight is that such mechanical detection can be performed within optimized detectors with no need for field gradients inside the sample volume, circumventing the deleterious consequences of such gradients for sensitivity and resolution. The new method is called Better Observation of Magnetization, Enhanced Resolution, and No Gradient (BOOMERANG), and its sensitivity is predicted to exceed that of inductive detection at microscopic size scales.

A prototype BOOMERANG spectrometer optimized for 3 mm diameter liquid and solid samples is described. The device uses direct digital synthesis of radio-frequency waveforms in its operation and fiber-optic interferometry to detect picometer-scale motions of a detector magnet. This magnet is bound to a tuned mechanical oscillator inside a magnet assembly designed for homogeneity of the magnetic field in the sample. Several types of time-domain FT-NMR spectra on test samples are presented. The data confirm theory and design principles.

The favorable scaling of BOOMERANG's sensitivity and the numerous potential uses for NMR at reduced size scales motivate construction of spectrometers optimized for microscopic samples. Geometric concerns in scaling down BOOMERANG are addressed quantitatively. At size scales where the number of spins is such that mean magnetization is smaller than fluctuations, such fluctuations, if not accounted for, can dominate the noise regardless of the physical detection method used. A measurement paradigm using correlations of these fluctuations to encode spectra is proposed to suppress this quantum noise, and the sensitivity of this method, which we call Correlated Observations Narrow Quantum Uncertainty, Enhancing Spectroscopic Transients (CONQUEST), is analyzed. BOOMERANG and CONQUEST promise to extend the applicability of nuclear magnetic resonance (NMR) for chemical analysis to samples and problems that are currently inaccessible by NMR due to poor sensitivity.

Contents

List of Figures

List of Tables

Chapter 1: Overview

1.0 Introduction

This thesis concerns observation of magnetic resonance phenomena through measurements of magnetically induced mechanical oscillations. The principal result of this work is a new class of detectors and methods that promises to extend the applicability of nuclear magnetic resonance (NMR) for chemical analysis and imaging to samples and problems that are currently inaccessible by NMR due to the poor sensitivity of traditional methods at reduced size scales.

NMR is known by its practitioners as a method of finely detailed non-destructive chemical analysis or as a tool for non-invasive medical imaging. But at the most fundamental level, nuclear magnetic resonance is the resonant reorientation of nuclear moments by applied magnetic fields. The reorientation of nuclear moments in a sample produces changes in the sample's magnetization as a function of applied electromagnetic stimuli, such stimuli most often taking the form of pulses of radio-frequency (rf) fields. The dynamics of the sample's spin system are registered by a detection apparatus as changes in the weak magnetic field produced by the sample. Leaving aside the so-called "trigger methods" of magnetic resonance[1], and optical methods that are peculiar only to a very narrow range of

samples or conditions[2-4], NMR devices are therefore essentially *magnetometers* connected to ancillary apparatus of varying degrees of sophistication.

Three types of detection schemes are commonly used to measure the magnetization of a sample (or its susceptibility). The first type of detector, an induction coil, forms the basis of all commercial NMR spectrometers and magnetic resonance imagers. Coherent precession of a sample's magnetization produces a change in the magnetic flux linking a nearby or enclosing coil. The resulting electromotive force in the coil, produced in accordance with Faraday's law, is amplified and analyzed.

A second type of detector is the superconducting quantum interference device (SQUID). The static magnetic flux through a superconducting loop disposed near the sample causes a change in the relative phase of two parts of an electron's wavefunction as those parts coherently traverse two separate paths around the loop. Recombination of the two parts of the wavefunction can occur in phase or out of phase, and as a result, the conductance of the device depends upon the flux linking the loop, and therefore on the magnetization of the sample. This physics forms the basis of SQUID magnetometers, which are used for static or low-frequency magnetometry[5,6]. SQUIDs have also been used in low-field NMR and nuclear quadrupole resonance (NQR)[7,8].

A third type of detector is the *force detector.* Any magnetized body that either moves in response to magnetic forces exerted by the sample or that forces the sample itself to move falls into this class. Force detection is the oldest method

of magnetometry/susceptometry. It is the basis for the Gouy balance[9,10] and for the vibrating-sample magnetometer[11]. It was also the basis for the very first method of magnetic *resonance spectroscopy* in the form of Rabi's molecular beam method[12]. Despite this long history, here we take a fresh look at detection of magnetic resonance with mechanical means.

1.1 Better Observation of Magnetization, Enhanced Resolution, and No Gradient (BOOMERANG)

Figure 1.1 shows a spherical sample enclosed inside an idealized flexible magnetic "detector" in the shape of a hollowed-out sphere. The magnetizations of the sample and the detector are aligned along the same axis. The sample exerts magnetic forces that tend to distort the detector as those dipole elements in the detector near the "poles" of the sample are attracted axially, while those near the "equator" are repelled laterally. Cyclic inversion of the sample's magnetization (discussed in Chapter 3) reverses the sign of the forces, alternately compressing and extending the flexible detector along its magnetization axis.

This mechanical detector is ideal in the sense that at no time is there a field gradient inside the sample volume, no matter how large the elliptical distortion of the spherical detector along its magnetization axis.

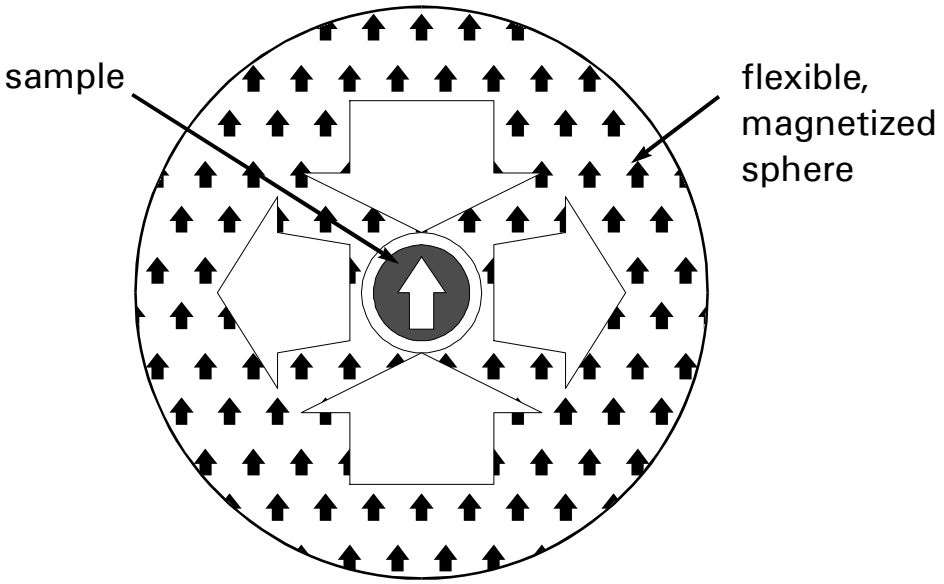

Figure 1.1. Flexible-sphere model of idealized mechanical detector. The sample is surrounded by a hollowed sphere of flexible magnetic material, and both are magnetized as shown by the vertical arrows. The sample exerts forces on individual dipole elements in the detector material, and these forces distort the detector along its symmetry axis.

Figure 1.2 shows a single cylindrical magnet above a spherical sample. Both the magnet and the sample are magnetized along the symmetry axis of the cylinder. The magnet is bound to a flexible suspension that provides for it a high-quality harmonic motion along its symmetry axis. Cyclic inversion of the sample's magnetization may be used to modulate the force coupling the sample and the magnet, resonantly driving this harmonic oscillation. The arrangement of sample, magnet, and suspension is reproduced inside an assembly of other

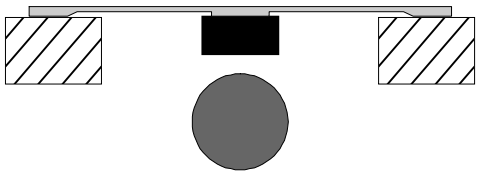

Figure 1.2. Cylindrical detector magnet bound to an anchored, flexible suspension and disposed near a spherical sample.

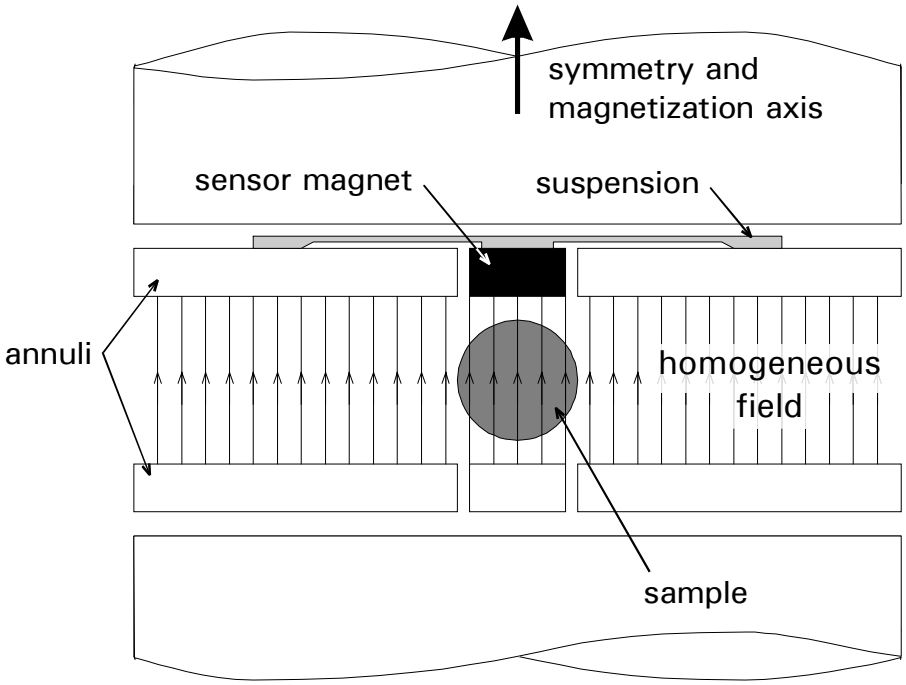

Figure 1.3. Magnet assembly incorporating the sensor magnet and flexible suspension of Figure 1.2. All the magnets in the assembly are magnetized along the common axis of cylindrical symmetry, which is vertical in the figure. The dimensions of the magnets are chosen so that the magnetic field throughout the sample volume is as homogeneous as possible, such homogeneity being limited by the smallest possible spacing between the sensor magnet and surrounding annulus. Reflection symmetry across the horizontal plane through the sample nulls odd-order field gradients.

magnets, all polarized along the common axis of cylindrical symmetry, in Figure 1.3, with the single magnet of Figure 1.2 now designated as a "sensor magnet."

In this geometry, the axial oscillation of the sensor magnet takes place inside an annular magnet, with the height of these two magnets the same, their faces flush when the sensor magnet is at the equilibrium point of its axial motion. The totality of the magnets in the assembly provides for the sample a homogeneous field that, by design, approximates the homogeneity of the idealized spherical case of Figure 1.1.

In both the idealized geometry of Figure 1.1 and in the cylindrical geometry of Figure 1.3, the latter being motivated by the practical concerns of ease of fabrication and sample access, we have emphasized the homogeneity of the magnetic field throughout the sample volume. The experimentally observed fact that the sensor magnet of Figure 1.3 can be made to oscillate in response to modulation of the sample's magnetization shows that the ability to measure susceptibility and magnetic resonance with force detection *is entirely independent of any field gradient in the sample volume.* This view, which is in contrast to the conceptual development of other force-detection methods (briefly surveyed in Appendix A), is the central theme behind the method of magnetic resonance now called Better Observation of Magnetization, Enhanced Resolution, and No Gradient (BOOMERANG)[13,14].

1.2 Problems Caused by Field Inhomogeneity

The BOOMERANG method solves several problems associated with large gradients in the sample volume. Without the annular and other magnets of Figure 1.3, the sensor magnet's own inhomogeneous field spreads the Larmor frequencies of spins in the sample over a range incompatible with the great majority of NMR experiments. While the deleterious consequences of this for spectroscopic resolution are readily appreciated, the consequences for imaging and for sensitivity in general are also severe. This spread of Larmor frequencies over a given sample volume becomes larger as the sensor magnet is made smaller. In Chapter 2, we examine the sensitivity of force-detection in the presence of thermal fluctuations in

the average force on the sensor magnet (Brownian-motion noise), and we find that in order to be near the optimal sensitivity, the sensor magnet, which must be placed as close as possible to the sample, must also be roughly the same size as the sample volume. In this case, the spread of nuclear Larmor frequencies can be of order 30 MHz for sensor magnets composed of the best ferromagnetic materials.

In force-detection methods that couple spin-dependent forces exerted by longitudinal magnetization to oscillatory motion, an rf field near the Larmor frequency is used to invert the sample's magnetization. The spectral range over which spins can be inverted with practical rf fields in nuclear resonance is of order $\sim$100 kHz. As shown in Figure 1.4, in the absence of the annular and other magnets, the field gradient $G_{zz} = \partial B_z / \partial z$ of the sensor magnet and the effective rf field B_1 define a "sensitive slice" through the sample, whose thickness is of order B_1/G_{zz}, outside of which the rf field is ineffective in inverting the spins. These spins therefore do not contribute to the signal energy. In combination with means to scan this surface through the sample volume, this provides an imaging capability[15-17], in which data from separate pixels is collected during separate shots of the experiment, and this approach is called magnetic resonance force microscopy (MRFM). However, this capability is bought at the price of reduced signal energy per shot, in contrast to modern NMR imaging

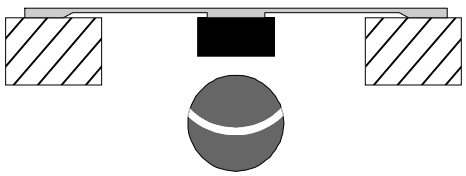

Figure 1.4. Sensitive slice in the sample volume. In the absence of the other parts of the magnet assembly of Figure 1.3, the sensor magnet can spread the Larmor frequencies of spins in the sample over many megahertz. Only those spins within the bandwidth of the applied rf field are inverted during detection.

protocols with higher throughput (*e.g.*, Fourier zeugmatography and back projection)[18], in which signal is acquired during each shot from many pixels, often the whole imaged volume, with the spatial information encoded in the frequency domain by way of field gradients that do not move the magnetization out of the observable spectral range.

The boundaries of the sensitive surface in gradient-based methods of force-detected magnetic resonance[15] are not sharply defined, but instead, the distribution of Rabi frequencies falls off gradually near the edges of the slice[†]. This renders such methods incompatible with modern multiple-pulse sequences that depend upon both a spatially homogeneous Rabi frequency and a spread of Larmor frequencies less than this Rabi frequency to achieve precise, coherent control of the observed spin population through numerous rf pulses.

The problems of reduced spectroscopic resolution, sensitivity, and coherent control will be more severe in NMR of liquids or of molecules weakly bound to a surface, where diffusion out of a sensitive region will occur on a timescale that may be short compared to the time during which either spectral information is to be encoded or during which detection is to take place. In order to suppress the effects of such diffusion, gradient-based methods must be used at lower temperatures or be subject to reduced sensitivity as a result of designs that use larger-than-optimal sensor magnets. This may seriously limit the possibilities for application of such

---

[†] The Rabi frequency characterizes the rate at which the rf field reorients the angle the local magnetization makes with the static field.

methods in chemistry and, especially, biology. The BOOMERANG method minimizes all of these difficulties.

1.3 Outline

In Chapter 2, we quantitatively address the detection of magnetic resonance signals in the presence of thermal noise for the cases of force detection and inductive detection. While this subject has been taken up by several other authors[1,19,20], the indirect, "reciprocity" arguments used by these authors are bypassed herein in favor of a more direct approach that lends itself well to analyses of scaling relations and geometrical optimizations, which are partially obscured by reciprocity arguments. The principal conclusion of Chapter 2 is that in the range of microns to millimeters the signal-to-noise ratio of BOOMERANG force-detected NMR scales with the square-root of the size r of the sample-plus-optimized-detector, while that of traditional inductively detected NMR scales at best as r^2, indicating a sample size (in the $\sim$0.1-1 mm range, depending on the field strength and the magnetogyric ratio of the target spins) below which BOOMERANG detection is preferred.

Chapter 3 introduces the apparatus used in the experiments described in this thesis. The prototype apparatus obtains a variety of NMR data on liquid and solid samples contained within a $\sim$3 mm diameter sample region. The observed signals and noise confirm design principles and the theory of force-detected NMR. Chapter 3 details the magnet assembly and the quantitative assessment of field parameters, the sensor oscillator, the fiber-optic interferometer used to monitor the oscillator's

position, the signal acquisition and conditioning system, rf synthesis and amplification, the NMR coil and sample-holder assembly, and cyclic inversion of the sample's magnetization. Also included is a detailed assessment of system noise sources.

The measurement of various kinds of spectroscopic data with the BOOMERANG prototype forms the subject of Chapter 4. The general notion of time sequencing, in which spectroscopic data are encoded pointwise during a time period separate from the signal-detection period, is used to measure several different kinds of spectroscopic observables. The combination of optimal sensitivity with high resolution has allowed measurement of FT-NMR spectra, longitudinal relaxation times, nutation, spin-echoes with sub-hertz line widths, and heteronuclear *J* spectroscopy in model compounds containing protons and fluorine-19.

Chapter 5 concerns issues that arise in scaling down BOOMERANG NMR to the small numbers of spins in the sample volume possible at the micron size scale and below. The principal subject of this chapter is *spin noise*, which is the uncertainty in measured spectroscopic parameters arising from quantum-thermodynamic fluctuations in the sample's magnetization. These fluctuations, if not accounted for, are an increasingly important source of noise, whatever the method of detection, in the size regime where such fluctuations exceed the mean polarization. The solution suggested herein is measurement of time-correlations of magnetization[21-23]. The correlation signal contains the same information as does the ordinary NMR spectrum, but with roughly unit signal-to-noise ratio per root shot of the experiment, independent of the sample's polarization. Also addressed are

geometrical considerations in application of BOOMERANG to surface-bound or to nanoscopic samples, where, in the latter, the higher mechanical frequencies associated with optimized nanoscopic oscillators suggest coupling torsional oscillators to precessing or spin-locked transverse magnetization at radio frequencies.

References

1 A. Abragam, *Principles of Nuclear Magnetism* (Clarendon Press, Oxford, 1961).

2 J. Wrachtrup, A. Gruber, L. Fleury, and C. von Borczyskowski, *Chem. Phys. Lett.* **267,** 179 (1997).

3 H. Arnolds, D. Fick, H. Unterhalt, A. Voss, and H. J. Jansch, *Sol. St. Nucl. Magn. Reson.* **11,** 87 (1998).

4 R. Tycko and J. A. Reimer, *J. Phys. Chem.* **100,** 13240 (1996).

5 W. G. Jenks, S. S. H. Sadeghi, and J. P. Wikswo, *J. Phys. D Appl. Phys.* **30,** 293 (1997).

6 J. Clarke, *Curr. Opinion Sol. St. & Matl. Sci.* **2,** 3 (1997).

7 C. Connor, *Adv. Magn. Reson.* **15,** 201 (1990).

8 Y. S. Greenberg, *Rev. Mod. Phys.* **70,** 175 (1998).

9 L. G. Gouy, *Compt. Rend.* **109,** 935 (1889).

10 L. N. Mulay, in *Physical Methods of Chemistry*, Vol. I part 4, 4th ed., edited by A. Weissberger and B. W. Rossiter (Wiley-Interscience, New York, 1972), Chapter 7.

11 Y. L. Yousef, R. K. Gigris, and H. Mikhail, *J. Chem. Phys.* **23,** 959 (1955).

12 I. I. Rabi, J. R. Zacharias, S. Millman, and P. Kusch, *Phys. Rev.* **53,** 318 (1938).

13 G. M. Leskowitz, L. A. Madsen, and D. P. Weitekamp, *Sol. St. Nucl. Magn. Reson.* **11,** 73 (1998).

14 D. P. Weitekamp and G. M. Leskowitz, U. S. Patent No. 6,100,687 (California Institute of Technology, USA, 2000).

15 J. A. Sidles, J. L. Garbini, K. J. Bruland, D. Rugar, O. Züger, S. Hoen, and C. S. Yannoni, *Rev. Mod. Phys.* **67,** 249 (1995).

16 O. Züger and D. Rugar, *Appl. Phys. Lett.* **63,** 2496 (1993).

17 O. Züger and D. Rugar, *J. Appl. Phys.* **75,** 6211 (1994).

18 P. Mansfield and P. G. Morris, in *Adv. Magn. Reson.*, Supplement 2 (Academic Press, New York, 1982).

19 D. I. Hoult and R. E. Richards, *J. Magn. Reson.* **24,** 71 (1976).

20 J. A. Sidles and D. Rugar, *Phys. Rev. Lett.* **70,** 3506 (1993).

21 P. J. Carson, L. A. Madsen, G. M. Leskowitz, and D. P. Weitekamp, *Bull. Am. Phys. Soc.* **44,** 541 (1999).

22 P. J. Carson, L. A. Madsen, G. M. Leskowitz, and D. P. Weitekamp, U. S. Patent No. 6,081,119 (California Institute of Technology, USA, 2000).

23 P. J. Carson, L. A. Madsen, G. M. Leskowitz, and D. P. Weitekamp, U. S. Patent No. 6,087,872 (California Institute of Technology, USA, 2000).

Chapter 2: On Signal Detection and Noise

2.0 BOOMERANG Force Detection

Without considering how to encode the NMR *spectrum* of a sample, in this chapter we address measurement of its nuclear magnetization by using the latter to drive a given mode of a mechanical oscillator. For concreteness, we consider the case of an oscillator that couples linearly to the longitudinal magnetization of the entire sample, which we therefore invert twice per oscillator period to drive the mode. We address the specifics of cyclic inversion in BOOMERANG in Chapter 3. Here we note only that the entire magnetization of the sample is inverted, and that this magnetization decays exponentially with a time constant we shall call T_{1a}, which for many samples is ideally as long as the longest relaxation time of the spin system, T_1. In a typical experiment, the Fourier component of the oscillator's motion at the driving frequency is proportional to the sample's magnetization at the beginning of a time interval during which the oscillator is driven.

In general, the oscillator's motion is defined in terms of a mechanical coordinate in the "flexible detector" of Chapter 1 along which the sample's magnetic force acts. This is also the coordinate along which the flexible suspension's restoring forces act and along which displacements are measured. We

take the "signal" to be the magnetic force exerted by the sample at the start of the oscillator-driving or *detection* period (or, rather, the projection of this force on the measured coordinate). The goal of the detection period is to measure this value with least uncertainty.

For concreteness, we return to the uniformly magnetized spherical sample inside the magnet assembly of Figure 1.3, with its designated sensor magnet. Each of the component magnets will in principle move separately in response to forces exerted by the sample's magnetization. However, since the sensor magnet is much lighter than other magnets in the assembly by design, and since the other magnets are fixed to rigid supports, the driven mechanical mode is very nearly approximated by the harmonic motion of the sensor magnet inside its encircling annulus. Thus, in the prototype described in Chapter 3, the sensor magnet moves up and down along the symmetry axis inside an otherwise rigid magnet assembly, and the displacement, z, of the sensor magnet relative to a fiber-optic position sensor fixed to the other magnets is recorded. The signal is thus defined as the net force exerted by the sample on the sensor magnet only.

The force exerted on a magnetic dipole $\boldsymbol{\mu}_d$ by another dipole $\boldsymbol{\mu}_s$ may be written

$$\mathbf{F} = -\nabla\left(-\mathbf{B}_s \cdot \boldsymbol{\mu}_d\right) = +\nabla\left(\frac{\mu_0}{4\pi}\boldsymbol{\mu}_s \cdot \left(\frac{3\hat{\mathbf{r}}\hat{\mathbf{r}} - 1}{r^3}\right) \cdot \boldsymbol{\mu}_d\right), \tag{2.1}$$

where $\hat{\mathbf{r}}$ denotes the unit vector pointing from the position of $\boldsymbol{\mu}_s$ (the *s*ample) to that of $\boldsymbol{\mu}_d$ (the *d*etector), ∇ denotes the gradient with respect to the coordinates of

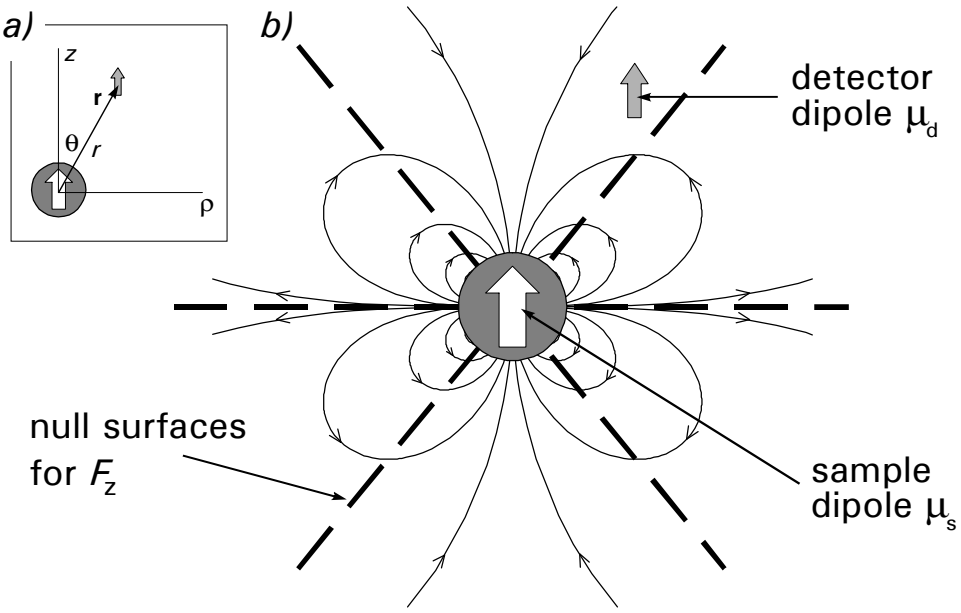

Figure 2.1. Force field near a sample with moment μ_s for axial detector dipoles μ_d. a) Coordinate system used in the text. b) Dotted lines define surfaces of revolution upon which the z-component of the force vanishes.

$\boldsymbol{\mu}_\mathbf{d}$, and $\mathbf{B}_s$ denotes the magnetic field due to the sample[1]. To calculate the force of one rigid body of finite extent on another, we must replace $\boldsymbol{\mu}_\mathbf{s}$ by $\mathbf{M}_s(\mathbf{r}_s)dV_s$ and $\boldsymbol{\mu}_\mathbf{d}$ by $\mathbf{M}_d(\mathbf{r}_d)dV_d$ and then integrate over the volumes V_s and V_d of the two bodies, whose magnetizations are $\mathbf{M}_s(\mathbf{r}_s)$ and $\mathbf{M}_d(\mathbf{r}_d)$. For the present case, $\mathbf{M}_s = M_s\hat{\mathbf{z}}$ and $\mathbf{M}_d = M_d\hat{\mathbf{z}}$ are constant vectors along the axis of cylindrical symmetry, $\hat{\mathbf{z}}$. Integration over the sample's spherical volume yields

$$\mathbf{dF} = \frac{\mu_0}{4\pi}\frac{V_s M_s M_d}{r^4}\left[\left(9-15\cos^2\theta\right)\cos\theta\hat{\mathbf{z}} + \left(3-15\cos^2\theta\right)\sin\theta\hat{\boldsymbol{\rho}}\right]dV_d \qquad (2.2)$$

for the force on the dipole element $M_d\hat{\mathbf{z}}dV_d$ at position $\mathbf{r} = r\left(\cos\theta\hat{\mathbf{z}} + \sin\theta\hat{\boldsymbol{\rho}}\right)$ in coordinates that are defined in Figure 2.1 a. Equation (2.2) may be viewed as defining a field of force around the sample that is experienced by detector dipoles

aligned along $\hat{\mathbf{z}}$. This force field is illustrated in Figure 2.1 b, where the lines of force (which are not the same as magnetic field lines) are parallel to **dF** at all points. This picture allows us to make some observations regarding the design of a suitable force detector.

First, since the force field is cylindrically symmetric, and since we wish to preserve field homogeneity in the sample volume as best as possible, our sensor magnet will be a solid of revolution about the magnetization axis $\hat{\mathbf{z}}$. Our choice of a circular cylinder, which is motivated by ease of fabrication and sample access, turns out to be very nearly the best shape (see Appendix B) given the requirement that the sensor magnet and the sample not occupy the same space. We make this latter criterion more concrete by defining a distance R_{max} from the center of the sample to the near edge of the sensor magnet. R_{max} is ideally dominated by the sample's radius, but it also includes space that may be necessary for intervening NMR coil windings and any barriers that might be required to keep the sample and sensor oscillator at different temperatures or pressures. Cylindrical symmetry requires that integration of Equation (2.2) over the sensor magnet volume yield a net force whose transverse components vanish, and so we consider only the *z*-component $dF_z = \hat{\mathbf{z}} \cdot \mathbf{dF}$ in what follows. The dotted lines in Figure 2.1 denote nodal surfaces of revolution (cones), at angles of 90° and $\theta_0 = \arccos\sqrt{3/5} \approx 39.2°$ with the vertical, upon which dF_z vanishes. The *z*-component of the force field changes sign when crossing through these surfaces. In order for the forces on individual dipole elements in the sensor to add in concert, a single, rigid sensor will lie entirely inside a nodal surface.

We calculate the dc force on the sensor magnet by integrating Equation (2.2) over the sensor's volume. The result for any volume may be written

$$F_z = \kappa_F \mu_0 V_s M_s M_d / R_{max} , \tag{2.3}$$

where

$$\kappa_F = \frac{R_{max}}{4\pi} \int \frac{1}{r^4} \left(9\cos\theta - 15\cos^3\theta\right) dV_d \tag{2.4}$$

is a dimensionless (and scale invariant) "shape factor." For a cylindrical sensor of radius *a* and height *h* placed a distance R_{max} from the center of the sample as in Figure 2.2,

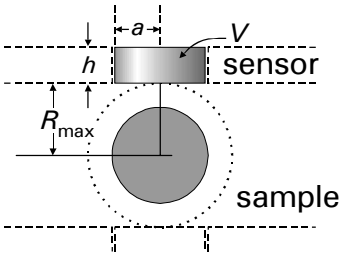

Figure 2.2. Sensor magnet dimensions and definition of R_{max}. Dotted lines denote the positions of other magnets in the BOOMERANG assembly.

$$\kappa_F = \frac{a^2 R_{max}}{2} \left(\frac{1}{\left[(R_{max} + h)^2 + a^2\right]^{3/2}} - \frac{1}{\left[R_{max}^2 + a^2\right]^{3/2}} \right). \tag{2.5}$$

2.1 Optimization of the Sensor Magnet

We consider as "optimal" the sensor magnet that maximizes the force signal-to-noise ratio,

$$SNR_{BOOM} = F_{z,rms} / F_N , \tag{2.6}$$

the ratio of the root-mean-square (rms) signal force $F_{z,rms} = \left(w/\sqrt{2}\right) F_z$, less by $\sqrt{2}$ than the dc force of Equation (2.2) and scaled by the Fourier component of the

inversion scheme used (which is $w = 4/\pi \approx 1.27$ for square-wave modulation of the longitudinal magnetization), and a time-average "noise force," F_N. The predominant noise source over a wide range of conditions is the Brownian motion of the sensor magnet. At a given temperature T, the corresponding average noise force is given by[2,3]

$$F_N = \sqrt{4k_B T \alpha \Delta f} \tag{2.7}$$

in the measurement bandwidth Δf, which is $\Delta f = 1/4T_{1a}$ in the present case[†]. The damping parameter, α, is the proportionality constant between the dissipative (frictional) force and the instantaneous velocity of the sensor magnet. This quantity may be written

$$\alpha = 2m/\tau, \tag{2.8}$$

where m is the motional mass of the oscillator, which is ideally dominated by the mass of the magnet, and where τ is the oscillator's "damping time," the time required for its amplitude to decay to $1/e \approx 36.8\%$ of its initial value after excitation by an impulse.

Empirical evidence from our prototype BOOMERANG spectrometer[4] suggests that damping due to eddy currents induced in the conducting magnets by virtue of their relative motion makes the largest contribution to the damping rate $\gamma = 2/\tau$.

[†] We define the bandwidth as $\int_0^\infty |Z(f)|^2 df \Big/ |Z(f_{max})|^2$ for a system or process with impedance or transfer function $Z(f)$ in accordance with theory[3] that leads to (2.7).

Estimates of this damping rate for the case of cylindrical symmetry are made in Appendix C. The functional form of the damping rate is complicated and not particularly instructive, and it depends much more strongly on other factors, such as the size and shape of the gap between the sensor and annulus, than it does on *a* and *h*. For that reason we leave the explicit dependence of τ on *a* and *h* out of the present optimization.

More importantly, we conclude in Appendix C that τ is scale-invariant. We write

$$\alpha = 2\left(\eta\pi a^2 h\right)/\tau \tag{2.9}$$

for the damping constant, in accordance with a motional mass dominated by a cylindrical magnet with density η. After appropriate substitutions, we then find the maximum of SNR_{BOOM} in the usual way, by differentiating Equation (2.6) with respect to both *a* and *h* and setting derivatives equal to zero. The result is a set of dimensions ($a \approx 0.59\,R_{\max}$, $h \approx 0.53\,R_{\max}$, corresponding to $\kappa_F \approx -0.072$, the sign indicating a downward force) that maximize sensitivity. It should be noted, however, that the sensitivity

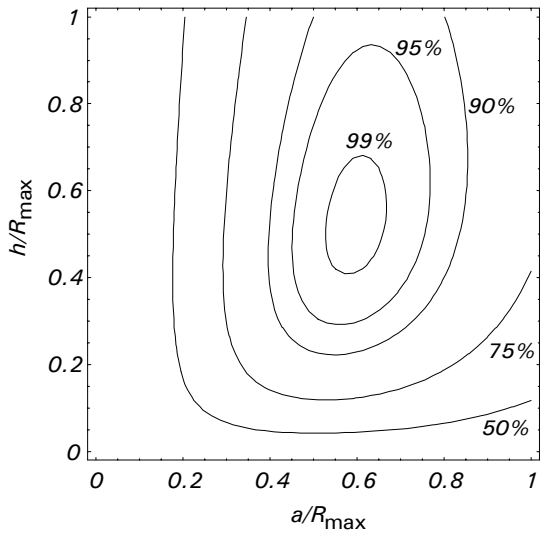

Figure 2.3. Signal-to-noise ratio (*SNR*) versus scaled radius *a* and height *h* of the sensor magnet. The contours show *SNR* relative to the *SNR* of the optimal design at $a/R_{\max} = 0.59$ and $h/R_{\max} = 0.53$. The *SNR* is not a sharply peaked function of either dimension.

figure of merit, as a function of *a* and *h*, is not sharply peaked (see Figure 2.3), and so some latitude exists in playing off sensitivity against homogeneity. The sensor magnet in Figure 2.2 is drawn with the above values for *a* and *h* relative to R_{max}.

We now turn to the scaling, relative to a linear dimension *r* of the sample-plus-optimized-detector, of the signal-to-noise ratio. As regards the signal, the only scale-dependent parameters appearing in Equation (2.3) are the sample's volume and R_{max}. The signal force thus scales as r^2. As regards noise, the conclusion of Appendix C, namely, the scale-invariance of the damping rate, makes α scale as r^3, and so SNR_{BOOM} is predicted to scale as $r^{1/2}$. This conclusion is based on the experimentally observed dominance of eddy-current damping at the prototype size scale. As this damping rate is scale-invariant, the $r^{1/2}$ law will hold as size scales are reduced until other mechanisms (for example, thermoelastic damping, surface losses, or so-called "anchor losses" due to phonon radiation out of mechanical supports) become more important. These damping mechanisms are the subject of much recent scrutiny in the nano-oscillator literature[5-7], and they are treated in the context of BOOMERANG by Madsen[4]. The very favorable $r^{1/2}$ scaling is in marked contrast to sensitivity scaling in inductive detection, to which we now turn.

2.2 Inductive Detection

For direct comparison to BOOMERANG, we assess sensitivity in inductive detection in the same way, by defining the signal-to-noise ratio,

$$SNR_{INDUCT} = V_{rms}/V_N\,, \tag{2.10}$$

in terms of a measured quantity, the rms electromotance V_{rms} in the coil, which is proportional to the magnetization of the sample. During detection, the sample's magnetization drives an electrical oscillator (an *LC* circuit tuned near the Larmor frequency of the target spins). The time-average noise voltage, V_N, is usually dominated by Johnson noise (thermal voltage fluctuations) in the resistive coil, but can also include contributions from dielectric losses in tuning capacitances and, for electrically lossy samples such as living tissue or solutions with electrolytes at physiological concentrations, induction losses in the sample. The average noise electromotance at a given temperature T is

$$V_N = \sqrt{4k_B TR\Delta f} \tag{2.11}$$

in the measurement bandwidth Δf. Here, R denotes the total resistance of the circuit at the Larmor frequency. The ohmic resistance in a conductor can be substantially larger at radio frequencies than at dc due to the skin effect, the tendency of rapidly oscillating currents to flow only within a shallow depth near the surface of a conductor. As a point of reference, the skin depth in room-temperature copper coils (with conductivity $\sigma = 5.8\times10^7\ \Omega^{-1}\text{m}^{-1}$ and permeability $\mu \approx \mu_0$) at $\omega/2\pi = 200\,\text{MHz}$ is[8]

$$\delta = \left(\frac{2}{\omega\sigma\mu}\right)^{1/2} \approx 4.7\mu\text{m}\,. \tag{2.12}$$

The bandwidth Δf of the measurement can be maximized and V_N minimized by prolonging the magnetization during detection with pulsed spin locking[9], in which the NMR circuit is driven by the sample's precessing magnetization during

the windows of a pulse sequence. Loss of magnetization then takes place exponentially with time constant $T_{1\rho}$, the rotating-frame relaxation time, which can be substantially larger than T_2, the transverse relaxation time. The bandwidth for the signal is then $\Delta f = b \times 1/4T_{1\rho}$, where the factor b, which accounts for the fact that the rf preamplifier is effectively decoupled from the signal for part of the time following pulses to avoid saturation and damage, can be substantially larger than unity. As a best case, $b = 1$ is used in the numerical examples that follow.

Since the detected signal is the electromotance induced in the detection coil by time-varying magnetization, the detector in this case is actually sampling the *electric* field induced by the sample. This fundamental detection process, the analogue of detecting the static force between two dipoles considered in section 2.0, is shown in Figure 2.4. An element of a conductor is positioned in the field of the magnetic dipoles in the sample, which are sources of electric field when they reorient in response to applied magnetic fields (*e.g.*, during precession). The electric field induced at **r** by the precessing magnetization may be obtained by taking the time derivative of the magnetic vector potential **A**(**r**) induced at **r** by a magnetic moment $\boldsymbol{\mu}_s$:

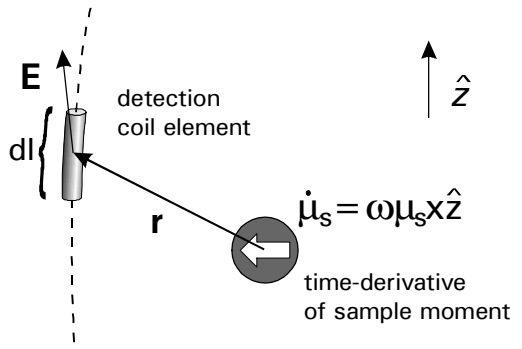

Figure 2.4. Electric field near a sample dipole with time-varying moment μ_s at the position of a detection coil element **dl**. The time-derivative vector is shown — the moment vector μ_s is out of the plane of the page for samples containing spins with positive magnetogyric ratios.

$$\mathbf{E}(\mathbf{r}) = -\frac{\partial}{\partial t}\mathbf{A}(\mathbf{r}) = -\frac{\partial}{\partial t}\left(\frac{\mu_0}{4\pi}\frac{\boldsymbol{\mu}_s \times \hat{\mathbf{r}}}{r^2}\right) = \frac{\mu_0}{4\pi}\frac{\hat{\mathbf{r}} \times \dot{\boldsymbol{\mu}}_s}{r^2} = \frac{\mu_0}{4\pi}\omega\frac{\hat{\mathbf{r}} \times (\boldsymbol{\mu}_s \times \hat{\mathbf{z}})}{r^2}. \qquad (2.13)$$

The last equality is true for magnetic dipoles precessing in the *xy*-plane perpendicular to $\hat{z}$ at angular frequency ω. For a sample of finite size, we replace $\boldsymbol{\mu}_s$ by $\mathbf{M}_s(\mathbf{r}_s)dV_s$, where $\mathbf{M}_s$ is the sample's magnetization at position $\mathbf{r}_s$ within the sample, and integrate over the sample volume dV_s. The result for a uniformly magnetized spherical sample with $\boldsymbol{\mu}_s$ along the *y*-axis is

$$\mathbf{E}(\mathbf{r}) = \frac{\mu_0}{4\pi}\omega M_s V_s \frac{\hat{\mathbf{r}} \times \hat{\mathbf{x}}}{r^2}. \qquad (2.14)$$

The electric field of Equation (2.14) can be viewed as a field of force, the analogue of the force field acting on magnetic dipoles in Figure 2.1. Here, the electric field acts on point charges, which are the electrons in the conducting coil. Figure 2.5 shows a density plot of the force field, with its strength indicated by color. The picture strongly suggests that a solenoid wound around the sample is an ideal detector.

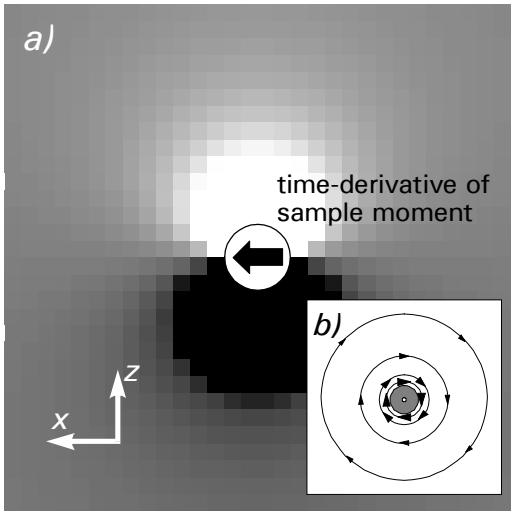

Figure 2.5. a) Density plot of the electric field near a sample with time-varying magnetization. The time derivative of the magnetization is as shown. The electric field is perpendicular to the page for all points in the plane of the page. b) View of the electric field from the side, along the axis of $\dot{\mu}_s$.

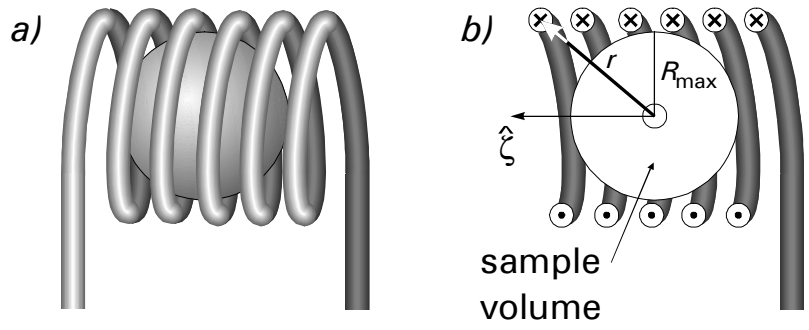

Figure 2.6. Inductive detector model. a) Sample in an NMR induction coil. b) Internal view with position **r** of the coil element defined. $\hat{\zeta}$ is a unit vector along the direction of the time derivative of the sample's magnetization.

Figure 2.6 shows a solenoidal coil wound around a spherical sample with a distance of closest approach, R_{max}, defined as shown. As in BOOMERANG, R_{max} is ideally dominated by the sample's radius, but technical considerations, such as the homogeneity of applied rf fields, can demand that R_{max} exceed the sample's radius by tens of percent and usually much more. The amplitude V of the oscillating electromotance is obtained by integrating Equation (2.14) over the coil. While the relevant integration was over a detector magnet volume in BOOMERANG, in this case, it is a line integral along a current path C:

$$V = \int_C \mathbf{E}(\mathbf{r}) \cdot \mathbf{dl} \,. \tag{2.15}$$

The result for any geometry can be written

$$V = \kappa_V \mu_0 V_s M_s \omega / R_{max} \,, \tag{2.16}$$

where

$$\kappa_V = \frac{R_{max}}{4\pi} \int \frac{\mathbf{r} \times \hat{\boldsymbol{\zeta}} \cdot \mathbf{dl}}{r^3} \tag{2.17}$$

is a shape factor for the coil, the analogue of κ_F, and $\hat{\boldsymbol{\zeta}}$ is the unit vector along $\dot{\boldsymbol{\mu}}_s$. For a helical *n*-turn coil of length 2*g* and radius r_c, the shape factor is

$$\kappa_V = \frac{nR_{max}}{\sqrt{r_c^2 + g^2}}. \qquad (2.18)$$

At sufficiently low frequencies, one could quantify resistive losses in the coil by setting

$$dR = \rho \frac{dL}{A} \qquad \text{or} \qquad dR = \rho \frac{dL}{p\delta}, \qquad (2.19a,b)$$

where ρ is the coil's resistivity and *A* it's cross-sectional area, and integrating over the length *L* of the unwound conductor. In Equation (2.19b), the cross-sectional area is replaced by an effective area $p\delta$, the product of the skin depth δ and a cross-sectional perimeter *p*. With appropriate substitutions, Equation (2.10) could then be used to optimize the dimensions of the solenoid. At commonly used radio frequencies, however, the situation is complicated by "proximity effects," the inductive and capacitive effects of currents in one part of the coil on other parts. These can be accounted for with a phenomenological proximity-effect factor[10-12] $\sigma \approx 3$. Optimization for the case of a (roughly spherical) human head yields an optimal winding geometry for a solenoid, as shown in Figure 2.7. While the size scale used in this optimization is far from the

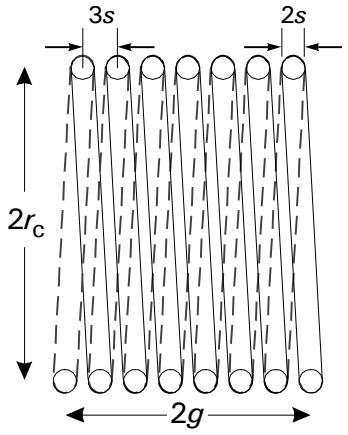

Figure 2.7. Dimensions for optimal NMR coil according to Hoult and Lauterbur[10].

microcoil designs that are our present concern, the aspect ratio $g/r_c = 0.7$ turns out to be consistent with intuition from Figure 2.5 and with results of the simpler optimization suggested above, and we shall use the dimensions of Figure 2.7 in the numerical examples that follow.

Using Equations (2.11) and (2.16), the latter reduced by the factor $\sqrt{2}$ as befits an rms electromotance, we may write Equation (2.10) as

$$SNR_{\mathrm{INDUCT}} = \frac{\kappa_V \mu_0 V_s M_s \omega / R_{\max}}{\sqrt{8 k_B T R \Delta f}}, \tag{2.20}$$

This is to be compared to the expression for BOOMERANG, which can be written

$$SNR_{\mathrm{BOOM}} = \frac{\kappa_F w \mu_0 V_s M_s M_d / R_{\max}}{\sqrt{8 k_B T \alpha \Delta f}}. \tag{2.21}$$

As we have already remarked, SNR_{BOOM} scales as $r^{1/2}$. We can similarly analyze SNR_{INDUCT}. The scale-dependent factors in the numerator of Equation (2.20) are the sample's volume and $R_{\max}$, and so we find that the signal electromotance scales as r^2. In the size regime where the coil's windings are larger than the skin depth, the resistance R, which is proportional to the conductor's total length divided by its cross-sectional perimeter, is scale-invariant. In accordance with Equation (2.20), in this regime SNR_{INDUCT} scales as r^2. At smaller scales, where current flows more uniformly through wires that are small in comparison to the skin depth, the resistance is proportional to total length and inversely proportional to cross-sectional area, and it therefore scales inversely with r. In that case SNR_{INDUCT} scales as $r^{5/2}$. These scaling relations are confirmed by the observations of Peck *et*

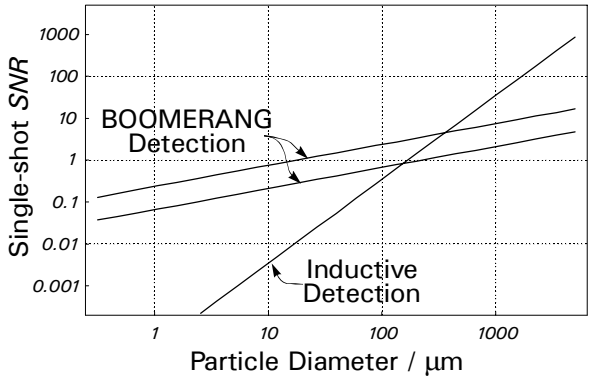

R_{max}	34 μm
sample mass	0.3 μg
# of spins	$6x10^{13}$
detector mass	0.2 μg
magnetization	2 T/μ_0
frequency	500 Hz
ring-down times	80 ms, 1 s
coil x-section	15 μm
coil diameter	83 μm
coil length	58 μm
# of turns	6

Figure 2.8 SNR and scaling for inductive detection and BOOMERANG. Signal-to-noise ratios are estimated for natural-abundance (4%) ^{29}Si NMR at 17 MHz in a 2T field at 150 K. The sample is scapolite, a siliceous mineral believed to be present in martian soil. The simulation is motivated by a study of low-power spectrometers for *in-situ* planetary exploration. The parameters at right are for the hypothetical optimized inductive and BOOMERANG detectors for a 60 μm sample, and the curves at left are based on the scaling relations described in the text. A one-second relaxation time is assumed for the magnetization, and two ring-down times are chosen for the BOOMERANG curves. The 80 ms time has been demonstrated experimentally at the millimeter scale, and, at fields higher than the 0.66 T of the prototype and with careful attention to eddy-current suppression, 1 s ring-down times are anticipated.

al., who report *SNR* per unit volume of r^{-1} and $r^{-1/2}$ in NMR experiments in microcoils with diameters above and below ~250 μm at 200 MHz (4.7 T)[13].

This prediction that SNR_{BOOM} decreases substantially more slowly with size than does SNR_{INDUCT} suggests that BOOMERANG will have superior sensitivity at and below a sufficiently small size scale. In Figure 2.8, SNR_{BOOM} and SNR_{INDUCT} are estimated and plotted over 5 orders of magnitude in sample size for a ^{29}Si NMR spectrum of the mineral scapolite. This example is motivated by a hypothetical mineralogical study with a low-power spectrometer transported to Mars on a space probe. The simulated device is optimized at each scale, and the parameters used in the simulation are listed the accompanying table.

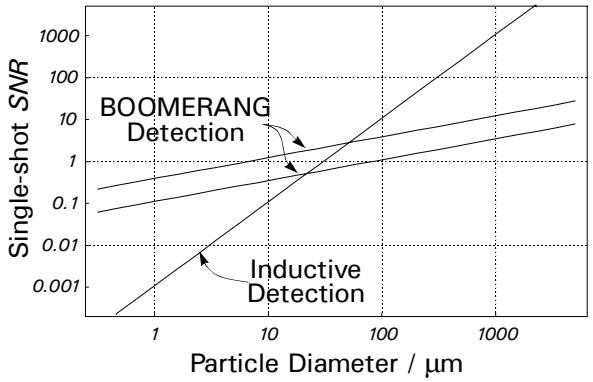

R_{max}	34 μm
sample mass	0.17 μg
# of spins	$2x10^{12}$
detector mass	0.2 μg
magnetization	2 T/μ_0
frequency	500 Hz
ring-down times	80 ms, 1 s
coil x-section	15 μm
coil diameter	83 μm
coil length	58 μm
# of turns	6

Figure 2.9 SNR and scaling in proton NMR. Signal-to-noise ratios are estimated for ^{1}H NMR at 500 MHz and 310 K. The sample is a crystal of a hypothetical 50 kD protein, and the SNR is for a single proton site per molecule, or perhaps a ^{13}C label which has been polarization-enhanced and indirectly detected. As in Figure 2.8, the parameters at right are for optimized inductive and BOOMERANG detectors for a 60 μm sample, and the curves at left are based on the scaling relations described in the text. A one-second relaxation time is assumed for the magnetization, and again 80 ms and 1 s are chosen for the oscillator ring-down times. The graphs show that, even for this case that is most favorable for inductive detection, there is a useful size range where BOOMERANG methods are predicted to exhibit superior sensitivity.

While the scaling relations apply to all nuclei, the size scale below which BOOMERANG's sensitivity is predicted to exceed that of inductive detection will depend on the magnetogyric ratio of the target spin and on the strength of the field. The Larmor frequency ω, which appears in SNR_{INDUCT} (2.20), is absent in SNR_{BOOM} (2.21), and so the relative advantage of BOOMERANG is greater at a given scale for nuclei with small magnetogyric ratios at fixed field, or at lower fields for a given nuclide. The case most advantageous to inductive detection (with the exception of NMR of tritium, whose magnetogyric ratio exceeds the proton's by 7%) is proton spectroscopy in high field. Figure 2.9 shows that, even in the 11.7 T field of a commercial 500 MHz superconducting magnet, BOOMERANG's sensitivity is preferable in samples with R_{max} below about 20-50 μm.

The foregoing motivates construction of a BOOMERANG spectrometer at the sub-millimeter scale, and efforts toward microfabrication of BOOMERANG spectrometers are detailed elsewhere[4,14]. But even with the $r^{1/2}$ scaling of SNR_{BOOM}, sensitivity is still a challenge at smaller scales, and so a proof-of-concept instrument optimized for 3 mm samples was constructed. That instrument is subject of Chapter 3.

2.3 A Note About Reciprocity

The integrand in Equation (2.15) may be interpreted in two ways. We have already used it to describe the electric field induced at the site of a conductor by a time-varying magnetic dipole. With the help of Equation (2.13), this integrand may be rewritten

$$\mathbf{E}(\mathbf{r})\cdot\mathbf{dl} = -\frac{\partial}{\partial t}\left(\frac{\mu_0}{4\pi}\frac{\boldsymbol{\mu}_s\times\hat{\mathbf{r}}\cdot\mathbf{dl}}{r^2}\right) = +\frac{\partial}{\partial t}\left(\boldsymbol{\mu}_s\cdot\frac{\mu_0}{4\pi}\frac{\hat{\mathbf{r}}'\times\mathbf{dl}}{r^2}\right) = -\frac{\partial}{\partial t}\left(\boldsymbol{\mu}_s\cdot\mathbf{d}\tilde{\mathbf{B}}_1\right) \qquad (2.22)$$

where $\hat{\mathbf{r}}' = -\hat{\mathbf{r}}$ is the unit vector pointing from the *current element* **dl** to the *sample dipole* $\boldsymbol{\mu}_s$. $\mathbf{d}\tilde{\mathbf{B}}_1$ is the element of magnetic field induced at $\boldsymbol{\mu}_s$ per unit current flowing through **dl**. We can thus recast the equations that permit us to calculate the induced electromotance by exchanging the roles of the "source" and "observation point." This is a reciprocity relationship[8]. The right-hand side of Equation (2.22) has been the standard means of calculating signal-to-noise ratios in NMR since Hoult and Richards introduced it in 1976[15]. One can calculate (or measure) a local sensitivity

to magnetic moments by integrating $\mathbf{d}\tilde{\mathbf{B}}_1$ over the NMR coil, and this can be useful in evaluating imaging apparatus.

A similar analysis can be applied to force detection. For a differential sample moment $\mathbf{d}\boldsymbol{\mu}_s$, Equation (2.1) may be written in two ways:

$$\mathbf{dF} = \nabla(\mathbf{B}_s \cdot \mathbf{d}\boldsymbol{\mu}_d) = \nabla\left(\frac{\mu_0}{4\pi}\boldsymbol{\mu}_s \cdot \left(\frac{3\hat{\mathbf{r}}\hat{\mathbf{r}} - 1}{r^3}\right) \cdot \mathbf{d}\boldsymbol{\mu}_d\right) = -\tilde{\nabla}(\boldsymbol{\mu}_s \cdot \mathbf{dB}_d) = -\boldsymbol{\mu}_s \cdot \mathbf{d}\left(\tilde{\nabla}\mathbf{B}_d\right), \quad (2.23)$$

which are related by the antisymmetry of the gradients (∇ and $\tilde{\nabla}$) of the dyadic $(3\hat{\mathbf{r}}\hat{\mathbf{r}} - 1)/r^3$ with respect to the coordinates of the detector and sample dipoles, respectively. The parameter $\mathbf{dG} = \mathbf{d}\left(\tilde{\nabla}\mathbf{B}_d\right)$ is the change in the magnetic field at the *sample* (due to the detector element $\mathbf{d}\boldsymbol{\mu}_d$) per unit displacement of the flexible detector along the "detection coordinate," *z*. That this reciprocity parameter **dG**, the equivalent of $\mathbf{d}\tilde{\mathbf{B}}_1$ in inductive detection, has units of magnetic field gradient (T/m) is an artifact of the detection coordinate's units, which are length (m) in the case we have treated here. The displacement may also be an angle, as we shall see in Chapter 5 when the subject of torsional oscillators is taken up.

References

1 G. M. Leskowitz, L. A. Madsen, and D. P. Weitekamp, *Sol. St. Nucl. Magn. Reson.* **11,** 73 (1998).

2 S. Chandrasekhar, *Rev. Mod. Phys.* **15,** 1-89 (1943).

3 C. W. McCombie, *Rep. Prog. Phys.* **16,** 266-320 (1953).

4 L. A. Madsen, Ph. D. Thesis, California Institute of Technology, 2002.

5 R. Lifshitz and M. L. Roukes, *Phys. Rev. B* **61,** 5600-5608 (2000).

6 M. L. Roukes, in *Solid-State Sensor and Actuator Workshop* (Hilton Head Island, SC, 2000).

7 K. Y. Yasamura, T. D. Stowe, E. M. Chow, T. Pfafman, T. W. Kenny, B. C. Stipe, and D. Rugar, *J. Microelectromech. Sys.* **9,** 117-125 (2000).

8 P. Lorrain, D. R. Corson, and F. Lorrain, *Electromagnetic Fields and Waves*, 3rd ed. (W. H. Freeman and Co., New York, 1988).

9 D. P. Weitekamp, *Adv. Magn. Reson.* **11,** 111 (1983).

10 D. I. Hoult and P. C. Lauterbur, *J. Magn. Reson.* **34,** 425-433 (1979).

11 B. B. Austin, *Wireless Eng. Exp. Wireless* **11,** 12 (1934).

12 F. E. Terman, in *Radio Engineer's Handbook*, 1st ed. (McGraw-Hill, New York, 1943), pp. 73-90.

13 T. L. Peck, R. L. Magin, and P. C. Lauterbur, *J. Magn. Reson. B* **108,** 114 (1995).

14 T. George, *et al*., in *IEEE Aerospace Conference* (Big Sky, Montana, 2001).

15 D. I. Hoult and R. E. Richards, *J. Magn. Reson.* **24,** 71 (1976).

Chapter 3: BOOMERANG Prototype

3.0 Overview

This chapter details the construction of a prototype BOOMERANG spectrometer optimized for detection of NMR from solid and liquid samples contained in a 3 mm diameter sample volume. Figure 3.1 shows a block diagram of the prototype. The heart of the spectrometer is the magnet assembly, which is

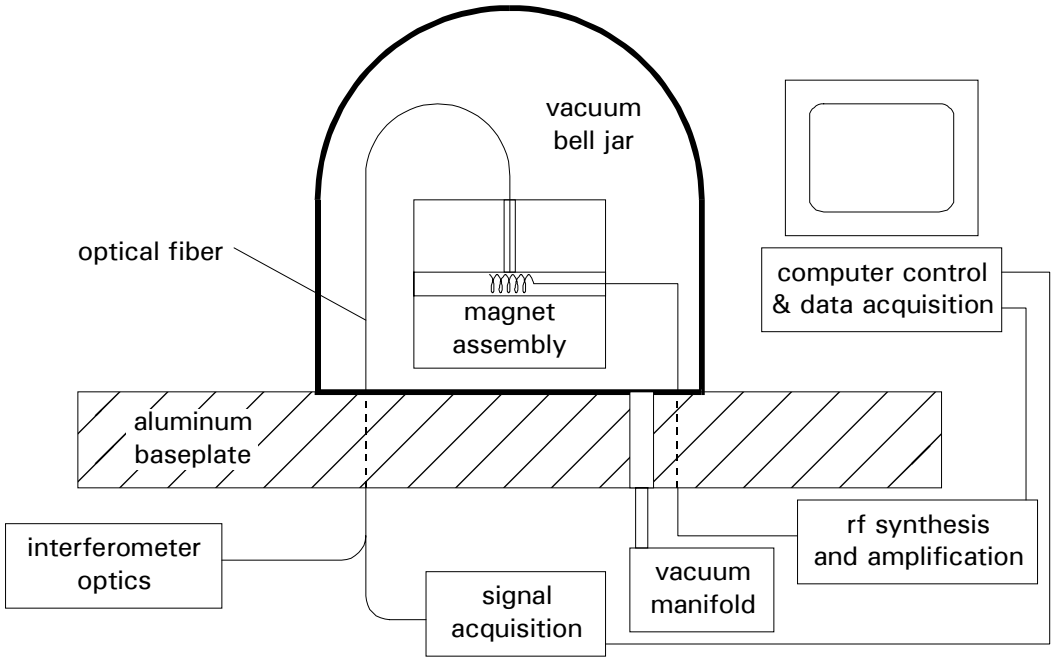

Figure 3.1. Block diagram of the BOOMERANG prototype.

described in section 3.1. This assembly provides a homogeneous field for a sample that is placed inside a solenoid, which is situated underneath a sensor magnet (not shown) inside the assembly. The sensor magnet is bound to a single-crystal silicon suspension (also not shown), and this combination forms a mechanical oscillator, which is described in section 3.2. Picometer-scale motions of the oscillator are monitored with the fiber-optic interferometer system described in section 3.3. The oscillator's resonance frequency is typically between 400 and 600 Hz. In order to suppress ambient acoustic noise, the magnet assembly is enclosed in a vacuum bell jar, which is pumped down to below 10^{-5} Torr. The vacuum also serves to suppress viscous damping of the oscillator.

Typically, the effects of viscous damping are observed to become negligible relative to eddy-current damping when the pressure is below about 10^{-3} Torr at room temperature. Under these conditions, the mean free path of molecules in the air is about 76 mm, which is far larger than the dimensions of the sensor magnet. Thus, a continuum model of the rarified atmosphere, which would predict that the air viscosity is independent of pressure[1], does not apply. We observe a modest increase in the ring-down time of the oscillator up to as much as 80 ms as the pressure is reduced below ambient pressure.

The optical signal from the fiber-optic position sensor is filtered, amplified, and digitized (section 3.4). Rf pulses to reorient the sample's magnetization, including the frequency-modulated pulses used to efficiently invert the magnetization during detection, are digitally synthesized, mixed up to the proton or fluorine Larmor frequency in the 25-30 MHz range, amplified, and delivered to an rf

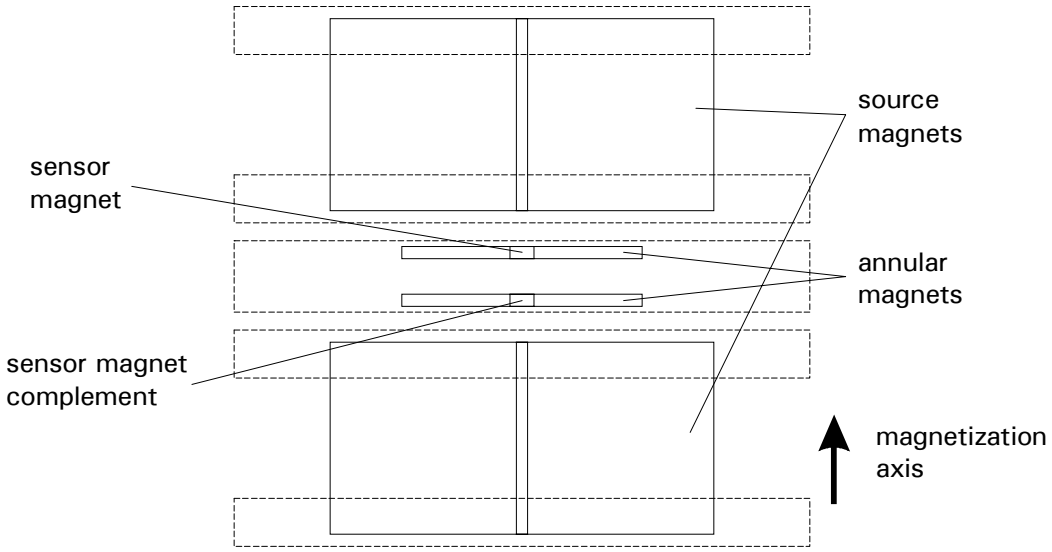

Figure 3.2 BOOMERANG prototype magnet assembly. The drawing is to scale, and magnetic elements, drawn in solid lines, are cylindrically symmetric about an axis that is vertical in the figure. All the magnets are magnetized along their common axis of symmetry. Square, brass brackets to hold the magnets are drawn in dotted lines. Magnetostatic calculations to specify exact magnet dimensions and spacings, as well as designs of bracket and alignment hardware, were performed by Lou Madsen[2].

coil (the solenoid containing the sample) inside the magnet assembly as described in section 3.5. Section 3.6 treats cyclic inversion, which is used to drive the detector oscillator in proportion to the sample's magnetization. The chapter concludes with a detailed assessment of noise sources (section 3.7).

3.1 Magnet Assembly

The defining feature of the BOOMERANG magnetic resonance spectrometer is the magnet assembly, which is designed specifically for field homogeneity. Figure 3.2 shows a schematic of the magnet assembly, which is to-scale. The aluminum base and supports used to hold the magnets in alignment are left out of the diagram for clarity. The "source" magnets (Magnetic Component Engineering, Inc., model N40) are made of neodymium iron boron (NdFeB) magnetized axially to a remanent

magnetization of 1.29 T/μ_0. They are right circular cylinders 2.54 cm high and 5.08 cm in diameter. Both have 1.6 mm holes drilled down the symmetry axis, the upper magnet to accommodate an optical fiber, the lower magnet to preserve reflection symmetry of the magnet assembly.

These source magnets magnetize the four internal magnets, including the sensor magnet. The internal magnets are machined from mu metal (Carpenter Technology Corp. "HyMu 80" alloy). In the field of the source magnets, the internal magnets acquire a magnetization of 0.665 T/μ_0. This value equalizes the normal component of the magnetic induction B across the boundary between the high-permeability mu metal and the air gap for the known geometry of the magnet assembly. This estimate, which falls between the value calculated for an infinitely wide flat disk in the field of the source magnets (0.605 T/μ_0) and the material's saturation magnetization[3] (0.75 T/μ_0) is the result of an iterative magnetostatic self-consistency calculation.

Figure 3.3 shows a plot of the longitudinal component B_z of the static field along the symmetry axis in the 4.8 mm space below the sensor magnet and above its complement. The distance between the annular magnets is fixed, but the distance between the source magnets can be varied somewhat to provide a coarse shimming capability. This procedure also changes the static field, and we have observed fields across the range 0.59-0.73 T. (The magnetization of the sensor magnet changes accordingly.) The three curves in Figure 3.3 are for three positions of the sensor magnet, which is free not only to vibrate longitudinally, but also to come to rest slightly above or below its encircling annulus as a result of static

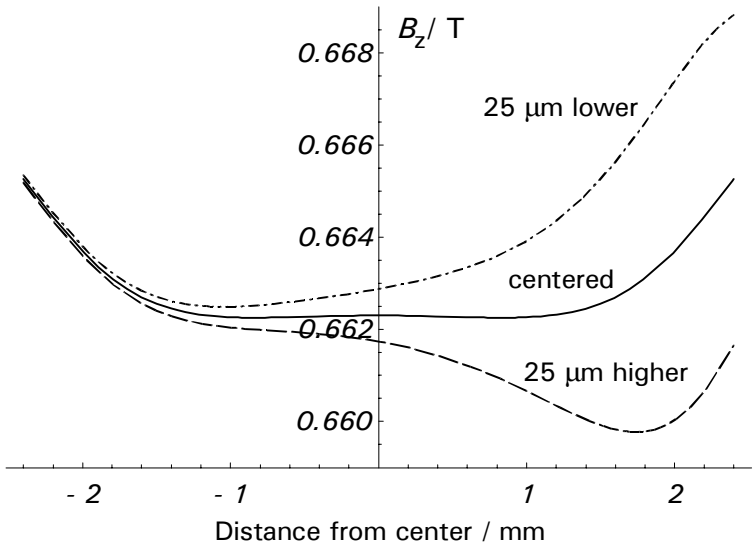

Figure 3.3. Calculation of the field at positions along the symmetry axis in the BOOMERANG prototype. When the sensor magnet is perfectly centered in the annulus, odd-order gradients in the field vanish.

forces from the other magnets. By varying the distance between the source magnets with inserted brass shims, it is possible to align the sensor and annulus to within $\sim$50 μm by careful visual inspection.

The reflection symmetry of the magnet system makes all odd-order gradients (*e.g.*, $\partial B_z/\partial z$, $\partial^3 B_z/\partial z^3$) vanish. The principal design goal was therefore to null the second-order gradient $\partial^2 B_z/\partial z^2$ as best as possible. As is shown in Figure 3.3, the linear term vanishes only when the sensor magnet is well aligned. Figure 3.4 shows three line shapes calculated for the three positions (perfect alignment and 25 μm above and below perfect alignment) of Figure 3.3. These line shapes are calculated by computing the field expected at randomly chosen points in a 3 mm spherical volume, binning the values, and graphing the resulting probability distributions. The simulations show that the total distribution of proton Larmor frequencies over the

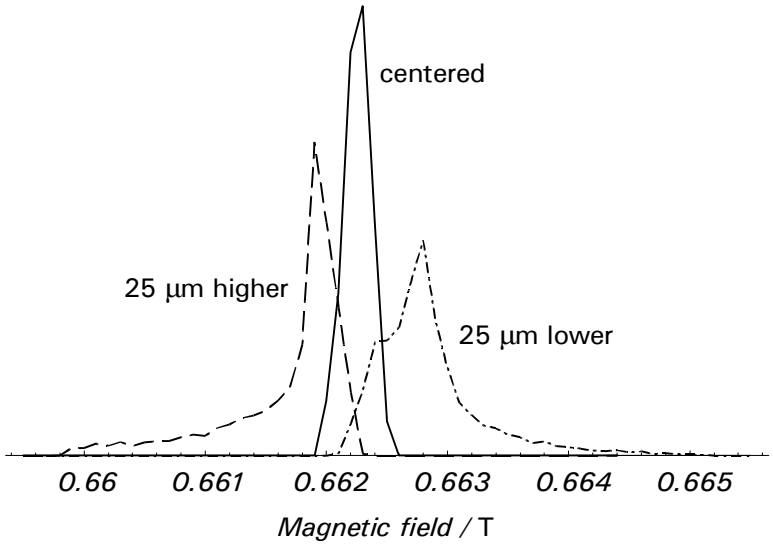

Figure 3.4. Distribution of fields within the sample for three positions of the sensor magnet.

sample is on the order of 28 kHz (6.5×10^{-4} T x 42.6 MHz/T, with full width at half maximum (FWHM) 6 kHz) for a perfectly aligned sensor and that the line width can vary substantially depending on the sensor's alignment. This distribution of Larmor frequencies is compatible with inversion of the entire sample magnetization for the ~50 kHz Rabi frequencies we achieved with our rf system (section 3.5).

Since the force coupling a given nuclear moment to the sensor magnet varies as a function of the moment's position within the sample, the distribution of Larmor frequencies shown in Figure 3.4 must be weighted by a "local sensitivity" in order to properly model the NMR line shape. As shown in Figure 3.5, this weighting distorts the expected line shapes considerably more for spectra taken with the sensor magnet displaced from its most symmetric location.

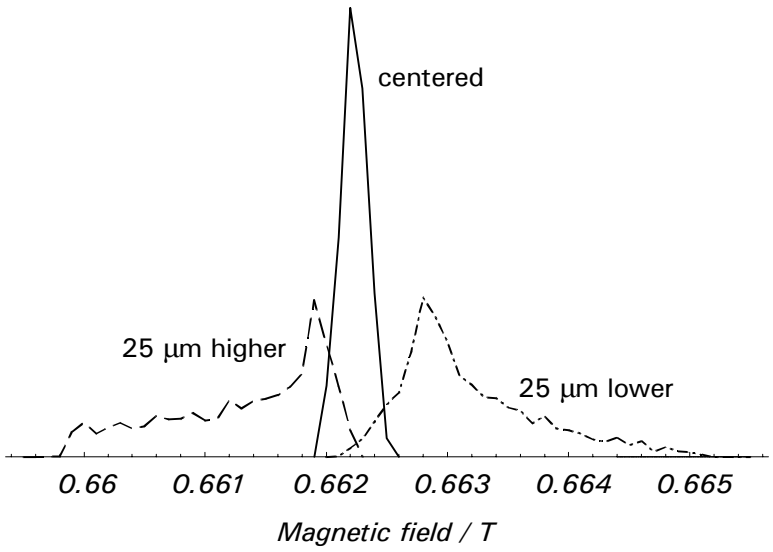

Figure 3.5. Simulated lineshapes for three positions of the sensor magnet adjusted for sensitivity variations in the sample volume. When the sensor is misaligned, extreme values of the field in the NMR line are weighted more significantly.

Figure 3.6 shows a Fourier-transform (FT) ^{1}H NMR spectrum of water taken with the prototype (see Chapter 4 for details). The line widths observed in ^{1}H NMR of water were typically in the range 8-50 kHz, which are consistent with the above simulations. Most of the observed line width can be attributed to the field inhomogeneity due to the presence of the gap between the sensor and the annulus. Indeed, simulation of the distribution of Larmor frequencies for the particular geometry in Figure 3.2 with the sensor radius modified so as to have no gap between the sensor and annulus showed a line width of only 0.6 kHz. Detailed optimization of the homogeneity using the approximation of perfectly axial magnetization, as well as more exact finite-element analyses[2] showed that this line width can be reduced, with careful placement of all the magnets, to well below 1 ppm (28 Hz in the prototype) overall for such no-gap configurations. An important

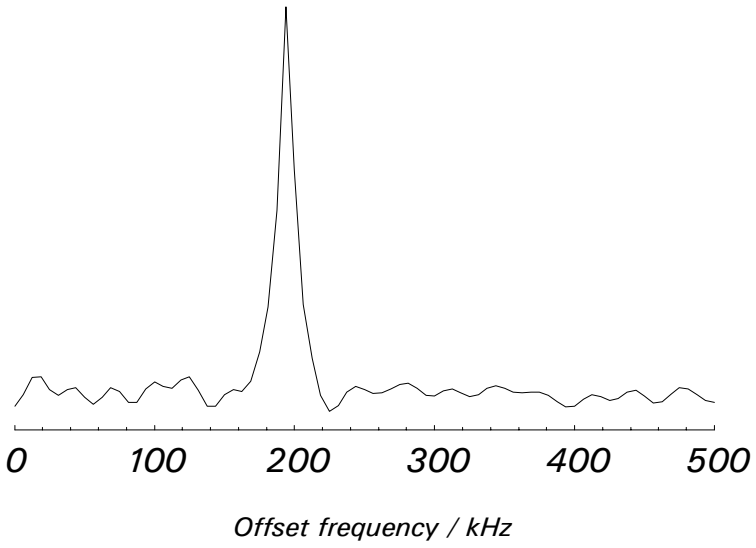

Figure 3.6. FT-NMR spectrum of water measured with the BOOMERANG prototype. The 17 kHz line width is consistent with the model calculation of figure 3.5.

improvement to next-generation BOOMERANG devices will be an active shimming capability based on movement of the magnets, which could be supplemented by a shim coil set as in ordinary NMR. Even at the demonstrated homogeneity (which is more than three orders of magnitude better than would be the case without using the BOOMERANG concept), the line width is sufficient to allow inversion of the entire sample magnetization. This is all that is really required. In the highest-resolution BOOMERANG designs, spectroscopic evolution can take place with the sample placed at a separate location, which is away from the sensor magnet and its surrounding gap, such a location being separately optimized for strict homogeneity (perhaps with coil-based shimming measures), with the sample subsequently shuttled under the sensor magnet for optimal detection[4].

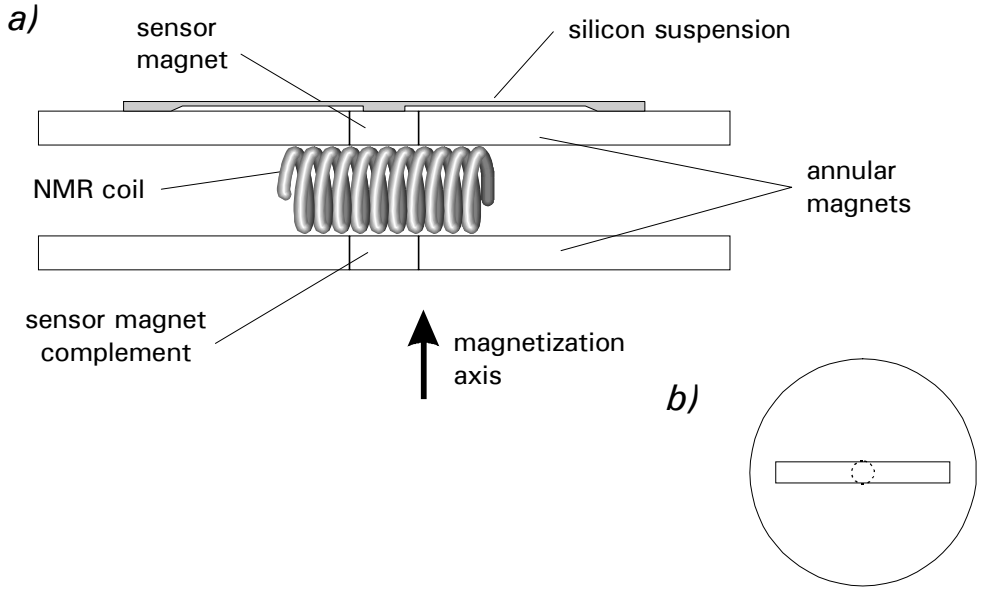

Figure 3.7. BOOMERANG prototype oscillator assembly, with surrounding annular and complement magnets, silicon suspension, and NMR coil. a) Side view, 3x scale. The sensor magnet, 3 mm in diameter and 1.5 mm high, is bound to a 0.22 mm thick rectangular silicon suspension. b) Top view, 1x scale.

3.2 Oscillator

Figure 3.7 shows the center of the magnet assembly with its oscillating silicon beam and sensor magnet. The sensor magnet is affixed to the beam so that it is free to oscillate along the symmetry axis. The sensor magnet's counterpart in the lower half of the assembly is glued inside its annulus, its face flush with that of the annulus. The sensor magnet weighs 83.1 mg, and the silicon beam's total mass is 36.7 mg. The total motional mass for this "fixed-fixed" beam configuration[5] is therefore about $(83.1 + 0.375 \times 0.70 \times 36.7)\,\text{mg} = 92.7\,\text{mg}$ accounting for the $\sim 30\%$ of the silicon beam that is fixed to the annulus and not free to oscillate. When placed between the field magnets, the oscillator's resonance frequency was typically between 400–600 Hz. The frequency of a given oscillator varied by tens

of hertz or more depending on the age of the oscillator, the temperature, and the thickness of the brass shims used to separate the source magnets.

The total spring constant, ~ 897 N/m (for the particular case of the above motional mass and a 495 Hz resonance frequency), is the result of two offsetting effects: a positive elastic spring constant due to the restoring force of the silicon beam and a negative magnetic spring constant due to magnetic forces, primarily between the sensor magnet and its encircling annulus. In the absence of the restoring force of the silicon beam, the sensor magnet is at the "top of a hill" in potential energy when positioned at the center of the annulus[2]. A crude estimate of this contribution to the spring constant can be made by estimating the second derivative with respect to longitudinal displacements of this potential energy, with the sensor modeled as a simple dipole in the field of the annulus. The result is -1380 N/m, which indicates an elastic spring constant of about $+2280$ N/m. The negative magnetic contribution to the total spring constant is an important feature of the BOOMERANG method. While both the elastic and magnetic spring constants (and therefore their sum) should scale linearly with the size of the apparatus, variations in aspect ratios of the silicon suspension should allow some control in the adjustment of the mechanical resonance frequency at a given size scale. This will help to maintain a frequency low enough to permit inversion of the sample magnetization with practical rf power (see section 3.5) as BOOMERANG devices are scaled down. Active measures of controlling the spring constant[2] may further enhance this capability.

The frequency and the ring-down time of the oscillator are experimentally measured by observing the steady-state response to acoustic or magnetic excitation as a function of input frequency. The oscillator is excited by magnetic coupling to the field generated by audio-frequency currents in a nearby excitation coil that is placed temporarily under the magnet. The mechanical response of the oscillator is maximized visually on an oscilloscope while the input frequency is tuned to find the resonance. The line width $\gamma/2\pi$ is obtained by recording those frequencies, one each on the high- and low-frequency sides of the resonance frequency, at which the mechanical response is $1/\sqrt{2}$ times the amplitude at resonance. In cases where the mechanical resonance is particularly sharp, the ring-down time $\tau = 2/\gamma$ of the oscillator can be measured directly by observing the transient response to an impulsive excitation. Typically, the line widths of the best oscillators used in our experiments were in the range 4–6 Hz (ring-down time $\tau = 53–80$ ms).

The damping of the oscillator is probably dominated by eddy currents induced in both the annulus and sensor magnets by their relative motion. This conclusion is based on the observation that greatly widening the gap (by 0.5 cm or more) between the sensor and the annulus substantially lengthens the ring-down time[2]. Calculations in Appendix C show that these (azimuthal) eddy currents are primarily located very close to the edges of the sensor and annulus. Indeed, longer ring-down times are observed with sensor-ring combinations with slightly rounded edges in the sensor/annulus gap. This suggests that some tradeoff may be made between homogeneity and ring-down time. Another strategy for the reduction of eddy currents that we have used with some success is the introduction of radial

slits in the annulus to interrupt the currents. This approach is motivated by common practice in transformer design, in which laminated transformer cores are used to mitigate similar eddy current losses.

The calculation of eddy current damping in Appendix C assumes uniform axial magnetization in both the sensor and the annulus, and it underestimates somewhat the eddy current damping that is actually observed. Radial components in the magnetization would make the calculated eddy currents larger. In magnetic fields that are substantially larger than the ~ 0.66 T field of the prototype, the magnetization of sensor and annulus may more strongly conform to an axial orientation, which may help to reduce eddy current damping.

Another significant issue regarding the oscillator is the drift of its resonance frequency between iterations of the experiment. This is probably due to heating of the oscillator by the applied rf current. The drift over several shots of the experiment can be seen in the plot of Figure 3.8. This density plot records the Fourier transform of a time series, a record of the oscillator's trajectory during driving by magnetization modulated with rf at a frequency (here 442 Hz) that is fixed shot-to-shot. The dark band is the frequency range over which the Brownian motion of the oscillator is strongest, which is within ~ 1 line width of the resonance frequency. This drift can be compensated for in practice by including several "dummy" applications of rf, which brings the oscillator to a steady-state temperature and frequency.

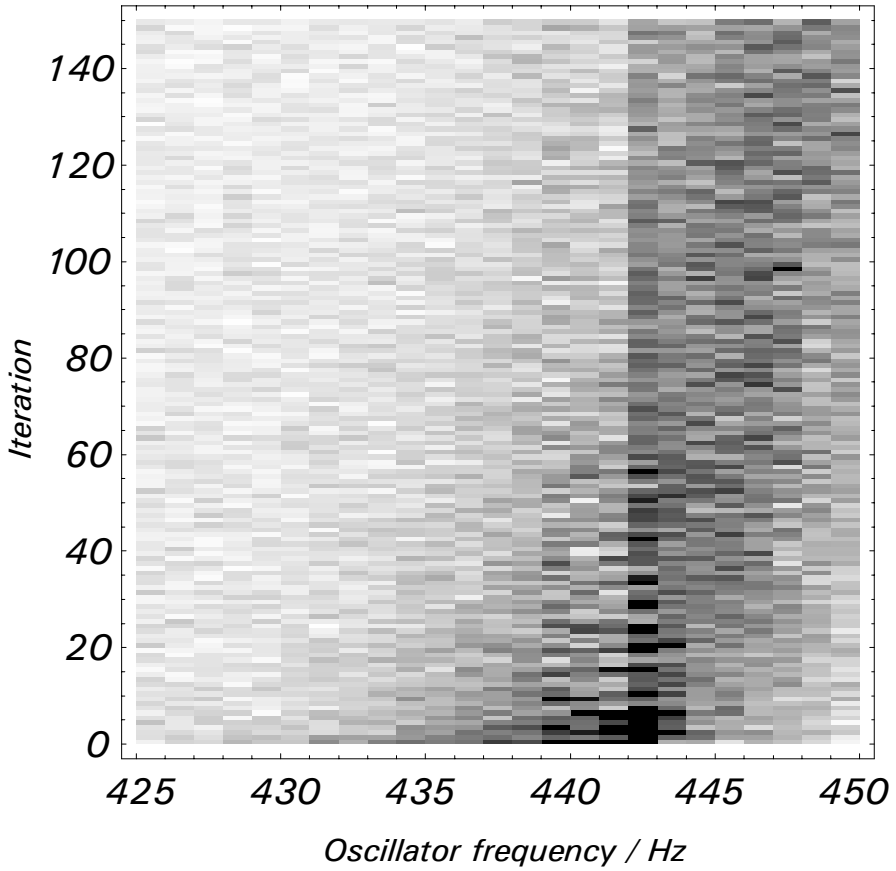

Figure 3.8. Drift over time of the oscillator frequency. In this density plot, intensity in the Fourier transform of a mechanical transient is indicated by color for 150 iterations of the experiment. The broad band, which moves by ~10 Hz over the course of the experiment, is the ~7-Hz-wide signature of the Brownian-motion noise. The narrow, dark feature at 442 Hz is the NMR signal that results from rf frequency modulation during oscillator driving.

Of more concern is the drift of the oscillator *during* a given shot. This can cause phase variations in the signal when the time between the beginning of heat deposition from rf pulses to the onset of the detection period varies from shot to shot in the experiment. Frequency variations of the oscillator were observed in real time by applying an audio-frequency excitation to the oscillator at a fixed frequency slightly (~3 Hz) off resonance and observing the phase shift on an oscilloscope as the natural resonance frequency changed during application of the rf current. The

frequency changed by ~4 Hz during application of rf currents that were typical of the experiments reported in Chapter 4. This is a very substantial fraction of the natural line width of the oscillator, and it was observed to cause significant aberrations in the phases of time-domain NMR signals.

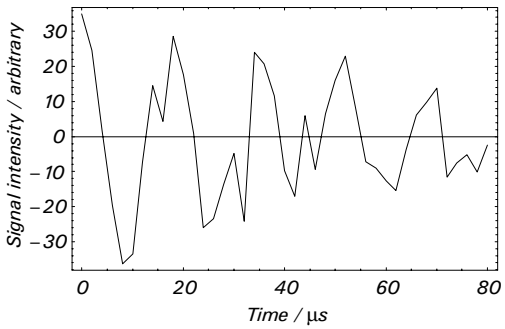

Figure 3.9. ^{19}F Nutation time series showing phase aberrations. The sample is neat fluoroacetonitrile. The signal should show a single decaying cosine.

Figure 3.9 shows the result of a particularly bad nutation experiment. In this figure, deviations from the expected decaying cosine are far above the predicted (section 3.7) and observed base noise level. Ways to account for this in the experiment are the subject of ongoing design efforts. A promising approach is to concurrently excite the oscillator slightly off resonance and observe the phase shift of this signal in real time. This signal can be used to estimate the instantaneous resonance frequency, which can subsequently be used in a fitting procedure. Alternatively, this estimate, or a temperature measurement, can be used in a thermal feedback scheme to stabilize the oscillator's frequency in real time.

3.3 Fiber-Optic Interferometer

The picometer-scale motions of the sensor magnet are monitored with a fiber-optic interferometer[6], which is shown schematically in Figure 3.10. Laser light at 780 nm from a pigtailed multimode diode laser (Sharp model LT023MD, from OZ Optics, Canada) is launched into one arm of a 2x2 fiber coupler (Gould Fiber Optics,

Inc.) through a single-mode optical fiber (5 μm core, 125 μm cladding). The laser is driven by a battery-powered current source for minimum intensity noise. The light is split 50/50 into the coupler's two output arms. One arm goes into a light dump to attenuate destabilizing backscattered light that would otherwise return to the laser arm. Dumping the light in this arm also reduces an undesirable dc offset in the detected photocurrent. The light dump is simply a piece of black felt affixed to the end of the fiber and soaked with pump oil, which serves as an index-matching fluid to further reduce reflections off the fiber end.

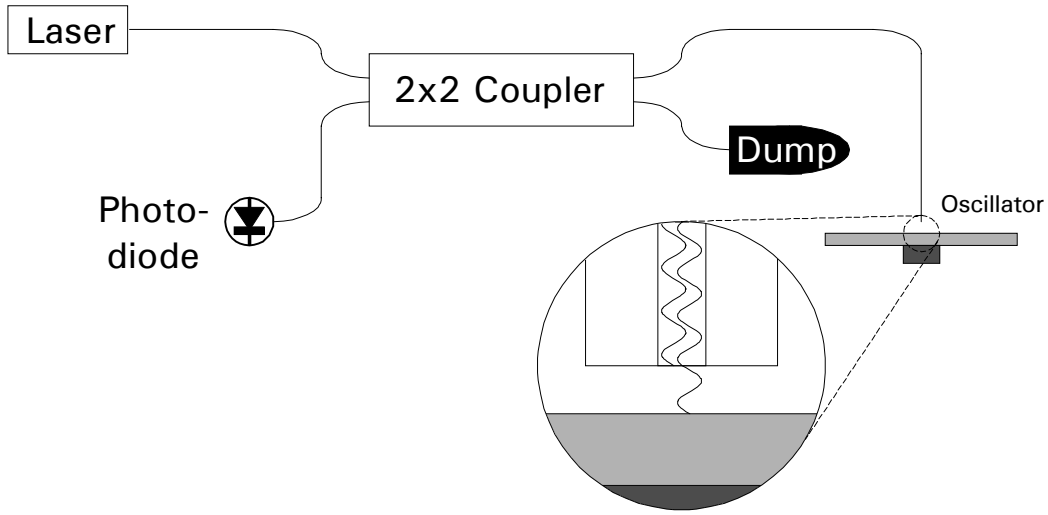

Figure 3.10. Fiber-optic interferometer. A laser diode launches light into one arm of a 2x2 fiber coupler, where it is split between two single-mode fibers. Half of this light goes to a light dump to prevent unwanted reflections. The other half goes into the magnet array through a narrow hole drilled through the center of one NdFeB pole magnet. The end of this fiber is cleaved, and it is brought to within a few microns of the polished surface of the silicon oscillator. Reflections from the glass-air interface and from the polished surface scatter back into the fiber and travel back through the coupler to a photodiode. The displacement of the oscillator is registered as a variation of intensity of the light incident on the photodiode due to interference of these two scattered beams.

The light in the coupler's interferometer arm goes through a vacuum-wall feedthrough, into the vacuum bell jar, and through the hole drilled along the symmetry axis of the upper field magnet. The fiber's face is cleaved flat and

brought to within a few microns of the reflecting surface at the back of the silicon oscillator. The light is reflected from two surfaces — one, the glass-air interface at the fiber end, and the other, the silicon oscillator. If the distance between these two reflecting surfaces is smaller than the coherence length of the laser, then the light reflected back down the fiber toward the coupler is subject to modulation by the interference between these two reflected waves, which depends sinusoidally on the distance between the fiber face and the oscillator. This backscattered light goes back through the coupler, and it is again split 50/50. One half of this light is incident on a photodiode (Seastar model CP-120-20), which is fc-coupled to the fiber. The photodiode is reverse-biased with a 9V battery to improve response and linearity, and the photocurrent is amplified by a current (transimpedance) amplifier (Princeton Applied Research, Model 181). The resulting output voltage is subsequently filtered, amplified, and digitized (section 3.4).

The interferometer-arm fiber is affixed above the source magnet to a clamp-and-spring assembly, which allows the distance between the fiber end and the silicon oscillator to be regulated by applying a voltage to a piezoelectric stack under the clamp. The nominal distance is set to the center of a sinusoidal fringe, where the photocurrent varies linearly with small displacements. Since it is important to maintain this linearity throughout the duration of the experiment, a feedback circuit is used to keep the fiber face near the fringe center[2]. The fringe visibility of the interferometer,

$$V = \frac{I_{max} - I_{min}}{I_{max} + I_{min}}, \tag{3.1}$$

where I_{max} and I_{min} are the maximum and minimum photocurrents, is typically 45-75%.

The sensitivity of the fiber-optic interferometer system is sufficient to observe the Brownian motion of the oscillator at room temperature, and so Brownian motion is the predominant noise source for room-temperature measurements. Figure 3.11 shows the observed noise spectral density over a 90 Hz range that includes the oscillator's resonance. This resonance peak is fit to a Lorentzian line at $\omega/2\pi = 496\,\mathrm{Hz}$ with full-width at half-maximum $\gamma/2\pi = 5.0\,\mathrm{Hz}$. The silicon element of this particular oscillator was part of a structure more complicated than a single fixed-fixed beam, and so the motional mass is difficult to estimate from elementary solid mechanics. The noise spectral density shown is consistent with a motional mass of 139 mg, which is somewhat larger than the 92.7 mg estimated for the simple fixed-fixed beam. Also included in the fit is a frequency-independent noise floor, which is about $0.038\,\mathrm{pm}^2/\mathrm{Hz}$ ($0.195\,\mathrm{pm}/\sqrt{\mathrm{Hz}}$). This exceeds estimates of white noise from the sum of several noise sources quantified in section 3.7 by a factor of four in power and two in amplitude. This excess noise may be due to intensity noise in the laser or possibly residual acoustic noise.

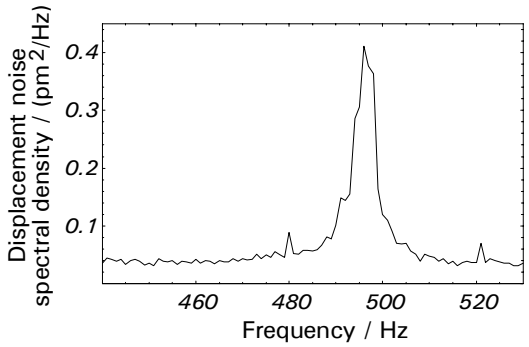

Figure 3.11. Displacement noise spectral density. The peak at the oscillator frequency is due to Brownian motion. The frequency-independent noise floor is somewhat larger than the prediction based on shot noise, Johnson noise in the photocurrent amp, etc., calculated in section 3.7.

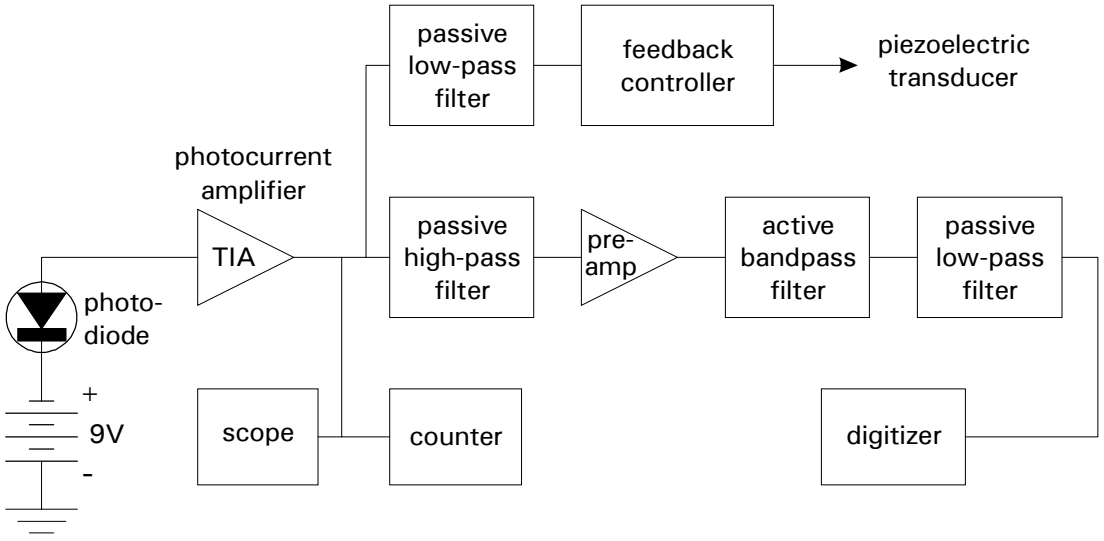

Figure 3.12. Signal acquisition and conditioning. See text of Section 3.4 for details.

3.4 Signal Conditioning and Acquisition

The output of the photocurrent (transimpedance) amplifier is the sum of an audiofrequency voltage due to vibrations of the oscillator and a near-dc level that depends on slow variations of the distance of the fiber face to the silicon oscillator. As shown in Figure 3.12, this output is split. One arm is low-pass filtered, and this near-dc component (below 0.1 Hz) is sent to the input of a feedback circuit, which is designed to maintain a setpoint voltage by driving a piezoelectric stack connected to the fiber support. In the other output arm, the audio-frequency component is high-pass filtered to remove the dc offset and to attenuate a large ~30 Hz interference that arises from acoustic noise exciting a spurious mechanical resonance in the apparatus. The resulting signal is amplified by a factor of 50 or 100 by a preamplifier (Stanford Research, Inc. Model SR552) and then filtered by a

rack-mount bandpass filter (Wavetek Model 442 Dual HI/LO filter). This filter is convenient because its passband can be set with front-panel switches. However, since its output includes some high-frequency electronic noise, its output is filtered through a two-pole low-pass passive (*LC*) filter before digitization. Digitization takes place inside a Pentium-based computer at 2 or 4 kilosamples per second and 16 bits vertical resolution using an ISA-compatible digitization board (Computer Boards, Inc. model CIO-DAS1602). Typically a one- or two-second transient is recorded when the oscillator is driven resonantly by forces exerted by the sample's modulated magnetization.

3.5 Rf System

Figure 3.13 shows the system of synthesizers, mixers, and amplifier that are used to deliver pulses of rf magnetic fields to the sample. The radio-frequency source for the experiments is a Signatec AWG502 arbitrary waveform generator board inside a Pentium-based IBM-PC-compatible computer. The board "clocks out" preprogrammed voltages on two channels at up to 50 megasamples per second, and it has a 64-kbyte data memory and a 256-byte program memory that allows some flexibility in looping of pulse programs. All the pulse sequences described in this thesis are computed and synthesized in real time by a C-language control program between iterations of rf application. These pulse programs are sent to the AWG board where they await a software trigger signal. The output of the AWG board is 8 V peak-to-peak at maximum in the frequency range 2-5 MHz (limited by the Nyquist frequency of the 10 MSample/s rate used in most of the experiments).

This 3 MHz range covers both the proton and fluorine Larmor frequencies in the 0.66 T field when mixed up to the ~28 MHz region with a local oscillator (Programmed Test Sources, Inc. PTS500).

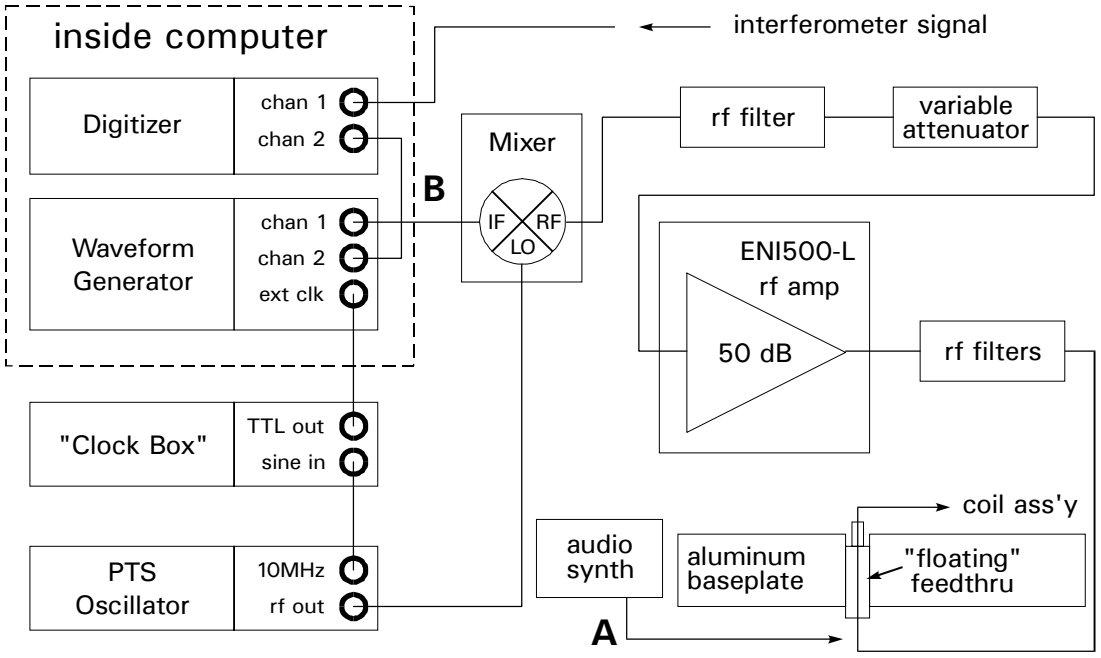

Figure 3.13. RF system as described in the text of section 3.5. At **A**, the NMR coil, which receives filtered rf current from the amplifier during experiments, can also be disconnected from the rf and connected to an audio-frequency synthesizer. This allows application of current at the sensor oscillator's resonance frequency, which can be used to calibrate the interferometric measurement of the oscillator's displacements. At **B**, a sinusoidal reference signal is sent from the AWG to a second channel on the digitizer. This timing channel acts as a phase reference for the detected interferometer signal.

The mixer unit is a collection of Mini-Circuits, Inc., devices configured for single-sideband operation by Lou Madsen[2]. Its output is filtered and attenuated, followed by amplification by 50dB (ENI 3100L or 5100L-NMR). The output from the amplifier is again filtered and then transmitted through a floating-ground feedthrough to the interior of the vacuum bell jar, where it is transmitted through

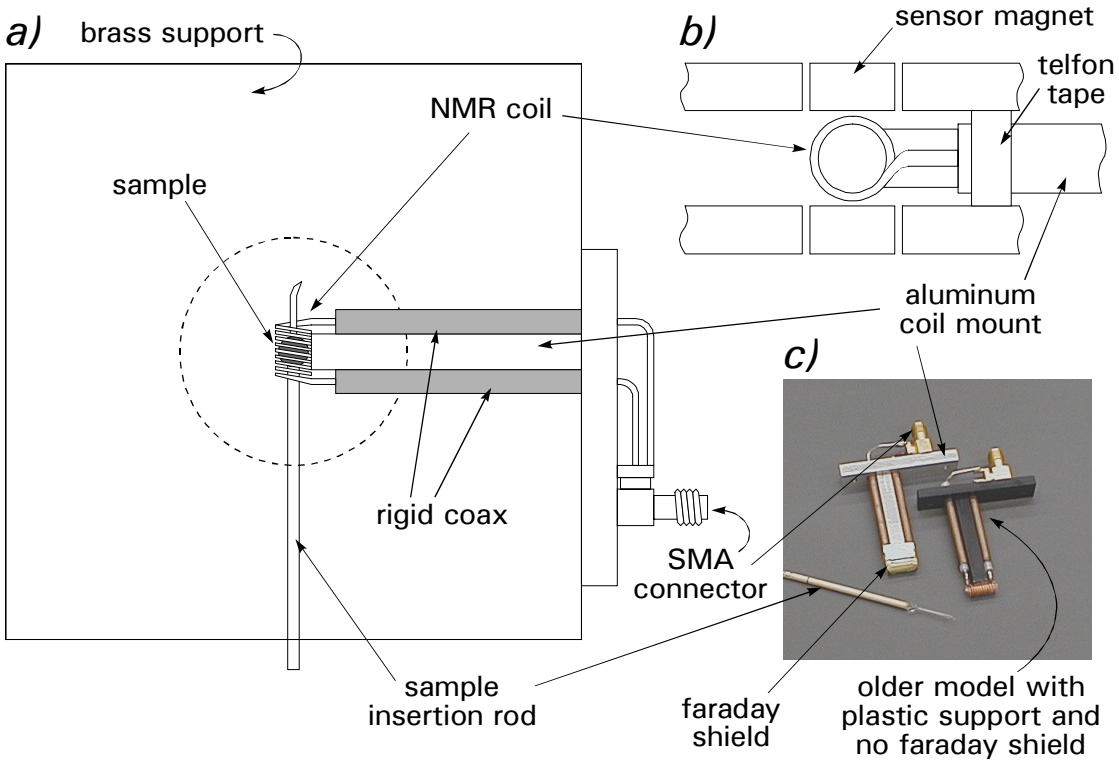

Figure 3.14. Therefore coil assembly. a) Top view. The sample is slid into the coil after the coil mount is installed as shown. b) Side view close-up showing coil underneath sensor magnet. c) Photo of two coil mounts and a liquid sample glued to an insertion rod.

~12 cm of micro-coax cable to an SMA connector on the NMR coil assembly shown in Figure 3.14.

Both the live and rf-ground voltages are brought into the magnet array through shielded rigid coax. The rigid coax that is used has outer and inner conductors made of a non-magnetic, low-permeability copper to avoid distortion of the static magnetic field. The ends of the rigid coax connect to a 9-turn coil that is wound within a beryllia tube and protected by an electric-arc suppressing mixture (GC Electronics Red GLPT Insulating Varnish, diluted with a few drops of toluene for smoother flow around small conductors). In order to get the sample as close as

possible to the moving sensor magnet, the wires of this coil (which are initially 32 gauge) are flattened to 150 μm thick between metal rollers. The beryllia tube has a high thermal conductivity, and in combination with the aluminum support to which it is bonded, it serves to conduct away heat that can change the resonance frequency of the oscillator. The outside of the beryllia tube is covered with a 25 μm thick, grounded Faraday cage to suppress the direct electromagnetic interaction of the coil with the sensor oscillator.

After the magnet assembly is put together[2], the coil assembly is inserted into the magnets so that the coil is directly under the moving sensor magnet. Then the sample, which is typically a liquid in a spherical bulb or a powder packed into a cylindrical tube between magnetically inert plugs, is affixed to a wooden dowel and inserted from another side, along the coil axis (see Figure 3.14).

The NMR coil is usually untuned. Our rf amplifier is strong enough to supply the necessary rf power into an untuned coil at the prototype size scale. This will also easily be the case for microfabricated BOOMERANG devices for low-power remote spectroscopy applications[2,8]. The lack of tuning capacitors, in combination with a direct-digital approach to rf synthesis, allows us to apply multiple pulses on two different nuclei simultaneously on the same channel and also to apply the broad-band frequency-swept pulses (cyclic adiabatic passage) that drive the oscillator during detection with minimal amplitude modulation of the rf current in the coil, which is important to suppress spurious driving of the oscillator.

3.6 Cyclic Inversion with Phase-Cycled Efficient ARP

We have repeatedly referred to cyclic inversion of the sample's magnetization as the means by which oscillating forces are applied to the sensor oscillator in BOOMERANG. This inversion is so important to BOOMERANG that we shall consider it now in some detail. In order to drive the oscillator into mechanical resonance, the nuclear magnetization of the sample is inverted twice per oscillator period τ. This could be done with a train of π-pulses. However, even though the field is designed to be homogeneous, there is still a residual spread of Larmor frequencies, which as we have seen is of order 20 kHz. In order to optimize signal power, the oscillator driving procedure must repeatedly invert these inhomogeneously broadened spins with negligible loss in magnetization over and above losses due to unavoidable relaxation in a time period $\sim T_{1a}$.

We may quantify the needed efficiency of a single inversion process by observing that if each pass loses a fraction ε of the magnetization (in addition to the fraction $\tau/2T_{1a}$ lost to relaxation), then the exponential relaxation time will be decreased from T_{1a} to $\left(\frac{2\varepsilon}{\tau}+\frac{1}{T_{1a}}\right)^{-1}$. If this new relaxation time is to be more than half of T_{1a}, then ε must be less than $\tau/2T_{1a}$, which is 0.001 for $T_{1a} \approx T_1 = 1\mathbf{s}$ and $\tau \approx 1/500\ \text{Hz} = 2\ \text{ms}$. Thus we require that each pass be at least 99.9% efficient in inverting the entire sample magnetization. This limits use of the "sudden" approach of π-pulses (even composite pulses), which have limited spectral range given the required efficiency.

A better approach is adiabatic passage, which is known to be a more efficient means of inverting a population of inhomogeneously broadened spins. In adiabatic passage, the frequency $\omega(t) = \dot{\phi}(t)$ of the rf component of an applied field

$$\mathbf{B}(t) = B_0\hat{\mathbf{z}} + B_1(\hat{\mathbf{x}}\cos\phi(t) - \hat{\mathbf{y}}\sin\phi(t)) \tag{3.2}$$

is swept through Larmor resonance in a time that is short compared to spin relaxation but long compared to a period of spin precession in the "effective field" (see below) in a coordinate frame rotating at the frequency of the applied field. In Equation (3.2) and the following, we leave out a counter-rotating component that is present when linearly polarized rf is used. Let $\{\hat{\mathbf{i}}, \hat{\mathbf{j}}, \hat{\mathbf{k}}\}$ denote unit vectors in the rotating frame, with $\hat{\mathbf{k}}$ along the static field and $\hat{\mathbf{i}}$ along the instantaneous transverse rf field. These may be expressed in terms of laboratory-fixed unit vectors $\{\hat{\mathbf{x}}, \hat{\mathbf{y}}, \hat{\mathbf{z}}\}$ as

$$\begin{pmatrix} \hat{\mathbf{i}} \\ \hat{\mathbf{j}} \\ \hat{\mathbf{k}} \end{pmatrix} = \begin{pmatrix} \hat{\mathbf{x}}\cos\phi(t) - \hat{\mathbf{y}}\sin\phi(t) \\ \hat{\mathbf{y}}\cos\phi(t) + \hat{\mathbf{x}}\sin\phi(t) \\ \hat{\mathbf{z}} \end{pmatrix}. \tag{3.3}$$

The magnetization $M(t)$ evolves according to the torque equation $\dot{\mathbf{M}} = \gamma\mathbf{M}\times\mathbf{B}(t)$, which reads

$$\dot{\mathbf{M}} = \gamma\mathbf{M}\times\left(B_1\hat{\mathbf{i}} + \frac{\omega(t)-\omega_0}{\gamma}\hat{\mathbf{k}}\right) \tag{3.4}$$

in the rotating frame, with γ denoting the magnetogyric ratio of the spins. The equation of motion takes the form of Equation (3.4) even when the offset

$\Delta = \omega - \omega_0$ from the Larmor frequency $\omega_0 = \gamma B_0$ is time-varying[9]. The effective field in the rotating frame,

$$\mathbf{B}_{\text{eff}} \equiv \left(B_1 \hat{\mathbf{i}} + \frac{\omega(t) - \omega_0}{\gamma} \hat{\mathbf{k}} \right) = \left(B_1 \hat{\mathbf{i}} + \frac{\Delta(t)}{\gamma} \hat{\mathbf{k}} \right), \tag{3.5}$$

is a vector that traverses a path in the *i-k* plane as the instantaneous frequency of the applied field is changed. This path is a line parallel to $\hat{\mathbf{k}}$ if the magnitude of the transverse field is held fixed, as shown in Figure 3.15. If the angle $\theta(t)$ that the effective field makes with the transverse plane changes slowly compared to the precession rate:

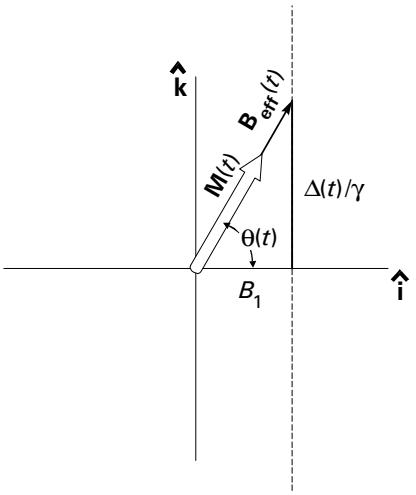

Figure 3.15. Efficient ARP. In the rotating frame, the offset frequency $\Delta(t)$ is swept so that the angle $\theta(t) = \tan^{-1}(\Delta(t)/\gamma B_1)$ changes linearly in time.

$$\left| d\theta/dt \right| << \sqrt{\gamma^2 B_1^2 + \Delta^2}\,, \tag{3.6}$$

then the approximate solution to Equation (3.4) is a magnetization vector $\mathbf{M}(t)$ that *follows* the effective field vector $\mathbf{B}_{\text{eff}}(t)$. This is the basis of the so-called adiabatic rapid passage (ARP): the transverse field is applied at a frequency which begins far off resonance and is swept through the resonance frequency to a point far on the other side, inverting the magnetization.

Simple trigonometric considerations evident in Figure 3.15 make the rate of change in θ for a given change in Δ maximum when $\Delta = 0$. This is also the condition

under which the adiabaticity condition (3.6) is most stringent. Therefore, both linear ($\Delta(t) \propto t$) and sinusoidal ($\Delta(t) \propto \sin \omega_m t$) sweeps in frequency place unnecessarily demanding constraints on the rate at which the magnetization can be efficiently swept through resonance, since in both these sweeps $|d\theta/dt|$ is largest just when $\mathbf{B}_{eff}$ is weakest.

This was recognized by Hardy *et al.*[10,11], who pointed out that since the precession rate is very large when the offset frequency Δ is large, the sweep rate in ARP can be much faster at the beginning and end of the sweep, that is, when the rf is far from resonance. They demonstrated a far more efficient, tangent-based adiabatic rapid passage using a frequency sweep of the form

$$\omega(t) = \omega_0 - \omega_s \tan(\omega_s \alpha t), \tag{3.7}$$

where ω_s is a sweep shape parameter near $\omega_1 = \gamma B_1$ and where

$$\alpha = \left(\frac{2}{\omega_s T_0}\right) \tan^{-1}\left(\frac{\Omega}{\omega_s}\right). \tag{3.8}$$

T_0 is the total sweep time ($-T_0/2 \le t \le +T_0/2$), and 2Ω is the range of the angular frequency sweep. These pulses use far less rf power for given ranges of both offset frequency Δ and rf field inhomogeneity ΔB_1 for a given required inversion efficiency.

Such frequency-modulated pulses are created by direct digital synthesis straightforwardly. To do this, one calculates the phase $\phi(t)$ as a function of a discrete time variable and then stores values proportional to $\sin \phi(t)$, which are "clocked out" to the waveform generator when needed. The required phase is the time integral of the frequency in Equation (3.7):

$$\phi(t) = \int_{-T_0/2}^{t} \omega(t)\,\mathrm{d}t = \omega_0\left(t + T_0/2\right) + \frac{1}{\alpha}\ln\frac{\cos\omega_s\alpha t}{\cos\omega_s\alpha\, T_0/2}. \qquad (3.9)$$

The inversions could be done by sweeping back-and-forth through the NMR line. However, if there is any difference between back-and-forth sweeps in the non-NMR response of the oscillator to the rf power in the coil (such as heating, mechanical expansion of the coil, *etc.*), then the predominant Fourier component of the resulting force will be exactly at the oscillator frequency. This back-and-forth sweeping protocol can thus lead to spurious driving of the oscillator. We suppress these effects by sweeping from the same side of the NMR line on every inversion as shown in Figure 3.16. This ensures that such non-NMR forces are at multiples of *twice* the oscillator frequency instead of exactly on mechanical resonance.

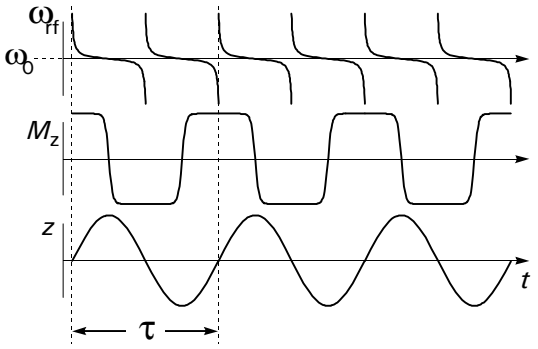

Figure 3.16. Driving the oscillator with efficient ARP. The frequency of applied rf is swept according to equation 3.7, and there are two sweeps per oscillator period τ. Both sweeps begin on the high-frequency side of the center frequency ω_0. The rate $d\omega_{rf}/dt$ is largest when the magnetization **M** is nearly along the static field direction. The oscillator amplitude $z(t)$ is 90° out of phase with the driving force, which is proportional to M_z.

A possible complication with such same-side sweeping is that for finite sweep width, an individual inversion ends with the effective field (and therefore the magnetization) having a non-vanishing transverse component. In order to prevent loss of this magnetization between passes, a 180-degree phase shift is applied on every other sweep. Figure 3.17 details how this phase shift corrects for such

imperfect inversion and retains more of the magnetization. We have found empirically that such phase cycling can prolong the driving interval by as much as a factor of four[2].

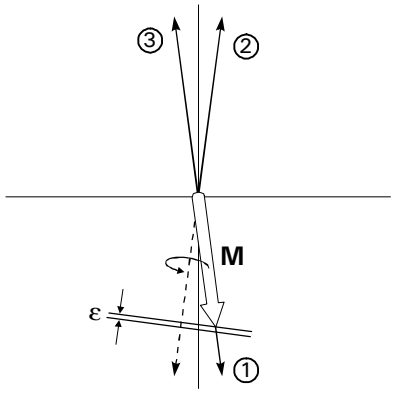

Figure 3.17. Phase cycling for efficient ARP. After one pass through resonance, the magnetization **M** is nearly, but not exactly, inverted (1). If the effective field at the start of the next pass through resonance is applied at (2) in this rotating-frame picture, then **M** is not perfectly aligned with the effective field. A component of **M** transverse to the effective field will be dephased. The net effect on **M** is a fractional loss of $\varepsilon = 1-\cos 2\theta \approx 2\theta^2$. A 180-degree phase shift of the rf, which places the effective field at (3), mitigates this loss.

Figure 3.18 shows the result of inverting proton magnetization in a 2.6 mm diameter liquid water sample over a 1-second interval with the phase-cycled tangent sweeps. By integrating the harmonic-oscillator equation of motion with an exponentially damped sinusoidal driving force, we can find the expected trajectory of the oscillator. When the oscillator's damping time τ is significantly shorter than the relaxation time T_{1a} of the magnetization, the result is

$$z(t) = Ae^{-t/T_{1a}}\left(1-e^{-t/\tau}\right)\cos\omega t\,, \tag{3.10}$$

where ω is the oscillator's resonance frequency, which is also the driving frequency (504 Hz for the transient in Figure 3.18). The amplitude A, which can be found using the theory of Chapter 2, is equal to the on-resonance steady-state amplitude were the magnetization not to decay.

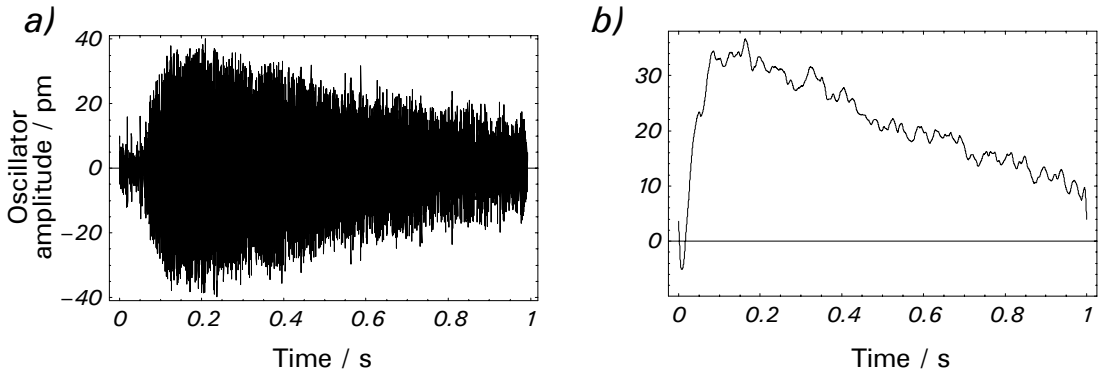

Figure 3.18. Driving the oscillator. a) Time series recorded during cyclic inversion of proton magnetization in a 2.6-mm diameter liquid water sample. b) Envelope of the signal in figure (a). Data from (a) were digitally mixed down to DC and then filtered in order to fit the data. The transient excitation was fit to equation (3.10) in order to find T_{1a}(0.687 s), τ (51 ms), and the amplitude (44.7 pm). The measured amplitude agrees with predictions from the theory in Chapter 2 (45.1 pm) to within about 1%.

Figure 3.18 b shows the amplitude envelope of the transient in Figure 3.18 a. A fit to Equation (3.10) yields $\tau = 51$ ms, $T_{1a} = 0.687$ s, and $A = 44.7$ pm. Agreement of the amplitude with expectations (45.1 pm) using an estimate of the sensor's magnetization from the observed Larmor frequency and the signal theory of Chapter 2 is remarkable ($< 1\%$). The measured T_{1a} corresponds to about 693 inversions by the time the magnetization decays by the factor *e*. This relaxation time is substantially shorter than the T_1 of water[2] (4.3 s) as measured by inversion-recovery (see Chapter 4). These results indicate that the whole sample magnetization is being used to drive the oscillator, but that substantial relaxation of the magnetization is taking place as a result of the inversions.

3.7 System Noise Analysis

3.7.0 Brownian motion revisited. Displacement calibration

Even at the prototype size scale, the principal source of noise in the recorded transients is due to the Brownian motion of the oscillator. This can be quantified in two ways – as noise in the driving force or noise in a displacement measurement. On general thermodynamic grounds[7,12], the rms fluctuation in the average force on the oscillator is predicted to be

$$F_{z,\mathrm{rms}} = \sqrt{4k_B T\alpha\Delta f}\ . \tag{3.10}$$

This may be viewed as the square root of a force-noise spectral density

$$S_F^{1/2} = \sqrt{4k_B T\alpha} \tag{3.11}$$

multiplied by the square root of a bandwidth, Δf. If the bandwidth of the measurement is substantially less than the bandwidth $\gamma/2\pi = 1/4\tau$ of the mechanical oscillator (which is true for the pointwise detection schemes of Chapter 4 when $T_{1a} >> \tau$), then the oscillator is approximately in steady state during the time the oscillator is driven. In this case the square root of the corresponding displacement-noise spectral density at mechanical resonance is obtained from (3.11) by multiplying $S_F^{1/2}$ by the quality factor $Q = \omega/\gamma$ and dividing by the spring constant $m\omega^2$:

$$S_x^{1/2} = \frac{Q}{m\omega^2}\sqrt{4k_B T\alpha} = \frac{1}{m\omega\gamma}\sqrt{4k_B T\alpha} = \sqrt{4k_B T/m\omega^2\gamma}\ . \tag{3.12}$$

With $m = 139\,\mathrm{mg}$, $\omega/2\pi = 496\,\mathrm{Hz}$, and $\gamma/2\pi = 5.0\,\mathrm{Hz}$, $S_F^{1/2}$ and $S_x^{1/2}$ are $8.4\ \mathrm{pN}/\sqrt{\mathrm{Hz}}$ and $620\ \mathrm{fm}/\sqrt{\mathrm{Hz}}$ ($6.2\ \mathrm{m\AA}/\sqrt{\mathrm{Hz}}$), respectively, at room temperature (293 K). As we shall see below, this contribution dominates other noise sources, but only by a small factor at the prototype size scale, and so some care was exercised in suppressing these other sources as much as possible. In smaller spectrometers, the Brownian-motion noise will be fractionally larger relative to these other sources of instrument noise. For direct comparison to Brownian-motion noise, each noise source is referred back to a displacement noise spectral density through multiplication by relevant gain factors, whose nominal values are shown in the signal path of Figure 3.19.

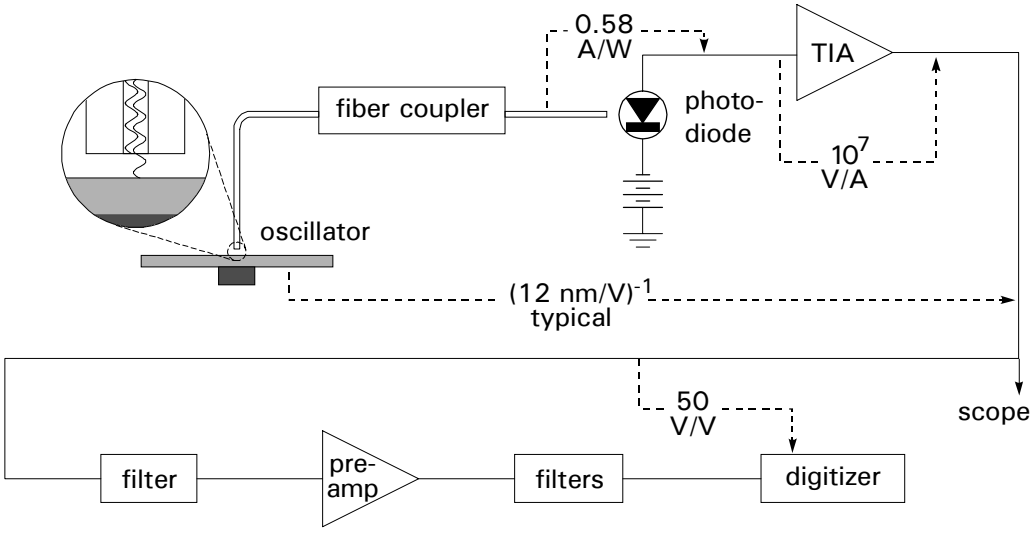

Figure 3.19. Signal conditioning path. Selected gain factors are shown for important connections in the signal path.

3.7.1 Photon shot noise

When the interferometer is set to its most linear operating point, there is a dc component to the light incident on the detector. The dc level of the light intensity at the photodetector is the source of two kinds of noise. The first is shot noise, which is due to the Poisson statistics of independent "photon arrivals," each with energy $h\nu$, from the light field[13]. If P denotes the optical power incident on the detector, then in a time interval Δt, $N = P\Delta t/h\nu$ photons arrive at the detector on average. The rms fluctuation in this average is $\sqrt{N}$, and therefore the rms fluctuation in the optical power is

$$P_{\text{rms}} = \frac{h\nu}{\Delta t}\sqrt{N} = \sqrt{Ph\nu/\Delta t} = \sqrt{2Ph\nu\Delta f}\,, \tag{3.13}$$

where explicit dependence on the the time interval Δt has been suppressed in favor of the corresponding bandwidth $\Delta f = 1/2\Delta t$. This allows convenient comparison of the square root of the corresponding noise spectral density,

$$S_{h\nu}^{1/2} = \sqrt{2Ph\nu}\,, \tag{3.14}$$

to other noise sources, including Brownian motion. With $P = 1.7\,\mu\text{W}$ and $\nu = c/780\,\text{nm}$, $S_{h\nu}^{1/2} = 930\,\text{fW}/\sqrt{\text{Hz}}$. We convert this value to the square root of the corresponding displacement-noise spectral density by multiplying (3.14) by the detector responsivity (0.58 A/W) to obtain the corresponding photocurrent noise, then by the transimpedance ($10^7\ \Omega$) to obtain the corresponding voltage noise out of the photocurrent amplifier, and finally by the displacement sensitivity (typically 12 nm/V). The result is $S_{x,h\nu}^{1/2} = 65\,\text{fm}/\sqrt{\text{Hz}}$.

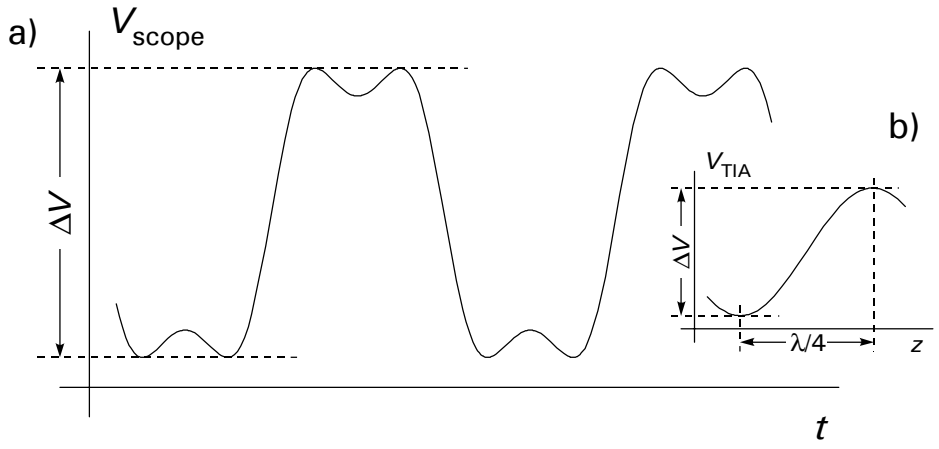

Figure 3.20. Interferometer displacement calibration. a) Voltage at the output of the transimpedance amplifier observed on an oscilloscope registers the voltage span associated with the interferometer's trough-to-crest displacement change. b) The laser intensity goes from trough to crest when the fiber-to-oscillator gap increases by $\lambda/4 = 195$ nm because the wave must traverse the gap twice before it re-enters the fiber and mixes with the reference wave. The displacement sensitivity may thus be calculated using equation (3.16).

The displacement sensitivity, the proportionality constant relating displacement to observed voltage at the output of the photocurrent amplifier, is used here because it is readily measured in the following way. The oscillator is driven to an amplitude that is large enough to observe the "folding over" of the voltage-to-distance relation (see Figure 3.20). These nanometer-scale oscillations are well within the expected range of linearity of the silicon oscillator, and so the nonlinearity of the observed voltage is due entirely to "interferometer action." The difference between the extrema of the oscilloscope trace corresponds to the voltage difference associated with a displacement of $\lambda/4$. Since the slope of the voltage-to-displacement sine curve is greater than the ratio of voltage span to displacement by $\pi/2$ in the linear region (as shown in Figure 3.20), the displacement sensitivity is

$$\frac{2}{\pi} \times \frac{\lambda/4}{V_{max} - V_{min}}. \tag{3.16}$$

3.7.2 Photon pressure fluctuations

The second type of noise due to the Poisson statistics of the laser radiation is the result of fluctuations in radiation pressure. These can be estimated with a simple model that assumes that a single photon impact on the oscillator transfers $2h\nu/c$ to the oscillator's momentum. Again, if in a time Δt there are $N = P\Delta t/h\nu$ photon impacts, then the rms fluctuation in the transferred momentum is

$$p_{\mathrm{rms}} = \frac{2h\nu}{c}\sqrt{N} = \sqrt{4\,Ph\nu\Delta t/c^2}\ . \tag{3.17}$$

If this momentum fluctuation takes place in a time Δt, then it may be viewed as a random force $p_{\mathrm{rms}}/\Delta t$, which has the force spectral density

$$S_{\mathrm{F},hk}^{1/2} = \sqrt{8Ph\nu/c^2} \tag{3.18}$$

and, in analogy with Equation (3.12), the displacement-noise spectral density

$$S_{\mathrm{x},hk}^{1/2} = \frac{1}{m\omega\gamma}\sqrt{8Ph\nu/c^2}\ . \tag{3.19}$$

At the BOOMERANG prototype size scale, this contribution (5.4×10^{-7} fm$/\sqrt{\mathrm{Hz}}$) is totally negligible. While it will become more important in force-detected NMR at reduced size scales[14], it is not a limiting factor in any proposed designs.

3.7.3 Photocurrent shot noise

Photocurrent shot noise is due to the Poisson statistics of discrete charge carriers in the electronic current through a diode. As this noise source is directly

correlated with the statistics of photon arrivals, we have already accounted for it in analyzing the photon shot noise.

3.7.4 Johnson noise in the transimpedance

The photocurrent amplifier uses a resistor at the input to convert the current to a voltage. The Johnson noise in this resistance forms the bulk of the noise added by this amplifier. The noise specification in the amplifier's documentation[15] is consistent with this fundamental physical argument, and the amplifier was found to behave according to specification. The square root of the voltage-noise spectral density due to Johnson noise in a resistance R is given by

$$S_{\Omega}^{1/2} = \sqrt{4k_{\mathrm{B}}TR}\,. \tag{3.20}$$

For a transimpedance of $10^7\ \Omega$, this is $S_{\Omega}^{1/2} = 400\,\mathrm{nV}/\sqrt{\mathrm{Hz}}$. This can be converted to the square root of a displacement-noise spectral density by multiplication by the displacement sensitivity. The result is $S_{\mathrm{x},\Omega}^{1/2} = 4.8\,\mathrm{fm}/\sqrt{\mathrm{Hz}}$.

3.7.5 Electronic noise in the preamp

The Stanford Research preamp documentation[16] specifies the voltage noise of the preamp referred to the input as

$$S_{\mathrm{E}}^{1/2} = 1.5\,\mathrm{nV}/\sqrt{\mathrm{Hz}}\,. \tag{3.21}$$

Multiplying by the displacement sensitivity, we find $S_{\mathrm{x,E}}^{1/2} = 0.018\,\mathrm{fm}/\sqrt{\mathrm{Hz}}$, which is negligible compared to Brownian motion.

3.7.6 Digitization noise

When the analog signal is digitized, the discretization of the signal introduces noise into each sample of the recorded data. This is shown in Figure 3.21. The added noise in a given voltage sample will be distributed uniformly over the range $+\varepsilon/2$ to $-\varepsilon/2$, where ε is the step size of the digitization process. This corresponds to an rms average fluctuation of $\varepsilon/\sqrt{12}$ in the bandwidth $\Delta f = 1/2\Delta t$, where Δt is the sampling time. The relevant voltage-noise spectral density (at the digitizer) is

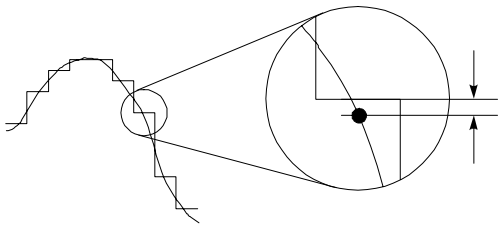

Figure 3.21. Digitization noise. In a given time slice, the requirement that the output of the digitizer be only one of a set of fixed values adds uncertainty to the measured value. This uncertainty is centered at zero and uniformly distributed over a range equal to the step size of the digitization process.

$$S_D^{1/2} = \frac{\varepsilon}{\sqrt{12}}\sqrt{2\Delta t} = \varepsilon\sqrt{\Delta t/6}\,. \tag{3.22}$$

For the prototype, a 16-bit digitizer was used, with full range -1.25V to $+1.25$V, corresponding to $\varepsilon = 38.1\mu$V. For samples acquired every 500μs, $S_D^{1/2} = 348\,\text{nV}/\sqrt{\text{Hz}}$ at the digitizer. To convert this to a corresponding displacement noise spectral density, this must be divided by the gain of the preamp (typically 50) and multiplied by the displacement sensitivity, yielding $S_{x,D}^{1/2} = 0.084\,\text{fm}/\sqrt{\text{Hz}}$. This estimate is for an otherwise noiseless digitizer. In the prototype experiments, it was observed that even with the inputs of the digitizer grounded, a frequency-independent electrical noise corresponding to ~ 3 bits peak-to-peak (rms amplitude

$2^3\varepsilon/2\sqrt{2}$) is recorded in the data, probably caused by electrical noise inside the computer. Even with this factor, the digitizer added negligible noise compared to Brownian motion.

References

1 G. W. Castellan, *Physical Chemistry*, 3rd ed. (Addison-Wesley, Reading, MA, 1983).

2 L. A. Madsen, Ph. D. Thesis, California Institute of Technology, 2002.

3 Magnetic Alloys Catalog (Carpenter Technology Corp., 1995).

4 G. M. Leskowitz, L. A. Madsen, and D. P. Weitekamp, *Sol. St. Nucl. Magn. Reson.* **11,** 73 (1998).

5 W. D. Pilkey, *Formulas for Stress, Strain, and Structural Matrices* (John Wiley & Sons, Inc., New York, 1994).

6 D. Rugar, H. J. Mamin, and P. Guethner, *Appl. Phys. Lett.* **55,** 2588 (1989).

7 C. W. McCombie, *Rep. Prog. Phys.* **16,** 266 (1953).

8 T. George, et al., in *IEEE Aerospace Conference* (Big Sky, Montana, 2001).

9 C. P. Slichter, *Principles of Magnetic Resonance*, 3rd ed. (Springer-Verlag, Berlin, 1990).

10 C. J. Hardy, W. A. Edelstein, and D. Vatis, *J. Magn. Reson.* **66,** 470 (1986).

11 C. J. Hardy and W. A. Edelstein, *J. Magn. Reson.* **69,** 196 (1986).

12 S. Chandrasekhar, *Rev. Mod. Phys.* **15,** 1 (1943).

13 C. W. Gardiner, *Handbook of Stochastic Methods for Physics, Chemistry, and the Natural Sciences*, 2nd ed. (Springer, Berlin, 1985).

14 J. A. Sidles, J. L. Garbini, K. J. Bruland, D. Rugar, O. Züger, S. Hoen, and C. S. Yannoni, *Rev. Mod. Phys.* **67,** 249 (1995).

15 Model 181 Current Sensitive Preamplifier manual (Princeton Applied Research Corp., 1978).

16 Model SR530 Lock-In Amplifier manual (Stanford Research Systems, 1989).

Chapter 4: Spectroscopy

4.0 CW Spectroscopy

The BOOMERANG apparatus described in the last chapter measures a mechanical transient proportional to the sample's longitudinal magnetization. The oscillator-driving protocol used during this detection period relies on a nonlinear sweep in the frequency of an applied rf field. As we saw in Figure 3.16, the sweep has a center-band region during which the frequency change is slow. If this center-band region is near the Larmor frequency of spins in the sample, then the spins are inverted, and forces on the oscillator drive it into resonance. If the slow part of the sweep is far off the spin resonance then the driving field either never sweeps through resonance or it sweeps so quickly as to violate the adiabatic condition (Equation 3.6). In this case the applied field is ineffective in inverting the spins, and so no oscillator driving is observed. This suggests a simple procedure for measuring the NMR spectrum: cyclic adiabatic passage is applied to the spins, and the amplitude of the oscillator's trajectory is measured as a function of the frequency of the center-band, which is stepped on successive iterations of the experiment.

Figure 4.1 shows a graph of oscillator amplitude integrated over the detection time versus the center-band frequency of the applied field. These amplitudes clearly map out the frequency spectrum of the spin resonance. This

method can be viewed as a pointwise version of continuous-wave (CW) NMR spectroscopy. The spectrum shown in Figure 4.1 is that of protons in liquid water at 0.638 T.

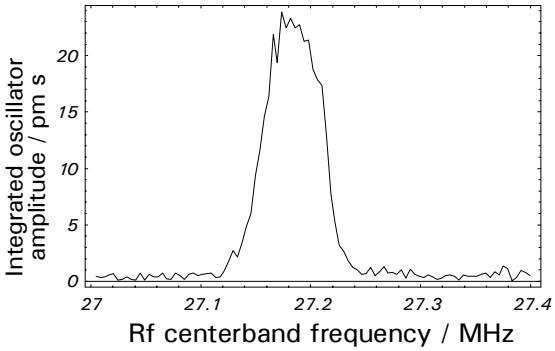

Figure 4.1. ^{1}H CW-NMR spectrum of liquid water.

The FWHM line width in this particular spectrum is 70 kHz, which is greater than the inhomogeneous linewidth of the liquid sample. This broadening is observed when the rf is strong enough to cyclically invert the spins even when the slow part of the sweep is somewhat off resonance. Because of this broadening effect, the cw spectrum is used only as a coarse measurement of the Larmor frequency.

4.1 Inversion-Recovery

Once the Larmor frequency is known, we can reproducibly measure the longitudinal magnetization of the sample by recording a transient and then fitting to find a signed amplitude. If the driving period follows a period during which this magnetization is modulated in some way, then one can measure relevant characteristics of the spin system. The simplest measurement that can be made in this way is of the longitudinal relaxation time, T_1. This is done using an inversion-recovery method.

Figure 4.2 shows a graph of integrated amplitude *vs.* the length of a time interval that follows a single adiabatic inversion and precedes detection. This interval t_1 is varied between iterations of the experiment, and on a given iteration the magnetization relaxes back toward equilibrium during t_1. The magnetization that survives this relaxation varies according to an exponential function. A fit to the graph yields the longitudinal relaxation time $T_1 = 1.67$ s for this sample, which is 1,1,1,3,3,3-hexafluoro-2-propanol ($(CF_3)_2CHOH$) at room temperature.

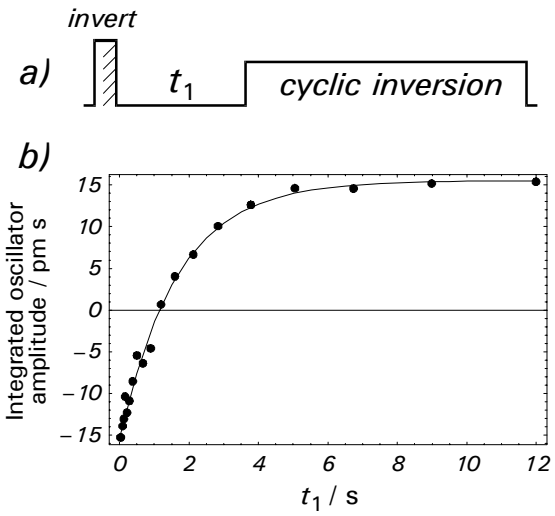

Figure 4.2. Measurement of ^{19}F T_1 by inversion-recovery. a) Pulse sequence. A single adiabatic inversion pulse is followed by an interval of variable length t_1. Then the oscillator's trajectory is measured during cyclic inversion. b) Integrated amplitude of the trajectory as a function of t_1. The sample is hexafluoroisopropanol. A fit to the exponential yields $T_1 = 1.67 \pm 0.1$ s.

4.2 Time Sequencing – FT-NMR with Half-Passages

This separation of a detection period from a time t_1 during which information about the spin system is encoded for measurement during detection is a general method with wide applicability. The detected observable, M_z, is often (except in susceptometry[1] and in inversion-recovery) not the one of interest. However, if one can apply pulses with well-defined flip angles to the sample, then it is a simple matter to use the detection of M_z to measure transverse magnetization. This is done

in pointwise fashion with time sequencing, which is also useful in optically[2] and inductively[3] detected NMR.

Figure 4.3 shows the most general scheme for encoding information about the magnetization into the oscillator's trajectory. The principle is to use the evolution period as a way to systematically create nonequilibrium longitudinal magnetization for measurement during detection. We have already seen one example of the longitudinal case (Figure 4.3 b), where the nonequilibrium magnetization is the result of incomplete longitudinal relaxation. If the detection period follows a single "store pulse" (with flip angle $\pi/2$), then the detection period instead measures a single component of *transverse* magnetization.

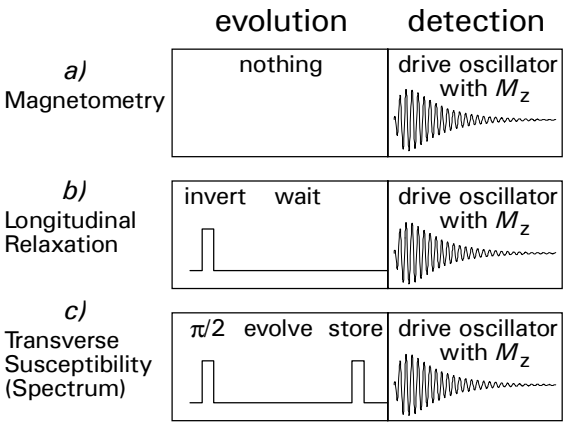

Figure 4.3. Time sequencing for pointwise acquisition of information from spin systems. The detection period is preceded by an evolution period during which information about the sample is encoded into non-equilibrium magnetization. Aspects of the evolution period are varied between iterations of the experiment.

This is illustrated by a simple pulse sequence that can be used to measure FT-NMR, which is shown in Figure 4.3 c. The initial $\pi/2$ pulse creates transverse magnetization from equilibrium magnetization. This transverse magnetization precesses in the static field for a measured time t_1. During this period, the spins evolve under the influence of the total spin Hamiltonian, whose dominant term is due to the static field, but which also includes chemical shift, field inhomogeneity,

and spin-spin couplings. After t_1 has elapsed, a second $\pi/2$ pulse is applied. This pulse selects one component of the transverse magnetization that survives the evolution interval for measurement during the detection period. The integrated amplitude of the detected transient is recorded as a function of t_1, and the length of this interval is varied on successive iterations of the experiment. The resulting time-domain signal is subject to Fourier transformation, yielding the spectrum.

This protocol relies on pulses with well-defined flip angles. Such flip angles can be measured with a nutation pulse sequence as described in section 4.3. This nutation sequence in turn requires that an accurate Larmor frequency has already been established, so that the frequency offset used is small compared to the Rabi frequency.

A simple way to circumvent this difficulty is to perform FT-NMR with the pulse sequence of Figure 4.3 b, but with the $\pi/2$ pulses replaced by adiabatic half-passages. If an adiabatic sweep is terminated in the center of the NMR line (when $\Delta = 0$, see Figure 3.15) the sample's magnetization is left in the transverse plane with a well-defined phase. The rf is turned off and then, after t_1 has elapsed, it is turned back on again with the same frequency and phase. If the adiabatic sweep is resumed to completion, then this procedure selects one component of the transverse magnetization that survives evolution during t_1 for subsequent detection. The size of the signal is relatively insensitive to the exact Larmor frequency (a previous measurement with CW spectroscopy suffices), and one requires only a very rough estimate of the Rabi frequency for use in selecting tangent sweep parameters.

Figure 4.4 shows an FT-NMR spectrum of liquid water obtained in this way. The observed spectrum is not subject to power-broadening as it is in CW spectroscopy, and so the NMR line is substantially narrower. The resulting better estimate of the Larmor frequency can be used in nutation and subsequently in multiple-pulse experiments. The line width is dominated by residual inhomogeneity in the static field. It is to be emphasized that this left-over inhomogeneity (which is about three orders of magnitude less than it would be were the annular magnets removed) is well within the range of compensation by mechanical or electrical shimming apparatus, which have not been included in the prototype.

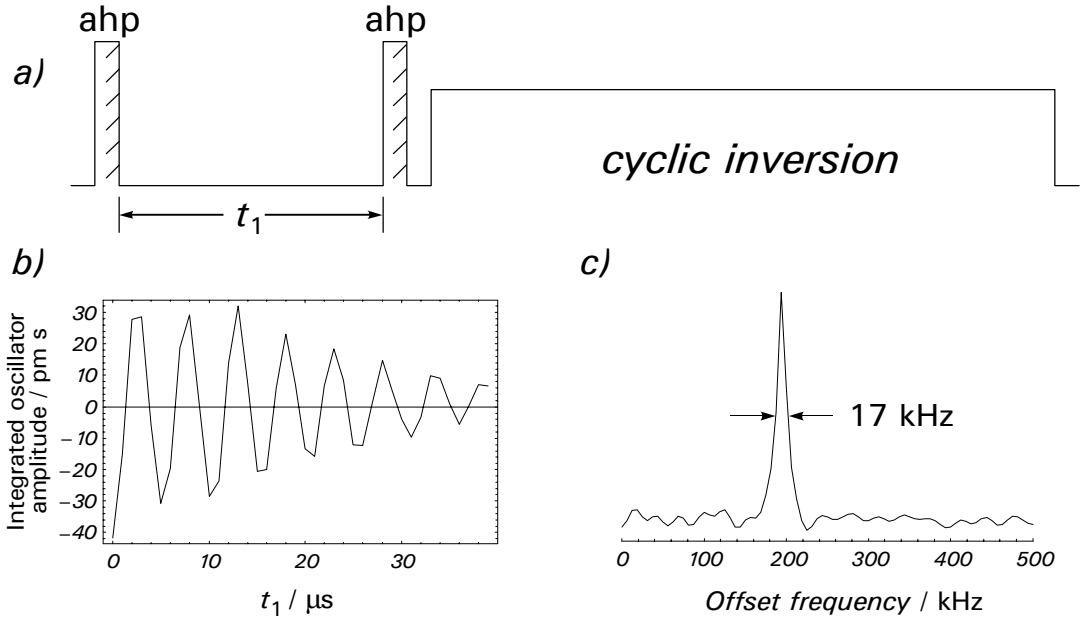

Figure 4.4. FT-NMR with adiabatic half-passages. a) Pulse sequence. An adiabatic half-passage creates transverse magnetization, which evolves during t_1. A store pulse selects one component of this magnetization, which is used to drive the oscillator during cyclic inversion. b) Integrated amplitude of the oscillator's trajectory as a function of t_1. This time-domain signal can be Fourier-transformed to yield a spectrum. c) The NMR spectrum. Data in (b) were fit to an exponentially decaying cosine, and this fitting function was used to extend the time-domain data (by a factor of four) in lieu of apodization in order to suppress noise and artifacts of the Fourier transform.

This method of encoding evolution of transverse magnetization (the single-quantum spectrum) into pointwise evolution of M_z bears resemblance to how multiple-quantum coherences are encoded pointwise into observable transverse magnetization in two-dimensional NMR spectroscopies[4]. In principle, *any* NMR pulse sequence can be inserted into the evolution interval in BOOMERANG. The separation of encoding and detection into distinct time intervals in BOOMERANG allows the whole spectrum to be obtained even though the spectral bandwidth is orders of magnitude larger than the oscillator bandwidth.

4.3 Nutation – t_1 and t_2 Noise

Figure 4.5 a shows a pulse sequence that can be used to measure the Rabi frequency of spins in the applied rf field (by nutation of the magnetization). The Rabi frequency is obtained by fitting the data in Figure 4.5 b to a decaying exponential or by Fourier transformation. The signal-to-noise in this experiment is sufficient to obtain a Rabi frequency to within about 5% (standard error). Figure 4.5 c shows residuals from the fit. The rms deviation in each time-domain point is about 6.9 pm, which is substantially larger than the ~0.5 pm rms error one would predict from the observed statistics of the t_2 transients given the ~0.5-Hz bandwidth of the measurement. The t_1 noise is therefore about 15 times larger than the t_2 noise. A similar analysis can be performed on data from the CW-NMR experiment shown in Figure 4.1. In that case, phases are not used at all in the fits, and the measured rms t_1 noise in each point's absolute value is about 0.3 pm. This shows that instabilities in the phase of the signal are at present our main noise source. Part of this phase instability comes from changes in the oscillator frequency during the driving interval,

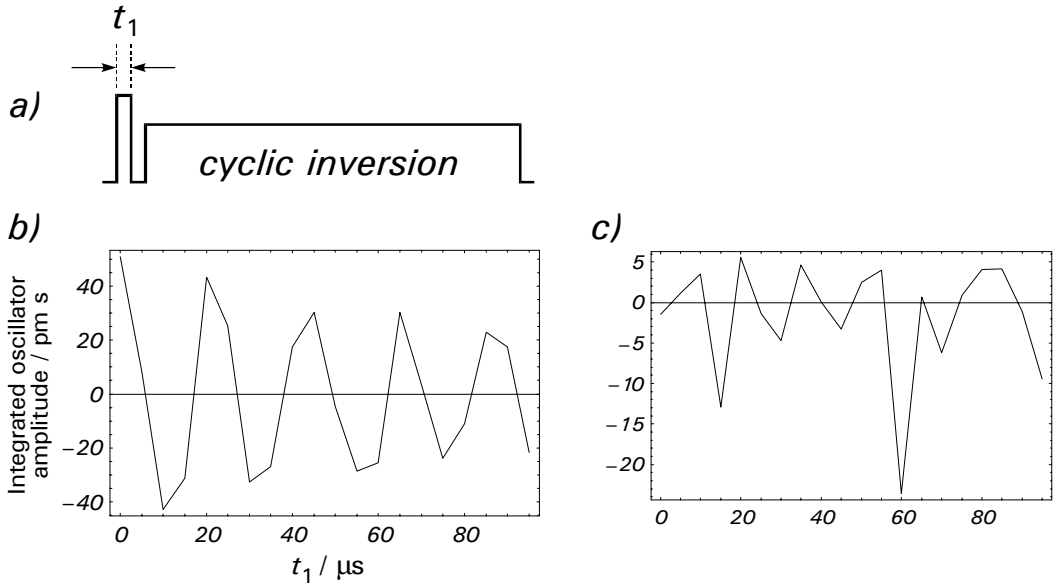

Figure 4.5. Nutation of proton magnetization in water. a) Pulse sequence. A single rf pulse of varied length t_1 is applied, followed by cyclic inversion and detection of the oscillator's trajectory. b) Integrated amplitude of the oscillator's trajectory as a function of t_1. A fit to an exponentially decaying cosine shows that the Rabi frequency is 46.7 ± 0.2 kHz. c) Residuals from the fit. The noise is about 20 times larger than what one would calculate from the noise in the transients. The t_1 noise is probably from instabilities in phase shot-to-shot in the experiment.

as we observed in Chapter 3. But it was also observed that the software triggering of the data acquisition in the prototype was subject to considerable jitter. Indeed, removal of the single point in the nutation time-domain data at $t_1 = 60\,\mu s$ reduces the rms errors by almost a factor of two. A look at the phase reference channel for this point shows substantial shift relative to other points.

4.4 Spin Echo

After relatively precise Larmor and Rabi frequencies are obtained from FT-NMR and nutation, in principle any multiple-pulse NMR experiment is compatible

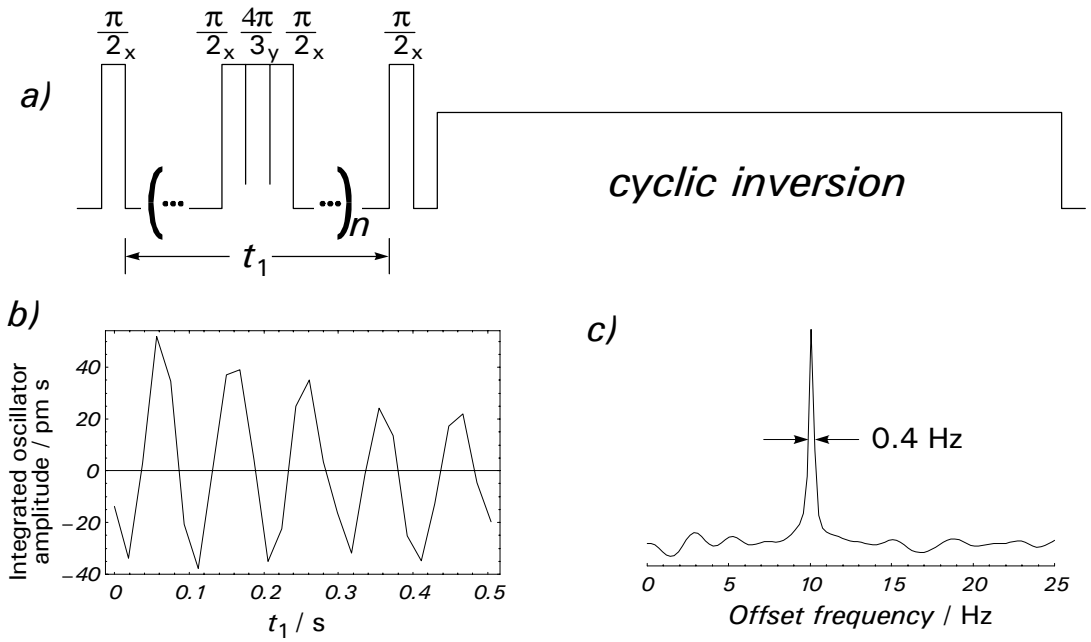

Figure 4.6. ^{19}F spin echo in hexafluoroisopropanol. a) Pulse sequence. A train of compensated π pulses is applied between a preparatory π/2 pulse and a "store pulse." b) Integrated amplitude of the oscillator's trajectory as a function of t_1. A fit to an exponentially decaying cosine is used, and the decay time is 0.96 ± 0.3 s. This fitting function is used to extend the time-domain data (by a factor of eight) in lieu of apodization in order to suppress artifacts of the Fourier transform. The resulting Fourier spectrum (c) exhibits a FWHM linewidth of 0.4 Hz.

with BOOMERANG. Figure 4.6 shows an example, a spin-echo sequence applied to ^{19}F in hexafluoroisopropanol using a train of composite π pulses. The decay time of the echo transient (0.96 s) is comparable to but somewhat smaller than the T_1 observed in the same compound by inversion-recovery (1.67 s). Given that the intrinsic rotating-frame relaxation time ($T_{1\rho}$) of the sample is likely near T_1 for such a small molecule, there are at least three factors that might contribute to this increased decay time. Some dephasing is probably taking place due to imperfections in the pulses. Such dephasing was not refocused because limitations in the pulse-programming hardware prevented phase-cycling the echo sequence. Another

possibility is dephasing due to diffusion in the residual gradient. Finally, the apparent signal strength itself may also be decreasing due to changes in the oscillator or in the Larmor frequency due to a slight drift in the sensor's magnetization.

4.5 Heteronuclear J Spectroscopy

Figure 4.7 shows an experiment with pulses on 2 nuclei (^{1}H and ^{19}F) in fluoroacetonitrile (FCH_2CN). The composite π pulses that were used in the echo experiment of Figure 4.6 were applied to both ^{1}H and ^{19}F after a preparatory $\pi/2$ pulse on ^{1}H. The time delay is incremented iteration to iteration in the experiment as always. When composite π pulses are applied to both spins, chemical shift and field inhomogeneity terms in the Hamiltonian are refocused, but the heteronuclear scalar coupling is not. The scalar coupling is observed in the spectrum as a splitting.

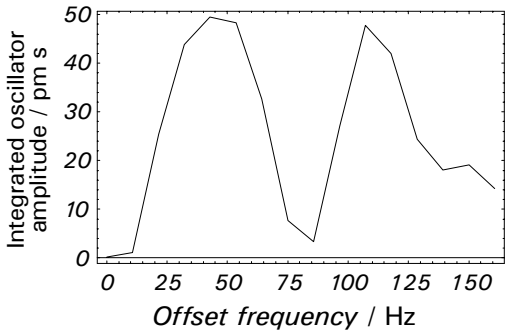

Figure 4.7. Heteronuclear J spectrum of fluoroacetonitrile. A train of compensated π pulses was applied to both ^{19}F and ^{1}H between a preparatory $\pi/2$ pulse and a store pulse on ^{1}H.

References

1 L. A. Madsen, Ph. D. Thesis, California Institute of Technology, 2002.

2 S. K. Buratto, D. N. Shykind, and D. P. Weitekamp, *Phys. Rev. B* **44,** 9035 (1991).

3 D. P. Weitekamp, *Adv. Magn. Reson.* **11,** 111 (1983).

4 R. R. Ernst, G. Bodenhausen, and A. Wokaun, *Principles of Nuclear Magnetic Resonance in One and Two Dimensions* (Clarendon Press, Oxford, 1987).

Chapter 5: BOOMERANG at the Micron Scale and Below

5.0 Introduction

The availability of a general NMR method whose sensitivity persists down to size scales that are fundamentally inaccessible to inductive detection motivates speculation regarding applications. The observation of NMR from nanoliter samples with inductive detection in microcoils with moderately concentrated samples[1,2] is near the lower size limit where inductive detection is predicted to be competitive with BOOMERANG for proton-bearing samples at conveniently available static field strengths. As we noted in Chapter 2, this crossover limit is at larger size scales for almost all other nuclei and for the lower (~2 T) field strengths that are practical with static fields generated by ferromagnets. Thus, BOOMERANG is being developed[3,4] as the NMR method of choice for low-power, low-cost, portable devices for NMR in remote environments such as in space exploration. Portable NMR here on Earth is also of interest for convenience or for high-throughput tasks, and so inexpensive 2 T spectrometer units for laboratory glove boxes or dip-probes for use in industrial process streams are candidate applications for commercialization of BOOMERANG technology.

Just as interesting is NMR at the higher fields available in commercial superconducting magnets. There are many samples in the ~0.1-100 μm size range that, according to estimates in Chapter 2, would exhibit satisfactory signal-to-noise with acceptable signal averaging. The main motivation here is in cases where sample size is limited intrinsically, such as in forensics, or when it is desirable to examine systems one at a time rather than in ensemble average. For example, BOOMERANG might allow spectroscopy and imaging of individual cells or membranes *in situ* or rotation studies on individual protein or zeolite crystallites that may be too small for use in crystallography. Another area of application at somewhat smaller scales is quantum dots.

The ability to measure NMR on a sample containing 10^9 –10^{12} spins would also enable NMR spectra of molecular monolayers and other surface species. There are special geometric considerations to be taken into account in surface studies and some of these are treated in section 5.3. An ultimate goal in designs for BOOMERANG at the micron scale is a microfabricated array of BOOMERANG spectrometers, which would allow massively parallel NMR analysis of sample libraries used in combinatorial-chemistry approaches to all kinds of problems in materials science, catalysis, and biochemistry.

Clearly there is sufficient motivation for NMR devices at length scales where the sensitivity of BOOMERANG is adequate but that of inductive methods is not. We have predicted on grounds of sensitivity and resolution that BOOMERANG methods show great promise as the means of extending NMR into the realm of smaller samples in a general way. However, in our analysis of sensitivity in both

force and induction methods, we have considered only instrument noise due to thermal processes in the detector. We now consider a new noise source that comes from the sample itself: spin noise.

Spin noise is uncertainty in the measured values of spectral parameters due to fluctuations in the sample's initial magnetization. It is present, independent of detection method, whenever measurements must be repeated on a standard initial state, such as in signal averaging or in the time-sequencing methods described in Chapter 4. In the context of proposals for very high sensitivity MRFM of biomolecules[5], (where, for more than one target spin, it may turn out to be a show-stopper), it has been largely ignored.

5.1 Spin Noise

The problem is best illustrated by example. Suppose we have a 0.8 ml room-temperature liquid sample 0.002 M in an organic compound and we wish to measure its single-quantum ^{13}C NMR spectrum at 125 MHz. If we have a single carbon site of interest per molecule, this sample contains 10^{18} of the target spins. The sample's magnetization can be calculated with the Curie law, which may be written

$$M = \frac{\overline{N}\hbar\gamma}{2}\frac{\hbar\gamma B}{2k_B T} \tag{5.1}$$

at high temperature T for spin-½ nuclei with magnetogyric ratio γ at spin density $\overline{N}$ in a static field B. This formula contains the polarization,

$$p = \tanh\left(\frac{\hbar\gamma B}{2k_B T}\right) \approx \frac{\hbar\gamma B}{2k_B T}, \tag{5.2}$$

which is 10^{-5} for the present case. Since the sample contains 10^{18} spins, and the equilibrium polarization is 10^{-5}, the net magnetization available to drive the detection apparatus is that of only 10^{13} spins.

The total magnetization is the sum of the magnetic moments of N spins per unit volume, each of which has a roughly but not exactly equal probability of contributing $+1$ or -1 nuclear moments to the magnetization when the polarization is much less than unity (we shall make this more precise later, but for now, the error statistics are nearly those of flipping a very slightly weighted coin). The uncertainty in the initial magnetization is proportional to $\sqrt{N}$. For the 10^{18} spin sample, this fluctuation magnetization, which manifests as shot-to-shot variations in the initial magnetization, is that of 10^9 spins, only 0.01% of the signal. The distribution of values of initial magnetization is shown schematically in Figure 5.1 a.

The situation is entirely different for the case of 10^5 spins (*e.g.*, a moderately concentrated species coating a single 1 μm diameter cell). Here, the average signal magnetization at room temperature in a 125 MHz field corresponds to that of only one spin on average, while the shot-to-shot fluctuations in magnetization are proportional to $\sqrt{N} \approx 300$ spins. The distribution for this case is shown in Figure 5.1 b. In a time-sequenced experiment, these fluctuations in initial magnetization manifest as so-called t_1 noise, which in this case is 300 times larger than the signal per root shot, even in the case of no instrument noise.

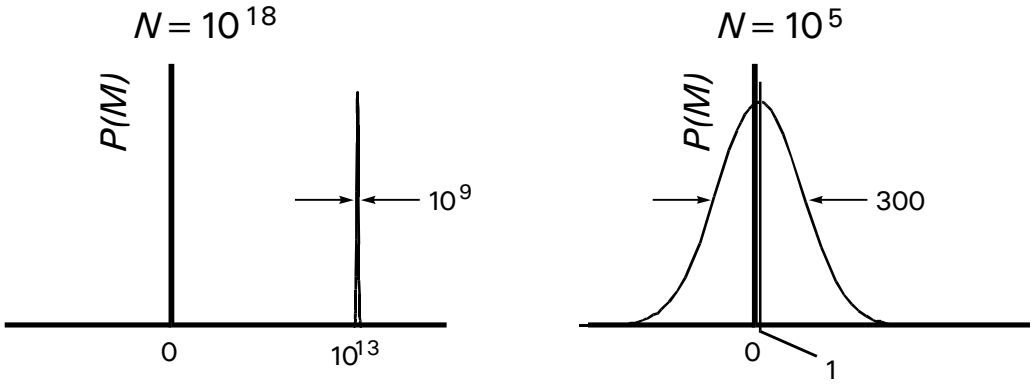

Figure 5.1. (a) Probability distribution for the net magnetization of $N = 10^{18}$ spins at thermal equilibrium with polarization 10^{-5}. The distribution is very sharply peaked, as the polarization p is significantly larger than $N^{-1/2}$. (b) Probability distribution for the net magnetization of $N = 10^5$ spins. Here the variance of the (roughly binomial) distribution is substantially larger than the mean. Note also that values of opposite sign from the mean are about as probable as values having the same sign.

The solution to the problem is in recognizing that in general we are interested in parameters in a spin Hamiltonian and not particularly in the magnetization *per se*. In fact, a look at the vast majority of published NMR spectra shows no units on the "y-axis" (or other ordinate axis if we are looking at multidimensional spectra). What we care about is a *correlation function* or its spectrum: the Bohr frequencies, relaxation times, coupling constants, and *relative* amplitudes in spectroscopy, or some kind of contrast observable in imaging.

5.2 Correlated Observations Narrow Quantum Uncertainty, Enhancing Spectroscopic Transients (CONQUEST)

Figure 5.2 shows the time sequence used in Chapter 4 to encode the single-quantum FT-NMR spectrum, here modified to include a second detection period (an

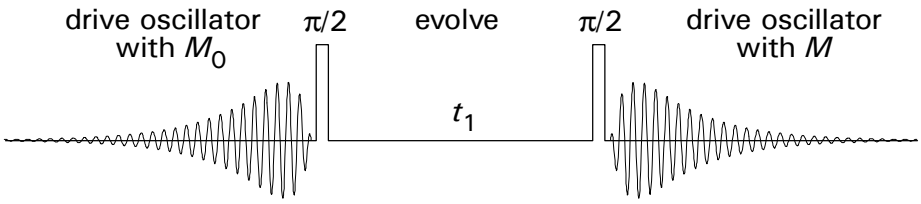

Figure 5.2. Time sequence for the CONQUEST method of encoding spectra pointwise. As in the first-order method (figure 4.3), two π/2 pulses are separated by a period t_1, which is incremented on successive shots of the experiment. The magnetization that survives the evolution period is measured by cyclically inverting it to drive the oscillator. In CONQUEST, a second period of driving is included before the first pulse to measure the fluctuation magnetization at the start of the encoding period. The signal for a given value of t_1 is defined as the product $M_0 M(t_1)$.

oscillator-driving interval) that precedes the evolution period. Consider the time-domain "second-order" signal

$$S_2(t_1) = M_{z,0}\, M_z(t_1), \tag{5.3}$$

which is formed on a given iteration by multiplying the result of the first measurement by the result of the second. What are the statistics of this signal compared to those of the ordinary (first-order) pointwise signal

$$S_1(t_1) = M_z(t_1)? \tag{5.4}$$

5.2.1 Mean and variance of the signals

We shall consider the simplest case of a sample containing N isochronous spins ½ in a device with negligible instrument noise so that we may reveal the essential features of the spin noise and the method. We shall also drop the units from Equations (5.3) and (5.4), calculating instead with the dimensionless angular momentum expressions

$$S_1(t_1) = I_z(t_1) \qquad \text{and} \qquad S_2(t_1) = I_{z,0}\, I_z(t_1). \tag{5.5a,b}$$

With measurements of longitudinal magnetization that are perfectly devoid of instrument noise, the results are always eigenvalues of the operator I_z. The probability of measuring the value m on the first measurement is

$$W(m) = Tr\{P_m \rho_0 P_m\} = Tr\{P_m \rho_0\}. \tag{5.6}$$

Here, ρ_0 is the thermal-equilibrium density operator and P_m is a projection operator associated with the eigenspace belonging to the eigenvalue m. Similarly, the joint probability of measuring the value m on the first measurement and k on the second measurement is

$$W(m,k) = Tr\{P_k U P_m \rho_0 P_m U^\dagger P_k\} = Tr\{U^\dagger P_k U P_m \rho_0\}, \tag{5.7}$$

where U is a time-evolution operator associated with the interval between the two measurements. The equilibrium density operator for this problem is

$$\rho_0 = \frac{1}{Q} e^{-H/k_B T}, \tag{5.8}$$

where

$$H = -\hbar\omega_0 I_z \qquad \text{and} \qquad Q \equiv Tr\{e^{-H/k_B T}\} \tag{5.9}$$

denote the Hamiltonian and the partition function.

In writing the last equalities in Equations (5.6) and (5.7), we have made use of the invariance of the trace to cyclic permutation of operators in a product, the idempotent property of projection operators ($P_m^2 = P_m$), and the fact that the

equilibrium density operator commutes with projections onto eigenspaces belonging to eigenvalues of the Hamiltonian, which is proportional to I_z.

Equation (5.7) may be used to calculate expectation values and variances for the first- and second-order signals $S_1(t_1)$ and $S_2(t_1)$. For example, the expectation value of $S_2(t_1)$ is found by multiplying the probability distribution $W(m,k)$ by m and k and then summing over all values of m and k:

$$\langle S_2(t_1)\rangle = \sum_{m,k} mkW(m,k) = \sum_{m,k} Tr\{U^\dagger kP_k UmP_m \rho_0\}. \tag{5.10}$$

We then recognize that $mP_m = I_z P_m$ and $\sum_m P_m = \mathbf{1}$ (and similarly for k) and write

$$\langle S_2(t_1)\rangle = Tr\{U^\dagger I_z U I_z \rho_0\} = Tr\{I_z(t_1) I_z \rho_0\} = \langle I_z(t_1) I_z\rangle, \tag{5.11}$$

where

$$I_z(t_1) = U^\dagger I_z U = I_z \cos(\omega t_1) - I_x \sin(\omega t_1) \tag{5.12}$$

is the Heisenberg-representation operator associated with the second measurement of I_z and ω is the Larmor frequency. We procede similarly for the expectation value of the first-order signal $S_1(t_1)$ and for the variances $\sigma_1^2(t_1) \equiv \langle S_1^2\rangle - \langle S_1\rangle^2$ and $\sigma_2^2(t_1) \equiv \langle S_2^2\rangle - \langle S_2\rangle^2$ and find

$$\langle S_1(t_1)\rangle = \langle I_z\rangle \cos\omega t_1, \tag{5.13}$$

$$\langle S_2(t_1)\rangle = \langle I_z^2\rangle \cos\omega t_1, \tag{5.14}$$

$$\sigma_1^2(t_1) = \left(\langle I_z^2\rangle - \langle I_z\rangle^2\right)\cos^2\omega t_1 + \langle I_x^2\rangle \sin^2\omega t_1, \tag{5.15}$$

$$\text{and } \sigma_2^2(t_1) = \left(\left\langle I_z^4 \right\rangle - \left\langle I_z^2 \right\rangle^2 \right) \cos^2 \omega t_1 + \left\langle I_x^2 I_z^2 \right\rangle \sin^2 \omega t_1 \qquad (5.16)$$

with the help of Equation (5.12). The expectation values on the right-hand sides of Equations (5.13–16) are with respect to the initial, thermal state ρ_0. Terms proportional to $\langle I_x \rangle$, $\langle I_x I_z + I_z I_x \rangle$, and $\langle (I_x I_z + I_z I_x) I_z^2 \rangle$ in Equations (5.13–16) are left out because they are easily shown to vanish.

Expectation values of powers of I_z are calculated straightforwardly from a moment generating function,

$$G(s) = \left\langle e^{isI_z} \right\rangle . \qquad (5.17)$$

Differentiation of $G(s)$ with respect to the argument s yields the expectation values:

$$\left\langle I_z^n \right\rangle = (-i)^n \left. \frac{d^n G}{ds^n} \right|_{s=0} . \qquad (5.18)$$

$G(s)$ is evaluated in terms of the number of spins N and the polarization p in Appendix D. The result is

$$G(s) = \left(\cos \frac{s}{2} + ip \sin \frac{s}{2} \right)^N . \qquad (5.19)$$

In accordance with Equation (5.18), the expectation values of the necessary powers of I_z are listed in Table 5.1. Also necessary are the expectation values $\left\langle I_x^2 \right\rangle$ and $\left\langle I_x^2 I_z^2 \right\rangle$,

m	$\left\langle I_z^m \right\rangle$
1	$\frac{1}{2} Np$
2	$\frac{1}{4} N\left(1 + (N-1)p^2\right)$
4	$\frac{1}{16} N\left(\begin{matrix} (3N-2) + 2(3N-4)(N-1)p^2 \\ + (N-3)(N-2)(N-1)p^4 \end{matrix} \right)$

Table 5.1. Expectation values of powers of I_z.

which can be calculated from $G'(s) \equiv \left\langle I_x^2 e^{isI_z} \right\rangle$. We recognize that in the expansion of the operator $I_x^2 = \left(\sum_i I_{x,i} \right)^2$, cross-terms like $I_{x,j} I_{x,k \neq j} e^{isI_z}$ are traceless, and so we find that $G'(s) = \frac{1}{4} N G(s)$ and that

$$\left\langle I_x^2 \right\rangle = \frac{1}{4} N \qquad \text{and} \qquad \left\langle I_x^2 I_z^2 \right\rangle = \frac{1}{4} N \left\langle I_z^2 \right\rangle. \tag{5.20a,b}$$

Results from Equations (5.13–20) are combined to compute the expectation values and variances of the first- and second-order signals, which are shown in Table 5.2.

a)	Expectation value	Variance
$S_1(t_1)$	$\frac{1}{2} Np \cos \omega t_1$	$\frac{1}{4} N \left(1 - p^2 \cos^2 \omega t_1\right)$
$S_2(t_1)$	$\frac{1}{4} N \left(1 + (N-1)p^2\right) \cos \omega t_1$	$\frac{1}{16} N \left(\begin{array}{c} N + (N-2)\cos^2 \omega t_1 \\ + \left(N + (3N-8)\cos^2 \omega t_1 \right)(N-1)p^2 \\ - (4N-6)(N-1)p^4 \cos^2 \omega t_1 \end{array} \right)$

b)	Expectation value	Variance
$S_1(t_1)$	$\frac{1}{2} Np \cos \omega t_1$	$\frac{1}{4} N$
$S_2(t_1)$	$\frac{1}{4} N \cos \omega t_1$	$\frac{1}{16} N \left(N + (N-2)\cos^2 \omega t_1\right)$

Table 5.2. Expectation values and variances of the first- and second-order signals. a) Exact expressions. b) Expressions to leading order in the polarization when $p\sqrt{N} << 1$.

5.2.2 Remarks

The signal-to-spin-noise ratio SNR_{spin} may be defined as the ratio of the expectation value to the square root of the variance. This quantity falls below unity for the $\cos \omega t_1 = 1$ values of the first-order signal when $p\sqrt{N} < 1$. Both the signal

and SNR_{spin} are proportional to the polarization, and in the limit of zero polarization there is no first-order signal that can be built up pointwise.

The signal-to-spin-noise ratio for the second-order signal is entirely different. In the limit of vanishing polarization, SNR_{spin} is independent of the polarization, and it is approximately unity for $N > 1$. A look at expectation values shows that the second-order signal has the same Fourier spectrum as the first-order signal. However, individual shots of the experiment for a given t_1 value can be co-added in the second-order signal without the individual contributors cancelling out on average as they do in the first-order signal when $p = 0$. The second order method can be used to measure a spectrum even with no spin order.

It is interesting to note that one can look at the "before" and "after" time series $M_{z,0}(t_1)$ and $M_z(t_1)$ individually, but, in the limit $p = 0$, they separately contain no information whatsoever about the spin system. The information in the spectrum is entirely contained in correlations. Under the influence of the pulse sequence and detection protocol, the spin populations determining measurements of I_z exhibit second-order coherence.

The "ring-down" aspect of the oscillator's motion depicted in Figure 5.2 during both the "before" and "after" detection periods may be somewhat misleading. In Figure 4.3, when a large mean magnetization is used to drive the oscillator on each shot, relaxation processes during the driving interval make the magnetization relax to near zero on average, and this causes a decrease in the oscillator amplitude with time t_2 during detection as shown. When the mean

magnetization is essentially zero to begin with compared to fluctuations, the magnetization used to drive the oscillator can be very far from a value that is indicative of the mean, and in fact it can have the opposite sign. Also, the detector oscillator will have some nonzero thermal amplitude and random phase at the start of a given driving interval, and memory of this information decays in the oscillator on the timescale of its ring-down time τ. There may be no net decrease in the oscillator's amplitude during driving on an individual shot "to zero" *per se*. The applied rf during the driving interval merely brings the state of the oscillator (its amplitude and phase) into correlation with the magnetization at a given time, with such time determined by the weighting of the oscillator's measured trajectory. By properly weighting the resulting transient, an estimate of the state of the magnetization at a preferred time is obtained. It is *this weighting* that is meant to be suggested by the trajectories in both the before and after detection periods, and not a decay to zero amplitude of the oscillator. The possible effective length of the weighting function will be on the order of a few times T_{1a}.

A better way to view the detection period is that the applied inversion sequence brings the spin system into contact with the oscillator by providing a common spectral density at the oscillator frequency. Another interesting feature of the second-order method is that there is no need to restore an equilibrium magnetization. The *SNR* is independent of polarization, so the experiment's repetition rate is not limited by waiting for spin order. We have called this method of encoding spectra into the second-order signal Correlated Observations Narrow Quantum Uncertainty, Enhancing Spectroscopic Transients (CONQUEST)[6-8].

5.3 BOOMERANG for Surface-Bound Samples

In Chapter 2 and in Appendix B, the expression for the force on a detector dipole (Equation (2.1)) exerted by a unit dipole of sample magnetization was used to find the sensor magnet shape that optimized the force signal-to-noise ratio for a sample contained in a spherical volume, and it was found that a right circular cylinder was nearly ideal and in fact the best shape given requirements of ease of manufacture and homogeneity. Consider now a circular "2-D" sample with given radius r_s, which could be composed of sites at an interface or a molecular monolayer deposited on a crystal surface. We can use Equation (2.1) to construct a force map in the vicinity of this flat sample to guide our design of a suitable sensor for this sample's magnetization. Figure 5.3 shows the force map. The picture suggests we use a circular cylinder with its radius approximately that of the sample.

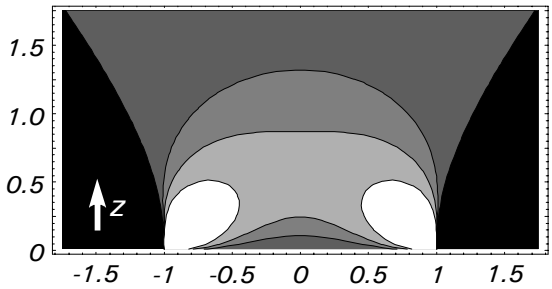

Figure 5.3. Force map over a flat circular sample. The sample is in the transverse plane perpendicular to the *z*-axis at z = 0, and both the sample and the detector moments are aligned along the z-axis. Each contour represents a factor of two increase in the magnitude of the vertical force on a detector dipole at that location. The force is directed oppositely in the region colored black. Numerical labels on the axes represent distance in units of the sample's radius.

Substitution of differential dipole elements into Equation (2.1) and integration over both a flat sample of radius r_s and surface magnetization density $\overline{M}_s$ and a cylindrical detector magnet of radius a, height h, magnetization M_d, and distance from the sample R_{max} yields the force

$$F_z = -\mu_0 \overline{M}_s M_d \sqrt{a r_s} \left(\frac{(2-m^2)K(m^2) - 2E(m^2)}{m} - \frac{(2-k^2)K(k^2) - 2E(k^2)}{k} \right), \quad (5.21)$$

where

$$m^2 = \frac{4 a r_s}{(R_{max} + h)^2 + (a + r_s)^2} \quad \text{and} \quad k^2 = \frac{4 a r_s}{R_{max}^2 + (a + r_s)^2} \quad (5.22a,b)$$

and where K and E are the complete elliptic integrals of the first and second kinds. When combined with the relevant expression for the force noise expected for a detector magnet attached to a massless suspension, the resulting signal-to-(Brownian)-noise ratio diverges as the R_{max} parameter goes to zero. This limit is unrealistic anyway, as space to accommodate NMR coil windings and to provide adequate field homogeneity is required, as is relaxation of the zero-inert-mass approximation. We thus optimize the detector magnet's dimensions for a specific case only.

Suppose the sample is a 100 μm diameter circle with a surface density of one ^{13}C spin per square nanometer, and suppose we set R_{max} equal to 10 μm. This might be the case were we to investigate chemical shift tensors at 125 MHz in an oriented monolayer of organic molecules deposited on an optical fiber, perhaps to see how the monolayer is modified by a covalently bound fluorophore in the fabrication of an immunosensor. In this case the optimal radius and height of the detector magnet are found to be 50.0 μm and 22.4 μm as shown in Figure 5.4. In that case the single-shot *SNR* is predicted to be about unity given an oscillator with a one-second ring-down time and $T_{1a} = 1$ s. In order to increase sensitivity, we have assumed that the polarization has been enhanced to 1% using optically polarized

^{3}He or ^{129}Xe. Polarization of solvents and of dissolved and surface species with noble gases are the subject of much recent interest[9-12], and polarization enhancements of 1000 have been reported at low fields in favorable cases. Whether enhancements to a few percent polarization can be made generally on surfaces is not clear, but surface species are likely to be particularly amenable to large and rapid enhancement.

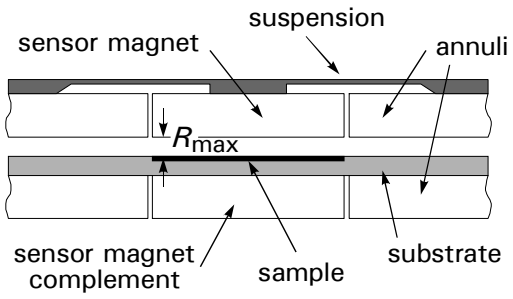

Figure 5.4. BOOMERANG for surface samples. The sensor magnet is drawn with dimensions that optimize sensitivity for the given sample radius and R_{max}.

The selection of a sample region in surface studies poses an interesting problem. One solution is to deposit the samples into the desired circular shape using a mask or ink-jet printer method. This would be convenient, especially for rapidly depositing many samples, but then the spectra might suffer from "edge effects" under some circumstances, where the chemical conditions at the edges of the sample disk are not indicative of the bulk of a more homogeneous surface. In that case it would be desirable to select a sample magnetically from a larger, more uniform film. Figure 5.5 shows how this might be accomplished with dc field pulses from a coil included in the apparatus for this purpose. The activated region could then be shuttled into a highly homogeneous field for evolution and then subsequently under a sensor magnet for detection.

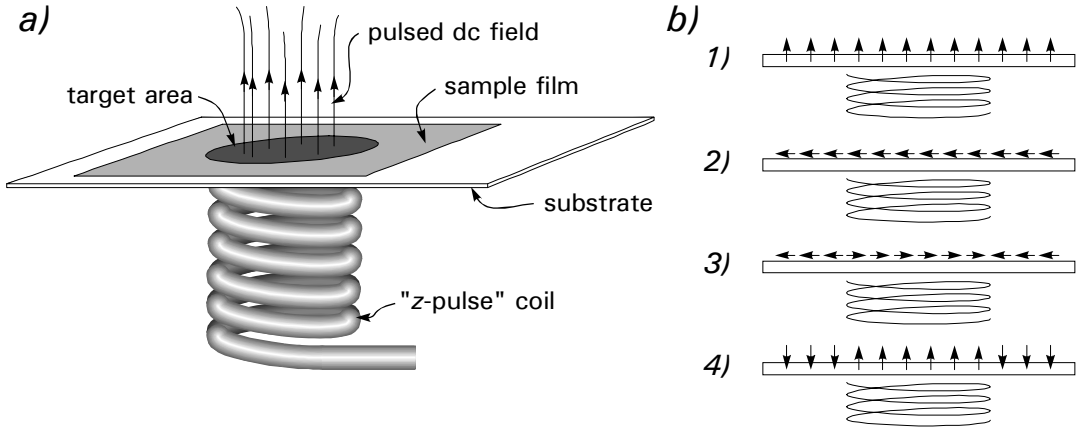

Figure 5.5. Magnetic selection of sample region. a) Substrate with sample film is slid into place over a coil that can produce a highly localized switched dc offset in the static field. b) Sample selection process. (1) Initial state. (2) $\pi/2$ pulse is applied to entire sample. (3) localized field ("*z*-pulse") is switched on long enough to advance the phase of the spins in the circular target area by π relative to surrounding spins. (4) $\pi/2$ pulse is applied to entire sample to create localized longitudinal magnetization for use in BOOMERANG.

5.4 Torsional BOOMERANG for Nanoscopic Samples

The analysis presented in Chapter 2 on scaling of the signal-to-noise ratio assumed that the frequency of the oscillator could be maintained in the audiofrequency range as the apparatus was scaled down for smaller samples. This can be done if the experimenter has independent control over the balance between elastic and magnetic spring constants or has other (active) means of control over the frequency[3]. However, this balance may become an increasingly difficult engineering challenge as the size scale of the detection apparatus is reduced into the sub-micron range. At higher frequencies, the increased rf power necessary to efficiently invert magnetization may cause other problems, such as heating of the sample or oscillator. It is therefore our concern in this section to address BOOMERANG with precessing or spin-locked *transverse* magnetization.

Figure 5.6 shows designs for BOOMERANG based on torsional resonance. The resonance frequencies of the moving parts coincide with the Larmor frequency of the spin system. The magnetic parts are all magnetized along the vertical in the figure as in longitudinal BOOMERANG, and this feature, perhaps in combination with external magnets not shown, provides a static field for the sample. However, the moving parts of the detector assembly are supported so as to make use of a net torque exerted by the sample's transverse magnetization.

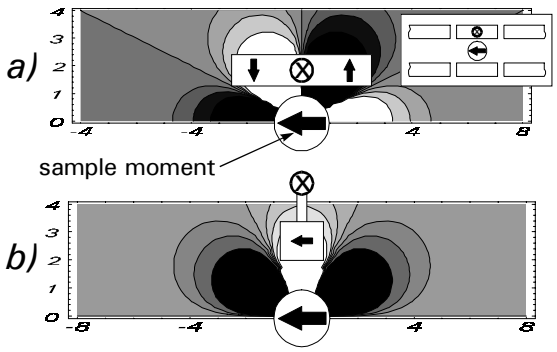

Figure 5.6. Force maps for design of torsional oscillators driven by transverse magnetization. Light and dark colors indicate forces of opposite sign. Each contour represents a factor of two increase in the magnitude of the force on a vertical detector dipole at that location. a) *z*-component of the force suggests a flat disk that undergoes torsional oscillations around the axis shown. b) *x*-component of the force suggests a pendulum-type oscillator. Numerical labels on the axes represent distance in units of the sample volume's radius. The inset to figure (a) shows the sensor as part of a BOOMERANG assembly.

It is known that torsional oscillators can have substantially better anchor losses[13] than cantilevered or other longitudinal oscillators. The main reason is probably that the moving element's center of mass remains fixed, and so there is no momentum transfer to the substrate. This is also a feature of the sound-bars in mallet-percussion instruments like the xylophone, which are fixed to their supports at nodes in their fundamental mode of vibration. Figure 5.7 shows a sensor magnet fixed to an oscillator suspension based on this idea. Such xylophone designs might be useful at size scales where longitudinal detection is still practical but where eddy-current damping has been suppressed, and so anchor losses are predominant.

Unfortunately, magnetic materials are typically much more dense than silicon and other structural materials used in microfabrication. Calculations using magnetic masses fixed to a xylophone-bar oscillator show that there would have to be rather large inert ballast masses on both ends of the xylophone-bar in order to satisfy the desired condition that the magnetic mass lies entirely between the oscillator supports. This inert mass lowers the detector's sensitivity for the case of a single sensor and a single sample. However, the figure suggests the possibility that these masses are not inert, but are instead other magnets driven by other samples.

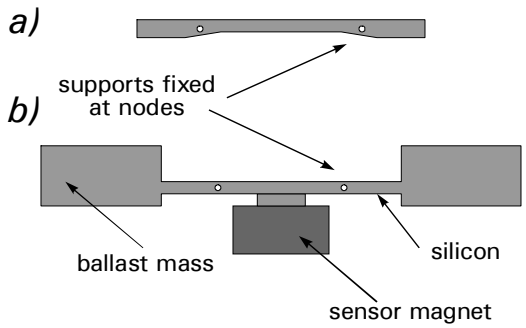

Figure 5.7. Xylophone-bar oscillators. a) Xylophone bar showing support points, which are nodes in the principal oscillatory mode by design. b) Silicon oscillator inspired by xylophone bar fixed to sensor magnet. Since magnet materials are so much more dense than silicon, substantial inert mass must be added to the oscillator. This suggests than more than one sensor oscillator be mechanically coupled together to drive a mode of a composite oscillator, with each sensor separately forced by its own sample.

5.5 Final Remarks – On Partitioning Samples and Microfabrication of Advanced Analytical Instruments

This chaining together of detector magnets each with its own sample is of far more than academic interest. One reason for such a composite detector is to improve sensitivity to average magnetization in a single sample that can be broken up into pieces. Suppose we have an NMR detection method whose *SNR* for a sample of linear dimension r is proportional to r^n. If the sample is broken into N

equal pieces, then the length scale of each piece is $r / N^{1/3}$ and the *SNR* from each piece will be proportional to $(r / N^{1/3})^n$ if its spectrum is measured with a detector optimized at the smaller size scale. An average of the signals from each piece should have a *SNR* $N^{1/2}$ times larger — $N^{1/2} (r / N^{1/3})^n = N^{1/2-n/3} \times r^n$.

This *SNR* expression exhibits a cutoff scaling factor, $n = 3/2$, below which it should be possible to increase the signal-to-noise ratio simply by breaking up the sample. For example, in BOOMERANG on 3-D samples (where $n = 1/2$), breaking up the sample results in a modest increase in sensitivity (proportional to $N^{1/3}$). As a flat sample's area scales only quadratically with *r*, *SNR* in BOOMERANG on 2-D samples is easily shown to have a scaling factor $n = -1/2$, and so surface BOOMERANG is particularly compatible with sensitivity enhancement by breaking up the sample (proportional to $N^{2/3}$). If it is possible to microfabricate massively parallel detectors at scales where instrument noise can be made negligible compared to spin noise, then a preferred approach for typical liquid samples would be to break each sample up as small as possible, as the *SNR* for second-order signals encoded with CONQUEST scales as r^0 (resulting in a sensitivity advantage to breaking up the sample that goes as $N^{1/2}$).[†] Designs, detailed microfabrication procedures, and preliminary results of microfabricated BOOMERANG devices are detailed by Madsen[3].

[†] Conversely, for inductive detection ($n = 2$), there is actually a very slight (proportional to $N^{1/6}$) advantage to *combining* samples (or merely putting them in the same NMR coil in different combinations).

The other reason for composite detectors brings up the much more general question of optimizing procedures and instrumentation to maximize extraction of information from a given *set* of samples. By combining microfabrication of detector arrays with micro-patterning of sample libraries, one could imagine building modes of a composite oscillator that are designed to be driven by *specific characteristics* of the whole library. Suppose, for example, that a surface is coated with an oriented enzyme-bearing lipid bilayer and a substrate is deposited so that its concentration is proportional to the function $\frac{1}{2}+\frac{1}{2}\cos kx$, where x denotes distance along some axis tangent to the surface. Then, if the concentration of a reaction product grows as the square of the substrate concentration (as in a second-order reaction, for example), there will be a component to the driving force on a composite oscillator during a suitably designed detection period at the spatial frequency $2k$, which will be absent if the reaction is first-order. Optimization procedures for such informational characteristics of sets of samples are an intriguing generalization of the theory of Chapter 2.

References

1 N. Wu, T. L. Peck, A. G. Webb, R. L. Magin, and J. V. Sweedler, *Anal. Chem.* **66,** 3849 (1994).

2 N. Wu, T. L. Peck, A. G. Webb, R. L. Magin, and J. V. Sweedler, *J. Am. Chem. Soc.* **116,** 7929 (1994).

3 L. A. Madsen, Ph. D. Thesis, California Institute of Technology, 2002.

4 T. George, *et al.*, in *IEEE Aerospace Conference* (Big Sky, Montana, 2001).

5 J. A. Sidles, J. L. Garbini, K. J. Bruland, D. Rugar, O. Züger, S. Hoen, and C. S. Yannoni, *Rev. Mod. Phys.* **67,** 249 (1995).

6 P. J. Carson, L. A. Madsen, G. M. Leskowitz, and D. P. Weitekamp, *Bull. Am. Phys. Soc.* **44,** 541 (1999).

7 P. J. Carson, L. A. Madsen, G. M. Leskowitz, and D. P. Weitekamp, U. S. Patent No. 6,081,119 (California Institute of Technology, USA, 2000).

8 P. J. Carson, L. A. Madsen, G. M. Leskowitz, and D. P. Weitekamp, U. S. Patent No. 6,087,872 (California Institute of Technology, USA, 2000).

9 S. Appelt, F. W. Haesing, S. Baer-Lang, N. J. Shah, and B. Blumich, *Chem. Phys. Lett* **348,** 263 (2001).

10 H. Desvaux, T. Gautier, G. Le Goff, M. Petro, and P. Berthault, *Euro. Phys. J. D* **12,** 289 (2000).

11 J. Smith, L. J. Smith, K. Knagge, E. MacNamara, and D. Raftery, *J. Am. Chem. Soc.* **123,** 2927 (2001).

12 T. Room, S. Appelt, R. Seydoux, E. L. Hahn, and A. Pines, *Phys. Rev. B* **55,** 11604 (1997).

13 T. A. Barrett, C. R. Miers, H. A. Sommer, K. Mochizuki, and J. T. Markert, *J. Appl. Phys.* **83,** 6235 (1998).

Appendix A: Connections to Other Mechanical Detection Methods

The "ideal detection sphere" arguments leading up to the BOOMERANG detector of Figure 1.3 represent a significant break from the conceptual development of the several other force-detected magnetic resonance methods shown, with BOOMERANG, in Figure A.1. The more traditional line of thinking has

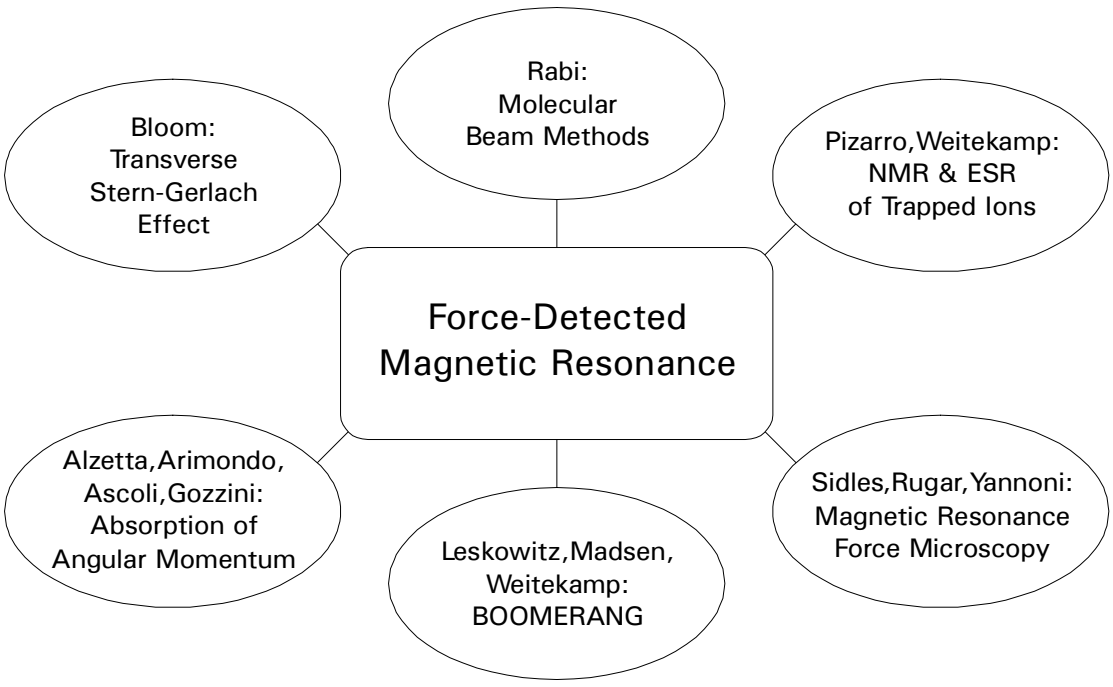

Figure A.1. Force-detected magnetic resonance methods.

been characterized by a "Stern-Gerlach" view, which has pervaded the field since the very first method of magnetic resonance, the Rabi molecular beam method[1] (which preceded by 8 years the observation of magnetic resonance in condensed phases using magnetic induction by Purcell[2] and Bloch[3]).

Rabi's method makes use of the Stern-Gerlach effect, the state-dependent force **F** on a spin-magnetic dipole $\boldsymbol{\mu}$ in an inhomogeneous static field:

$$\mathbf{F} = \boldsymbol{\mu} \cdot \mathbf{G} . \qquad (A.1)$$

Here, $\mathbf{G} = \partial \mathbf{B} / \partial \mathbf{r}$ is the gradient tensor of the static field **B** with respect to the spatial coordinates **r**. This force spatially separates populations of molecules in a beam by the eigenvalue of the projection of their spin angular momentum onto the static field direction. An applied rf field induces spin flips that reverse the initial deflections of the separate populations, modulating the intensity of the molecular beam at a detector in accordance with the spin-resonance condition. A Stern-Gerlach separation of eigenstates of precessing *transverse* angular momentum for magnetic resonance of molecular beams was later proposed[4] and demonstrated[5] by Bloom and coworkers.

Both the spectroscopic resolution and sensitivity of these methods is limited by the residence time of the spins in the field. A key improvement in force-detected magnetic resonance is to keep the spins in the field for a longer time by confining them to a harmonic motion, applying the forcing fields at the mechanical resonance frequency of that motion. This is a feature of proposals by Pizarro and Weitekamp to detect electron spin resonance (ESR) and NMR of electromagnetically trapped

ions by way of a resonance-induced change in the amplitude of their orbits using switched field gradients[6-8].

Spin-dependent mechanical resonance is also a feature of a torque-detection method for magnetic resonance of condensed phases in homogeneous fields, which was introduced in the 1960's by Gozzini and coworkers[9-14]. In those experiments, a spin-bearing solid sample (the solid free-radical diphenylpicrylhydrazyl, DPPH) suspended in a homogeneous magnetic field is made to absorb angular momentum from an rf field applied at the frequency of spin precession. The sample spins, which are bound to a torsional oscillator, transmit their acquired angular momentum via rapid thermalization with the lattice to the oscillator, which therefore experiences a torque. This absorption of angular momentum from the applied field is analogous to the absorption of power from the field attempted long ago by Gorter[15] and finally observed as a rise in temperature of the sample by Schmidt and Solomon[16]. While these methods may be used in a homogeneous field, the thermalization of angular momentum or of energy with the lattice, a necessary component of the methods, limits their use in the great majority of modern NMR pulse sequences, which rely on persistence of spin coherence through numerous rf pulses.

Mechanical detection was revived in the context of condensed phases by Sidles, who proposed a "folded Stern-Gerlach effect"[17] — the resonant driving of small oscillators, such as force-microscope cantilevers, with spin-dependent forces in accordance with Equation (A.1). The version of this proposal that has been implemented uses cyclic adiabatic rapid passage (ARP) or cyclic saturation to

modulate longitudinal magnetization at an audio frequency in the presence of a field gradient, driving the oscillator to which either the sample[18,19] or a small ferromagnetic particle[20], which provides the gradient, is attached. The ferromagnetic particle serves the dual purpose of providing a coupling force and varying the spin-resonance condition across the sample volume, which provides an imaging capability. The first experimental demonstration of this approach, which is now called magnetic resonance force microscopy (MRFM), was performed in Daniel Rugar's laboratory at IBM Almaden[18]. This first demonstration was an ESR experiment with solid DPPH bound to the cantilever. Subsequently, MRFM as been extended to proton[19], and fluorine[21] NMR and to ferromagnetic resonance in cobalt thin films[22].

The sensitive-slice imaging capability of MRFM bears resemblance to Damadian's magnetic resonance imaging method[23,24]. MRFM was also originally motivated by biological imaging — although at a dramatically reduced size scale. Rugar and Sidles have attempted to set the groundwork for a means of imaging biomolecules magnetically, angstrom-thick slice by angstrom-thick slice. A very challenging intermediate goal is detection of magnetic resonance from single electrons using MRFM, and to this end great strides have been made, particularly in Rugar's laboratory, such that as of this writing it is now possible to observe magnetic forces with sub-attonewton per root hertz sensitivity at cryogenic temperatures[25]. This is in principle sufficient to observe resonance from single electrons, but so far efforts have been unsuccessful[26].

In light of the history behind Equation (A.1), it is not surprising that authors describing molecular beam and MRFM-type force detection propose use of the highest gradients possible. The experimental trend in MRFM has been toward ever-increasing gradients, and as of this writing MRFM has been performed with gradients as large as 250 kT/m[27]. But, as we have seen in Chapter 1, no gradients are in fact needed to observe magnetic resonance with force detection, and there are very good reasons for avoiding their use. What is going on here?

The answer lies in the choice of a mathematical model for the sample. In Equation (A.1), the "sample" is a point dipole.

The geometric optimization described in Chapter 2 takes into account the shape and size of a *whole* sample and asks the question of what detector provides optimal signal-to-noise *for that sample*.[†] Our choice of a sphere with a specified R_{max} is based on computational simplicity and also on the fact that for powdered samples and fluids, one can arrange to pack the sample into a sphere. Often in solid-state magnetic resonance, even single crystals are shaped into spheres to mitigate susceptibility effects. In commercial (inductive) instruments for both solids and liquids, the effective sample volume is most often a cylinder with near-unit aspect

[†] Specifically, the uncertainty in the measurement of the *average* magnetization of the sample is the observable that is optimized. This is not the only one that might be considered. For example, the "local sensitivity" alluded to in Chapter 3 varies over the sample volume by more than an order of magnitude. It might be of interest to optimally assess anisotropies in some heterogeneous sample. The information-theoretic question of how best to generalize the optimization given arbitrary constraints is well worth serious consideration.

ratio, a close match to a sphere mathematically. A sphere is in any case a first approximation to *any* 3-D sample.

Which brings us back to the point dipole. This sample can be viewed as a sphere with vanishing R_{max}. The theory of Chapter 2 is applicable, and in this special case, a moving sensor magnet designed for optimal detection is as small as possible and as close as possible to the sample dipole. *In the absence of any compensation magnets* this leads to the conclusion that higher gradients mean better sensitivity, as the detector would impose the largest possible gradient at the position of the sample dipole[28].

The difficulty of constructing nanoscopic BOOMERANG magnet assemblies with narrow gap spacings, relative to single magnet particles on cantilevers, is apparent. If the goal is to observe magnetic resonance from a single, isolated, fixed spin (nuclear or electronic), then the BOOMERANG concept is probably more trouble than it is worth. If the (single) spin is not in a fixed location, but instead is diffusing in a target volume or on a surface, then the elimination of field gradients is again relevant. It is almost always the case that the real information sought from an experiment is hidden in a volume that is at least as large as a molecule. Even imperfect composite magnet assemblies that allow a larger sample region with many spins during detection can extract *information* at a greater rate than can be had one spin at a time.

Single-electron-spin sensitivity in MRFM may well be achieved in the very near future, and the very much more challenging observation of magnetic resonance from single nuclear spins may also be possible in theory. But the probable range of

superiority of force-detection over inductive detection (as regards sensitivity) is between 10^0 and 10^{12} or so spins in volumes of up to approximately 0.1 mm^3. Such samples possess enormous information content that may best be extracted by whole-sample BOOMERANG methods, and we have proceeded accordingly in our efforts.

References

1 I. I. Rabi, J. R. Zacharias, S. Millman, and P. Kusch, *Phys. Rev.* **53,** 318 (1938).

2 E. M. Purcell, H. C. Torrey, and R. V. Pound, *Phys. Rev.* **69,** 37 (1946).

3 F. Bloch, W. W. Hansen, and M. Packard, *Phys. Rev.* **70,** 474 (1946).

4 M. Bloom and K. Erdman, *Can. J. Phys.* **40,** 179 (1962).

5 M. Bloom, E. Enga, and H. Lew, *Can. J. Phys.* **45,** 1481 (1967).

6 P. J. Pizarro and D. P. Weitekamp, *Bull. Magn. Reson.* **14,** 220 (1992).

7 D. P. Weitekamp and P. J. Pizarro, U.S. Patent No. 4,982,088 (California Institute of Technology, USA, 1991).

8 P. J. Pizarro, Ph. D. Thesis, California Institute of Technology, 1994.

9 A. Gozzini, in *XII Colloque Ampere* (Bordeaux, 1963), pp. 82.

10 E. Arimondo, *Il Nuovo Cimento* **52 B,** 379 (1967).

11 G. Alzetta, E. Arimondo, C. Ascoli, and A. Gozzini, *Il Nuovo Cimento* **52 B,** 392 (1967).

12 G. Alzetta, E. Arimondo, and C. Ascoli, *Il Nuovo Cimento* **54 B,** 107 (1968).

13 E. Arimondo, *Ann. Phys.* **3,** 425 (1968).

14 C. Ascoli, P. Baschieri, C. Frediani, L. Lenci, M. Martinelli, G. Alzetta, R. M. Celli, and L. Pardi, *Appl. Phys. Lett.* **69,** 3920 (1996).

15 C. J. Gorter, *Physica* **3,** 995 (1936).

16 J. Schmidt and I. Solomon, *J. Appl. Phys.* **37,** 3719 (1966).

17 J. A. Sidles, *Phys. Rev. Lett.* **68,** 1124 (1992).

18 D. Rugar, C. S. Yannoni, and J. A. Sidles, *Nature* **360,** 563 (1992).

19 D. Rugar, O. Züger, S. Hoen, C. S. Yannoni, H.-M. Vieth, and R. D. Kendrick, *Science* **264,** 1560 (1994).

20 K. Wago, D. Botkin, C. S. Yannoni, and D. Rugar, *Appl. Phys. Lett.* **72,** 2757 (1998).

21 K. Wago, O. Züger, R. Kendrick, C. S. Yannoni, and D. Rugar, *J. Vac. Sci. Technol. B* **14,** 1197 (1996).

22 P. C. Hammel, B. J. Suh, Z. Zhang, M. Midzor, M. L. Roukes, and J. R. Childress, *Bull. Am. Phys. Soc.* **43,** 171 (1998).

23 R. Damadian, *Science* **171,** 1151 (1971).

24 R. Damadian, U. S. Patent No. 3,789,832 (1972).

25 H. J. Mamin and D. Rugar, *Appl. Phys. Lett.* **79,** 3358 (2001).

26 J. D. Hannay, R. W. Chantrell, and D. Rugar, *J. Appl. Phys.* **87,** 6827 (2000).

27 K. J. Bruland, W. M. Dougherty, J. L. Garbini, J. A. Sidles, and S. H. Chao, *Appl. Phys. Lett.* **73,** 3159 (1998).

28 G. M. Leskowitz, L. A. Madsen, and D. P. Weitekamp, *Sol. St. Nucl. Magn. Reson.* **11,** 73 (1998).

Appendix B: Sensor Optimization

B.0 Global Optimization with Massless Support

In this appendix, we calculate the shape of the detector magnet that optimizes sensitivity in a measurement of a spherical sample's average magnetization given a condition of closest approach to the sample's surface. The quantity to be optimized is the signal-to-noise ratio of the measurement, which we defined in Chapter 2 (Equation (2.6)):

$$SNR_{\mathrm{BOOM}} = F_{\mathrm{z,rms}}/F_{\mathrm{N}} \ . \tag{B.1}$$

We begin by parameterizing the shape of the detector. Symmetry requires that the detector be a solid of revolution about the axis along which it will be displaced, which we take to be the *z*-axis. Figure B.1 shows a detector magnet above a spherical sample, with a distance of closest approach, R_{max}, defined along the *z*-axis relative to the center of the sample. We also take the center of the sample to be

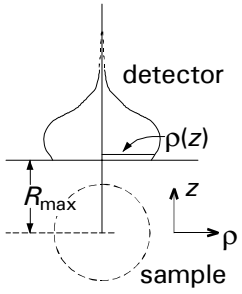

Figure B.1. Curve defining the detector magnet, which is a solid of revolution.

the origin of a cylindrical coordinate system. The most general parameterization of the sensor magnet's shape given the symmetry restriction is a function,

$$\rho = \rho(z), \tag{B.2}$$

that defines the surface of the sensor magnet. This function is single-valued, greater than or equal to zero everywhere, and defined on the interval $\{z \mid R_{\max} \le z < \infty\}$, but is otherwise unrestricted.

The total root-mean-squared (rms) force on the detector is the integral of the forces on dipole elements in the detector,

$$F_{z,\mathrm{rms}} = \frac{w}{\sqrt{2}} \int_{\substack{\text{detector} \\ \text{volume}}} \hat{\mathbf{z}} \cdot \mathbf{dF}, \tag{B.3}$$

reduced by the factor $\sqrt{2}$ relative to the static force and scaled by a factor w, which accounts for the amplitude of the Fourier component of the force for a specfic driving protocol (see Chapter 2). Due to the cylindrical symmetry of the system, only the z-components of the forces add in concert, and so, following Chapter 2, we sum up the contributions of the z components only. The integrand in Equation (B.3) may be written (see Chapter 2)

$$\hat{\mathbf{z}} \cdot \mathbf{dF} = \frac{\mu_0}{4\pi} \frac{V_s M_s M_d}{r^4} \left(9 - 15\cos^2\theta\right)\cos\theta dV_d, \tag{B.4}$$

where V_s is the sample's volume, M_s is its magnetization, M_d is the magnetization of the detector magnet, $r = \sqrt{z^2 + \rho^2}$ is the distance of the given detector dipole from

the origin, and θ is the polar angle at the location of the detector dipole. With the substitutions $r^2 = z^2 + \rho^2$, $\cos\theta = \frac{z}{r}$, and $dV_d = \rho d\rho d\phi dz$, we may write

$$F_{z,rms} = \frac{w}{\sqrt{2}} \frac{\mu_0}{4\pi} V_s M_s M_d \int_0^{2\pi} d\phi \int_{R_{max}}^{\infty} z dz \int_0^{\rho(z)} \frac{9\rho^2 - 6z^2}{\left(z^2 + \rho^2\right)^{7/2}} \rho d\rho \tag{B.5}$$

for the rms force. Evaluating the integrals over ρ and the azimuthal angle φ, we find

$$F_{z,rms} = -\frac{3}{2} \frac{w}{\sqrt{2}} \mu_0 M_s M_d V_s \int_{R_{max}}^{\infty} f(z, \rho(z)) dz \,, \tag{B.6}$$

where

$$f(z, \rho(z)) = \frac{z\rho^2}{r^5} \tag{B.7}$$

and

$$r = r(z) = \sqrt{z^2 + \rho(z)^2} \,. \tag{B.8}$$

Equation (B.6) shows that the signal force $F_{z,rms}$ is a functional whose value depends on the parameterizing relation $\rho = \rho(z)$. The noise force F_N in the denominator of Equation (B.1) is also a functional of ρ. To find this functional, we first write

$$F_N = \sqrt{4 k_B T \alpha \Delta f} \,, \tag{B.9}$$

where T is the temperature of the detector oscillator, Δf is the bandwidth of the measurement, and α is the oscillator's damping constant (Equation (2.8)). α is proportional to the oscillator's motional mass m, which we assume is dominated by the mass of the magnetic detector. (In section B.1 we relax this assumption for the simpler case of a right circular cylinder.) For a magnet with cylindrical symmetry, α

can be written in terms of the damping rate γ, the density η of the detector material, and the volume of the magnet:

$$\alpha = m\gamma = \gamma\eta \int_{\substack{\text{detector}\\ \text{volume}}} dV = \gamma\eta \int_{R_{\max}}^{\infty} \pi\rho^2 dz = \pi\gamma\eta \int_{R_{\max}}^{\infty} v(z,\rho(z))dz \,. \tag{B.10}$$

where
$$v(z,\rho(z)) = \rho^2 \,. \tag{B.11}$$

The explicit definition of the symbols *f* and *v* for the integrands in Equations (B.7) and (B.11) will help simplify the notation in the discussion that follows.

Now, let

$$\tilde{J} = SNR_{\text{BOOM}}^2 = \frac{F_{\text{z,rms}}^2}{F_{\text{N}}^2} \,. \tag{B.12}$$

Substituting in the expressions for the signal and noise forces and collecting constant factors that do not depend on the shape function ρ, we write

$$\tilde{J} = \left(\frac{9}{32\pi} \frac{w^2 \mu_0^2 M_{\text{s}}^2 M_{\text{d}}^2 V_{\text{s}}^2}{k_{\text{B}} T \eta \gamma \Delta f} \right) J \tag{B.12}$$

and
$$J = \frac{F^2}{V} \,, \tag{B.13}$$

where
$$F = \int_{R_{\max}}^{\infty} f(z,\rho(z))dz \quad \text{and} \quad V = \int_{R_{\max}}^{\infty} v(z,\rho(z))dz \,. \tag{B.14a,b}$$

The optimal sensor shape is defined by the function $\rho(z)$ that extremizes the signal-to-noise ratio. Since all we have done is to square SNR_{BOOM} and remove constant factors in deriving Equation (B.13), a necessary and sufficient condition is

that J is extremized. To find the optimum function $\rho(z)$, we consider the variation δJ in J caused by arbitrary infinitesimal variations in $\rho(z)$ about its optimum. When $\rho(z)$ is optimal, J is stationary with respect to these variations, and so in accordance with Equation (B.13) we write

$$\delta J = \frac{2VF\delta F - F^2\delta V}{V^2} = \frac{F}{V^2}\left(2V\delta F - F\delta V\right) = 0\,. \tag{B.15}$$

Since neither of the integrals F nor V are zero, we must have

$$2V\delta F - F\delta V = 0\,, \tag{B.16}$$

where, since the limits on the integrals are fixed,

$$\delta F = \int_{R_{\max}}^{\infty} \delta f(z,\rho)dz \quad \text{and} \quad \delta V = \int_{R_{\max}}^{\infty} \delta v(z,\rho)dz\,. \tag{B.17a,b}$$

The variations in the integrands are directly proportional to the functional variation $\delta\rho$ in $\rho = \rho(z)$:

$$\delta f = \frac{\partial f}{\partial \rho}\delta\rho\,;\ \delta v = \frac{\partial v}{\partial \rho}\delta\rho\,, \tag{B.18a,b}$$

where

$$\frac{\partial f}{\partial \rho} = \frac{z\rho}{\left(z^2+\rho^2\right)^{7/2}}\left(2z^2 - 3\rho^2\right) \tag{B.19}$$

and

$$\frac{\partial v}{\partial \rho} = 2\rho\,. \tag{B.20}$$

Using Equations (B.17–18), we may rewrite Equation (B.16) as

$$2V\int_{R_{\max}}^{\infty}\frac{\partial f}{\partial \rho}\delta\rho dz - F\int_{R_{\max}}^{\infty}\frac{\partial v}{\partial \rho}\delta\rho dz = 0 \tag{B.21}$$

or, since V and F are just numbers (functionals of $\rho(z)$),

$$\int_{R_{\max}}^{\infty} \left(2V \frac{\partial f}{\partial \rho} - F \frac{\partial v}{\partial \rho} \right) \delta\rho \, dz = 0 \qquad \text{(B.22)}$$

According to the fundamental theorem of the calculus of variations[1], in order for this integral to vanish for *arbitrary* variations $\delta\rho$ in the shape function $\rho(z)$, we must have

$$2V \frac{\partial f}{\partial \rho} - F \frac{\partial v}{\partial \rho} = 0 \, . \qquad \text{(B.23)}$$

Equation (B.23) is analogous to the Euler-Lagrange equations that result from extremizing action in the Lagrangian formulation of mechanics. It is worth recalling that this equation is a prescription for solving for that function $\rho = \rho(z)$ which satisfies an extremum principle, in this case the optimal signal-to-noise ratio. Note that, in contrast to Euler-Lagrange equations (and other such equations as arise in the calculus of variations, like the so-called "brachistochrone" problem[2]), Equation (B.23) is not a differential equation, as the derivative $\rho'(z)$ appears nowhere in (B.23). It is in fact an integral equation that has in it the functionals $F[\rho(z)]$ and $V[\rho(z)]$, which are *numbers*, and not functions of the variable z *per se*.

With the help of equations (B.19, 20, and 8), we rewrite Equation (B.23) in the form:

$$\frac{F}{2V} = \frac{\partial f / \partial \rho}{\partial v / \partial \rho} = \frac{1}{2} \frac{z}{r^7} \left(5z^2 - 3r^2 \right). \qquad \text{(B.24)}$$

The left-hand side of Equation (B.24) is a *number*, a functional of the whole function $\rho(z)$, and not an explicit function of z, and therefore the right-hand side may be set equal to a constant:

$$\lambda^{-4} \equiv \frac{F}{2V} = \frac{1}{2}\frac{z}{r^7}\left(5z^2 - 3r^2\right). \tag{B.25}$$

An even power of λ is allowed because the right hand side is never less than zero. The quartic exponent is chosen so that λ will have the dimensions of length (λ's significance will become clear shortly).

Equation (B.25) can be viewed as a relation that defines the function $\rho(z)$ implicitly, but it is best solved as an equation for $r = r(z(\theta)) = \sqrt{z(\theta)^2 + \rho(z(\theta))^2}$ in terms of $\theta = \arccos(z/r)$:

$$\left(\frac{r}{\lambda}\right)^4 = \frac{1}{2}\left(5\cos^3\theta - 3\cos\theta\right) = P_3(\cos\theta). \tag{B.26}$$

This is the shape that optimizes the signal-to-noise ratio given the condition of closest approach, and all that is left is to find the parameter λ in terms of R_{max}. When $\theta = 0$, we have $r = \lambda$, and so λ is the distance from the center of the sample (which is also the origin of the coordinate system) to the top of the sensor magnet. The optimal shape is shown in Figure B.2.

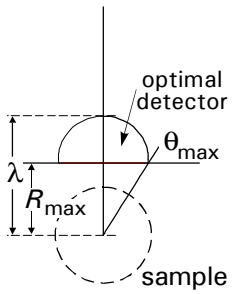

Figure B.2. Optimal shape for the detector magnet.

To find λ, we recognize that, in Equation (B.25), we have both an integral equation,

$$\lambda^{-4} = \frac{F}{2V} = \frac{\int_{R_{\max}}^{\lambda} \frac{z\rho^2}{r^5}\, dz}{2\int_{R_{\max}}^{\lambda} \rho^2 dz}, \tag{B.27}$$

and a functional form for r (and therefore z and ρ) as a function of θ (which we have already recast in the form of Equation (B.26)) that we can substitute directly into the integrands. Note also that the limits on z have been written $\{z \mid R_{\max} \le z < \lambda\}$, since the function $\rho = \rho(z)$ is zero for values of z greater than λ. We first multiply Equation (B.27) by λ times the denominator of the right-hand side, rearrange, and find

$$2\lambda^{-3}\int_{R_{\max}}^{\lambda} \rho^2 dz - \lambda\int_{R_{\max}}^{\lambda} \frac{z\rho^2}{r^5}\, dz = \int_{R_{\max}}^{\lambda} \left(2\lambda^{-2}\rho^2 - \lambda^2\,\frac{z\rho^2}{r^5}\right)\lambda^{-1} dz = 0\,. \tag{B.28}$$

The latter integral (which is dimensionless in anticipation of a later substitution) may now be rewritten with the substitutions

$$\rho = r(\theta)\sin\theta\,, \quad z = r(\theta)\cos\theta\,,$$

and

$$dz = \left(r'(\theta)\cos\theta - r(\theta)\sin\theta\right)d\theta\,. \tag{B.29a,b,c}$$

The result is

$$\int_{\theta_{\max}}^{0} \left(\frac{2r^2\,\sin^2\theta}{\lambda^2} - \frac{\lambda^2\cos\theta\sin^2\theta}{r^2}\right)\frac{r}{\lambda}\left(\frac{r'(\theta)}{r}\cos\theta - \sin\theta\right)d\theta = 0\,. \tag{B.30}$$

The limits R_{max} and λ have been replaced by the corresponding θ values θ_{max} and 0 (see Figure B.2). In combination with Equation (B.26), which expresses r/λ as a function of θ, Equation (B.30) is an integral equation for the angle θ_{max}. To solve it, we implicitly differentiate Equation (B.26) and find that

$$\frac{r'(\theta)}{r} = \frac{3}{4}\frac{1-5\cos^2\theta}{5\cos^3\theta - 3\cos\theta}\sin\theta\,. \tag{B.31}$$

Substituting Equations (B.26) and (B.31) into (B.30), we obtain

$$\frac{5\cdot 2^{1/4}}{4}\int_0^{\theta_{max}} \frac{\left(5\cos^2\theta-4\right)\left(1-\cos^2\theta\right)\left(3-7\cos^2\theta\right)\cos^2\theta}{\left(5\cos^3\theta-3\cos\theta\right)^{5/4}}\sin\theta d\theta = 0\,, \tag{B.32}$$

which can be solved numerically, yielding $\cos\theta_{max} \approx 0.84913$ (or $\theta_{max} \approx 31.88°$).

Now, $z = R_{max}$ when $\theta = \theta_{max}$, and so, substituting $r = z\sec\theta$ into Equation (B.26) we find

$$\left(\frac{R_{max}\sec\theta_{max}}{\lambda}\right)^4 = \frac{1}{2}\left(5\cos^3\theta_{max} - 3\cos\theta_{max}\right), \tag{B.33}$$

whose solution is $\lambda \approx 1.6542\,R_{max}$. Figure B.2 is drawn consistent with this ratio.

A sensor magnet shaped as in Figure B.2 is a global optimum as regards sensitivity (given that the motional mass is dominated by that of the magnetic material), but other considerations render it impractical for BOOMERANG. Large static forces would result from placing such a "mushroom-cap" magnet inside a suitable annulus, and homogeneity through the sample volume would be compromised were this shape used instead of the optimal right circular cylinder, or "hockey-puck" of Chapter 2. Fortunately, the sensitivity of the best hockey-puck

design is about 72% of the globally optimal mushroom-cap design and about 36% better than an optimized spherical sensor magnet (all constrained by the same R_{max}). The close match in size between the optimal cylinder and the global optimum is shown in Figure B.3. The near-optimal sensitivity of the hockey puck, in combination with its superior homogeneity and relative ease of manufacture at the millimeter size scale and below make it the best choice for the sensor magnet's shape.

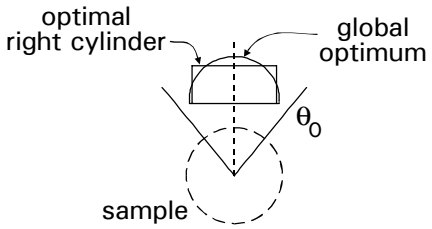

Figure B.3. Optimal shape for the detector magnet compared to optimal right cylinder. The sensitivity of the cylinder is nearly (about 72%) the optimal sensitivity. The nodal surface at polar angle θ_0 described in Chapter 2 is also shown.

B.1 Hockey-Puck Design with Added Inert Mass

In the BOOMERANG prototype described in Chapter 3, the magnet material comprises 83.1mg/92.7mg = 90% of the motional mass of the sensor oscillator. In practical microscopic designs, this ratio might vary substantially due to the realities of microfabrication, and so it is of interest to assess the effect of including inert mass (the silicon suspension) in the sensitivity optimizations for hockey-puck designs.

Figure 2.3 of Chapter 2 showed that for the case of no inert mass, the signal-to-noise ratio is not a sharply peaked function of either the sensor magnet's radius *a* or its height *h*. That figure is reproduced in Figure B.4 a with a larger range

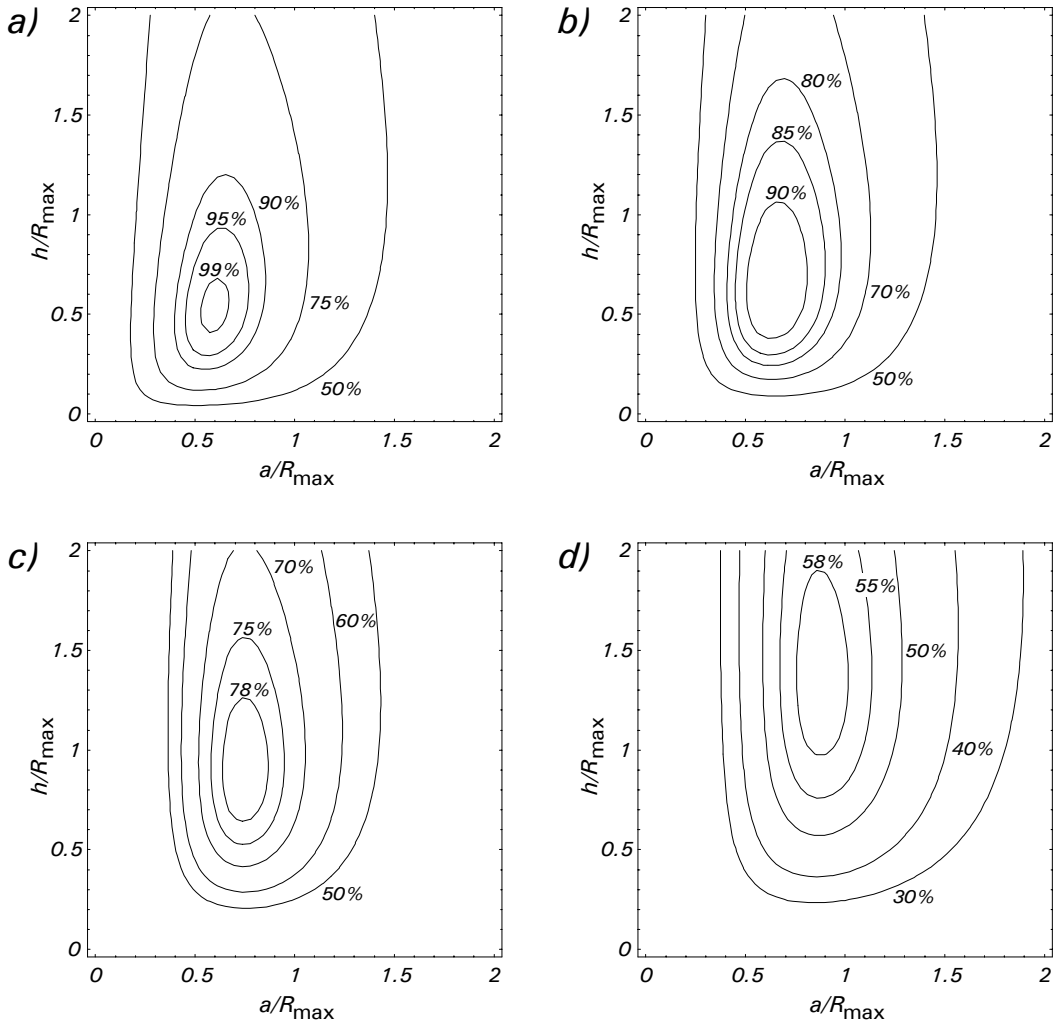

Figure B.4 Signal-to-noise ratio (*SNR*) vs. scaled radius a and height h of the sensor magnet. The contours show *SNR* relative to the *SNR* of the optimal design at $a/R_{max} = 0.59$ and $h/R_{max} = 0.53$ in Figure B.4 a, in which the suspension adds nothing to the oscillator's motional mass. a) No added inert mass. b) Inert mass 14.4% of Figure a's optimal mass, as in the BOOMERANG prototype. c) Inert mass equal to Figure a's optimal mass. d) Inert mass equal to five times Figure a's optimal mass.

of parameters. Figures B.4 b–d show contour plots of the SNR calculated for three other cases. In each case, the mass of the optimal sensor of Figure B.4 a is used as a fiducial mass. In Figure B.4 b, the effective mass of the silicon suspension is 14.4% of this fiducial mass. This is the relative mass of the silicon suspension used

in the BOOMERANG prototype. In Figure B.4 c, the case of an inert mass equal to the fiducial mass is shown, and in Figure B.4 d, the inert mass is five times the fiducial mass. The contours show that reasonably good *SNR* can be achieved over a wide range of design parameters when only mass and signal force are taken into account. A significant aspect of all of these graphs is that a $\sim$30% change in the radius *a* about its optimal value causes less than 5% loss in *SNR*, indicating that a small sacrifice in sensitivity could yield gains in homogeneity (with concomitant reduction in required rf power and heating of the oscillator and sample). More importantly, a more refined optimization procedure, which accounts for improved oscillator ring-down times associated with better sensor-annulus gap placement and spacing, should therefore have sufficient leeway to improve the sensitivity of next-generation BOOMERANG devices.

References

1 C. Lanczos, *The Variational Principles of Mechanics*, 4th ed. (Dover, New York, 1970), p. 59.

2 H. Goldstein, *Classical Mechanics*, 2nd ed. (Addison-Wesley, Reading, MA, 1980), p. 42.

Appendix C: Damping Due to Eddy Currents

Figure C.1 shows a cutaway view of the cylindrical sensor magnet moving inside an annular magnet. The relative motion of these magnets induces eddy currents in both the sensor and the annulus, with such currents being proportional to the material's conductivity. The goal of this appendix is to calculate the oscillator's damping rate $\gamma = 2/\tau$ due to eddy currents in the BOOMERANG prototype.

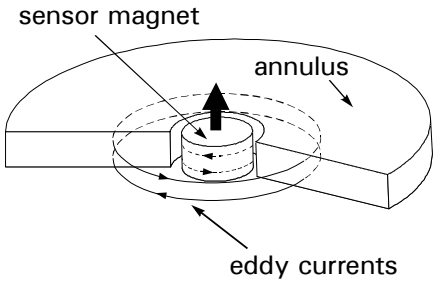

Figure C.1. Eddy currents due to relative motion of the magnets.

We start by considering the electric field produced by the sensor magnet moving in the rest frame of the annular magnet. If a stationary magnetized body produces a magnetic field $\mathbf{B}(\mathbf{r})$, then it produces an electric field

$$\mathbf{E}(\mathbf{r}) = -\mathbf{v} \times \mathbf{B}(\mathbf{r}) \tag{C.1}$$

in a coordinate frame in which its velocity is $\mathbf{v}$. The same result is obtained by considering the time derivative of the local vector potential. This electric field induces eddy currents in the conducting annular magnet that are strictly azimuthal

due to the symmetry of the magnets, as we shall see. We will neglect eddy currents in other metal parts due to the fact that these parts are far more distant from the sensor than the annulus is and because, as we will see, the eddy current density falls off very rapidly with distance. Eddy currents in the sensor (by virtue of its motion in the field of the other magnets) can also be calculated in the rest frame of the sensor magnet using Equation (C.1).

Before we continue, an important point must be made. Our analysis will leave out the fact that the eddy currents themselves are time-varying. A given induced current element therefore gives rise to oscillating electromagnetic fields and secondary eddy currents in nearby conductors. A more rigorous analysis of the problem must therefore be cast in terms of field equations[1], which are further complicated by moving media[2]. We shall continue with our more or less rough estimate of the eddy currents nonetheless. It will turn out that while the skin depth in the mu-metal magnets (which can be said to quantify the importance of this "self-consistent-field" issue),

$$\delta = \sqrt{\frac{2}{\omega\sigma\mu}} = \sqrt{\frac{2}{(2\pi \cdot 500\,\mathrm{Hz})(1.72 \cdot 10^{6}\,\Omega^{-1}\mathrm{m}^{-1})(50000 \cdot 4\pi \cdot 10^{-7}\ \mathrm{TmA}^{-1})}} = 77\,\mu\mathrm{m}\,, \quad \text{(C.2)}$$

is far smaller than the size of the magnets, it is about the same size as the range over which eddy currents are strong. So, the more rigorous analysis will not differ wildly from our simpler theory at the prototype size scale, and agreement between the theories will become closer as size scales are reduced.

The system of sensor magnet and annulus is symmetric with respect to rotation about the vertical axis. Consequently, the azimuthal component of the magnetic field

$$\mathbf{B}(\rho, z) = B_\rho(\rho, z)\hat{\rho} + B_z(\rho, z)\hat{\mathbf{z}} \tag{C.3}$$

vanishes, and we may work in a gauge in which the magnetic vector potential $\mathbf{A}(\rho, z) = A_\phi(\rho, z)\hat{\phi}$ is strictly azimuthal. Here and in what follows we make use of a cylindrical coordinate frame $\{\hat{\rho}, \hat{\phi}, \hat{\mathbf{z}}\}$, with z along the symmetry axis. The velocity of the sensor magnet $\mathbf{v} = v\,\hat{\mathbf{z}}$ is also along the symmetry axis, and since the symmetry is therefore not broken, we may write Equation (C.1) as

$$\mathbf{E} = -v\,B_\rho\hat{\phi}\,. \tag{C.4}$$

Since the boundaries of the cylindrical magnets are parallel to this azimuthal electric field, and since the conductivity σ is isotropic, the induced currents $\mathbf{J}(\mathbf{r}) = \sigma\mathbf{E}(\mathbf{r})$ at every position $\mathbf{r}$ are also strictly azimuthal. We then find that the local dissipated power density is

$$W = \mathbf{J}\cdot\mathbf{E} = \sigma E^2 = \sigma v^2 B_\rho^2\,. \tag{C.5}$$

The velocity $v(t) = v_0\cos\omega t$ is a function of time, and we may write the total instantaneous power dissipation as an integral over the volume V of the conductor in terms of the radial field B_ρ produced by the moving element,

$$P(t) = \int_V W dV = \sigma v(t)^2 \int_V B_\rho^2 dV\,. \tag{C.6}$$

The dissipated power is also the (negative) time derivative of the work done by the dissipative force $\mathbf{F} = -\alpha\mathbf{v}$:

$$P(t) = -\frac{\mathrm{d}}{\mathrm{d}t}U = -\frac{\mathrm{d}}{\mathrm{d}t}\int_0^t \mathbf{F}\cdot\mathbf{dl} = \frac{\mathrm{d}}{\mathrm{d}t}\int_0^t \alpha\mathbf{v}(t')\cdot\mathbf{v}(t')dt' = \alpha v(t)^2 . \qquad \text{(C.7)}$$

Setting Equations (C.6) and (C.7) equal, we find

$$\gamma = \frac{1}{m}\alpha = \frac{\sigma}{m}\int_V B_\rho^2 dV . \qquad \text{(C.8)}$$

An important conclusion to be drawn from Equation (C.8) is that, since the conductivity σ and the field B are scale-invariant, and since m and V are both proportional to r^3, the damping rate γ is scale-invariant. To evaluate the integral in (C.8), we must first know B_ρ, which is itself the result of a volume integration over contributions from dipole elements in the moving magnet. It is convenient first to find the vector potential $\mathbf{A}(\mathbf{r})$, in terms of which we have

$$B_\rho = \hat{\rho}\cdot\nabla\times\mathbf{A} = -\frac{\partial A_\phi}{\partial z} . \qquad \text{(C.9)}$$

If we assume that the magnetization is uniform, then the necessary volume integration,

$$\mathbf{A}(\mathbf{r}) = \frac{\mu_0}{4\pi}\iiint_{\text{magnet}} \frac{M\hat{\mathbf{z}}\times\hat{\mathbf{r}}}{r^2}dV , \qquad \text{(C.10)}$$

is simplified by standard integral theorems. We obtain the well-known result[3] that the field outside a cylindrical magnet with uniform axial magnetization is the same

as if the magnet were replaced by a solenoid of the same dimensions with the surface current density equal to the magnetization *M*:

$$\mathbf{A}(\mathbf{r}) = \frac{\mu_0 M}{4\pi} \iint_{\text{side}} \frac{\hat{\phi}}{r}\, ds\,. \tag{C.11}$$

The surface element in this integral, $ds = \rho d\phi dz$ includes the axial coordinate *z*, and so combination of Equations (C.9) and (C.11) is facilitated by the fundamental theorem of calculus, which offsets the axial derivative and integration. The result is

$$B_\rho(\mathbf{r}) = \frac{\mu_0 M}{4\pi}\left[\oint_{\substack{\text{top}\\ \text{edge}}} \frac{a\hat{\phi}}{r}\, d\phi - \oint_{\substack{\text{bottom}\\ \text{edge}}} \frac{a\hat{\phi}}{r}\, d\phi \right], \tag{C.12}$$

where *a* is the radius of the magnet. The integration paths for these integrals are as shown in Figure C.2.

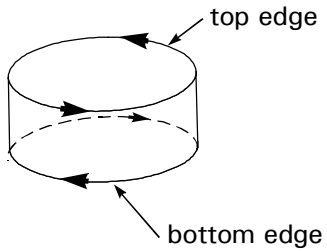

Figure C.2. Integration paths for Equation (C.8) when the sensor magnet is considered the source of electric fields (in the other magnets).

The line integrals in Equation (C.12) may be evaluated in terms of the complete elliptic integrals of the first and second kinds, *K*(*m*) and *E*(*m*). The result is

$$I(\rho, z) \equiv \oint_{\substack{\text{edge}\\ \text{ring}}} \frac{a\hat{\phi}}{r}\, d\phi = \sqrt{\frac{4a}{\rho}}\left(\frac{(2-m)K(m) - 2E(m)}{\sqrt{m}} \right)\hat{\phi}\,, \tag{C.13}$$

where $m = \dfrac{4a\rho}{z^2 + (\rho + a)^2}$, and where z is measured from the plane of the given edge ring (top or bottom).

The same analysis applies to calculation of eddy currents in the sensor magnet if one calculates with the other magnets moving with velocity **v** in the rest frame of the sensor magnet. (Effects due to acceleration of the magnets are negligible and ignored.) Equations (C.12) and (C.13) may be used to calculate the integrand B_ρ^2 in Equation (C.8). Figure C.3 shows a contour plot of this value (scaled by the Jacobian determinant for the integration, which is ρ). The picture is a detailed map of how the dissipated power density is distributed inside the magnets. The eddy currents are concentrated near the sharp edges of both the sensor magnet and annulus.

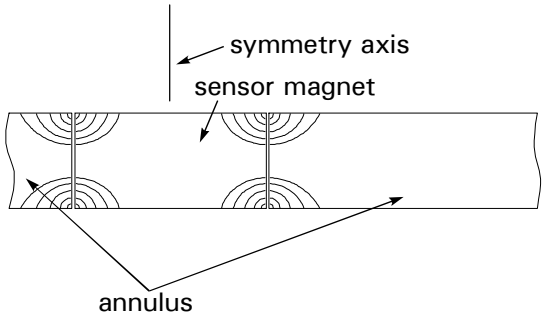

Figure C.3. Power dissipation in the magnets. Contours show where most of the power is dissipated. Each contour represents a factor of 2 decrease in power density.

Figure C.3 shows that the power density falls off approximately exponentially with distance from the sharp corners of the magnets. The calculated distance over which the power density decreases by e in this model is 110 μm, which is close to the skin depth (77 μm) calculated at 500 Hz for mu metal. This means that we are somewhat *over*-estimating the damping rate, which we calculate to be 0.93 Hz by numerically integrating (C.8). Were the skin depth much smaller (or the magnets larger), the conclusions drawn from our rough theory of eddy

currents would have to be changed. In particular, the effective conductivity, and therefore the damping rate, would be reduced. The effective size of the conductor would also scale as an area rather than a volume, and so, above the size scale of the BOOMERANG prototype, the damping rate γ scales inversely with size (as r^{-1}).

Again, because of the skin effect, we are slightly overestimating the eddy current damping with our simplified model relative to a more exact calculation with field equations. However, the observed damping rate is still somewhat *larger* than we've calculated. Empirically we find that introducing radial slits to interrupt and redirect the eddy currents reduces the damping rate, as does increasing the gap or rounding the edges of the magnets[4]. So it is likely that our assumption of perfectly uniform magnetization is an oversimplification. Indeed, allowing the magnetization to have a nonvanishing radial component would increase B_p in Equation (C.8), and this would also increase our estimate of the damping rate.

References

1 W. R. Smythe, *Static and Dynamic Electricity*, 3rd ed. (McGraw-Hill, New York, 1968).

2 P. Penfield and H. A. Haus, *Electrodynamics of Moving Media* (M.I.T. Press, Cambridge, MA, 1967).

3 P. Lorrain, D. R. Corson, and F. Lorrain, *Electromagnetic Fields and Waves*, 3rd ed. (W. H. Freeman and Co., New York, 1988).

4 L. A. Madsen, Ph. D. Thesis, California Institute of Technology, 2002.

Appendix D: Partition Function, Polarization, and Moment Generating Function for N Isochronous Spins

D.1 Partition Function

The thermal-equilibrium density operator for a system of N isochronous spins ½ at temperature T is given by

$$\rho_0 = \frac{1}{Q} e^{-H/k_B T}, \tag{D.1}$$

where

$$Q \equiv Tr\left\{e^{-H/k_B T}\right\} \tag{D.2}$$

denotes the partition function, and

$$H = -\hbar\omega_0 I_z \tag{D.3}$$

denotes the Hamiltonian, with ω_0 the Larmor frequency of the spins and

$$I_z = \sum_{j=1}^{N} I_{z,j} \tag{D.4}$$

the z-component of the total dimensionless angular momentum. Let

$$x \equiv \frac{\hbar\omega_0}{k_B T} . \tag{D.5}$$

Then

$$Q = Tr\left\{e^{xI_z}\right\} = Tr\left\{\prod_{j=1}^{N} e^{xI_{z,j}}\right\}. \tag{D.6}$$

If we expand each exponential in powers of $I_{z,j}$ and note that, for spin ½ operators, $I_{z,j}^2 = \frac{1}{4}\mathbf{1}$, we find that

$$Q = Tr\left\{\prod_{j=1}^{N}\left(\mathbf{1}\cosh\left(\frac{x}{2}\right) + 2I_{z,j}\sinh\left(\frac{x}{2}\right)\right)\right\}. \tag{D.7}$$

Expansion of the product yields a sum of operators, only one of which, $\mathbf{1}$, has nonzero trace ($Tr\{\mathbf{1}\} = 2^N$). Thus,

$$Q = 2^N\left(\cosh\frac{x}{2}\right)^N . \tag{D.8}$$

D.2 Polarization

Let us consider a Boltzmann distribution of spins ½ in two energy levels $\varepsilon_{\pm} = \pm\frac{1}{2}\hbar\omega_0$. We define the polarization, p, as the difference in the populations of the energy levels, normalized to unity:

$$p \equiv \frac{n_- - n_+}{n_- + n_+} = \frac{e^{+\frac{1}{2}x} - e^{-\frac{1}{2}x}}{e^{+\frac{1}{2}x} + e^{-\frac{1}{2}x}} = \tanh\frac{x}{2} . \tag{D.9}$$

D.3 Moment generating function

The moment generating function, defined by

$$G(s) = \left\langle e^{isI_z} \right\rangle , \tag{D.10}$$

is used in Chapter 5 to calculate expectation values of powers of I_z. With the equilibrium density operator ρ_0 and the parameter x defined as above, we have

$$G(s) = \frac{1}{Q} Tr\left\{ e^{xI_z} e^{isI_z} \right\} = \frac{1}{Q} Tr\left\{ e^{(x+is)I_z} \right\}. \tag{D.11}$$

In correspondence with Equations D.6–D.8, this may be written

$$G(s) = \frac{1}{Q} Tr\left\{ e^{(x+is)I_z} \right\} = \frac{1}{Q} 2^N \cosh^N\left(\frac{x+is}{2}\right) = \frac{\cosh^N\left(\frac{x+is}{2}\right)}{\cosh^N\left(\frac{x}{2}\right)} = \left(\frac{\cosh\left(\frac{x+is}{2}\right)}{\cosh\left(\frac{x}{2}\right)} \right)^N . \tag{D.12}$$

The hyperbolic cosine in the numerator may be expanded:

$$\cosh\left(\frac{x+is}{2}\right) = \cosh\left(\frac{x}{2}\right)\cos\left(\frac{s}{2}\right) + i \sinh\left(\frac{x}{2}\right)\sin\left(\frac{s}{2}\right). \tag{D.13}$$

Substitution of Equations D.9 and D.13 into Equation D.12 yields the moment generating function in terms of the number of spins N and the polarization p:

$$G(s) = \left(\cos\frac{s}{2} + ip \sin\frac{s}{2} \right)^N . \tag{D.14}$$